Spectral characterization of materials using Terahertz Time Domain Spectroscopy (THz-TDS)

by

Huzifa Zain Alabdeen Abdarahman Hissen

Thesis presented for the degree of Master of Physics in the Faculty of Science at the Stellenbosch University

Department of Physics,
Stellenbosch University,
Private Bag X1, Matieland 7602, South Africa.

Supervisors:

Prof. E.G. Rohwer

Dr. P.H. Neethling

December 2014

Declaration

By submitting this thesis electronically, I declare that the entirety of the work contained therein is my own, original work, that I am the owner of the copyright thereof (unless to the extent explicitly otherwise stated) and that I have not previously in its entirety or in part submitted it for obtaining any qualification.

Date: December 2014 .....

Abstract

Spectral characterization of materials using Terahertz Time Domain Spectroscopy (THz-TDS)

H.Z.A.A. Hissen

Department of Physics,
Stellenbosch University,
Private Bag X1, Matieland 7602, South Africa.

Thesis: MSc

December 2014

Terahertz (THz) radiation is often used in many promising applications such as information and communication technology and airport security. Optimized and adapted terahertz fields hold huge promise for leading this technology further. This study is focused on terahertz time domain spectroscopy (THz-TDS). In THz-TDS the electric field is measured, therefore both amplitude and phase information of the THz pulse can be obtained. We used the pump-probe technique in order to measure a THz pulse from the photoconductive antenna. A pulsed fiber laser with FWHM of $\simeq 100$ fs was used for this. The frequency spectrum of the measured THz pulse was obtained via a fast Fourier transform. We studied the principles of the THz pulse generation as well as detection, with a photoconductive antenna as emitter and detector. In this study terahertz spectroscopy has been used to investigate the refractive index and absorption coefficient of different types of materials in the terahertz region. The last part of this study deals with a simple process for material parameter extraction of a polymer sample using commercial software called Teramat1.0. It uses the sample thickness, the reference THz pulse and the transmitted THz pulse to retrieve the complex refractive index of the sample.

Uittreksel

Spektrale karakterisering van materiale deur Terahertz Tyddomein Spektroskopie (THz-TDS)

*("**Spectral characterization of materials using Terahertz Time Domain Spectroscopy (THz-TDS)**")*

H.Z.A.A. Hissen

Fisika Departement ,
Universiteit Stellenbosch,
Privaatsak X1, Matieland 7602, Suid Afrika.

Tesis: MSc

Desember 2014

Terahertz (THz) straling word gereeld gebruik vir belowende toepassings soos inligting en kommunikasie tegnologie en lughawe sekuriteit. Geoptimeerde en aangepaste terahertz velde dra by tot die bevordering van die tegnologie. Hierdie studie fokus op terahertz tyd domein spektroskopie (THz-TDS). In THz-TDS word die elektriese veld gemeet en dus word beide amplitude en fase inligting van die THz puls verkry. Ons gebruik 'n pomp en toets tegniek om die THz puls deur 'n fotogeleidende antenna te bepaal. 'n Gepulseerde vesel laser met FWHM van 100 fs word hiervoor benut. Die frekwensie spektrum van die gemete THz puls word bereken deur 'n vinnige Fourier transvorm te bereken. Die beginsels van die generering en deteksie van THz pulse is bestudeer met 'n fotogeleidende antenna as sender en ontvanger. In die studie is terahertz spektroskopie gebruik om die brekingsindekse en die absorpsie koeffisiënte van verskillende materiale in die terahertz gebied te bepaal. Die laaste gedeelte van die studie handel oor 'n eenvoudige proses om die materiaal parameters van 'n polimeer te bepaal deur gebruik te maak van kommersiële sagteware Teramat 1.0. Die monster dikte, die THz verwysingspuls en die deurgelate puls word gebruik om die komplekse brekingsindeks van die materiaal te bereken.

Acknowledgements

I would like to express my sincere gratitude to the following people and institutions for thier contributions to this project:

- My supervisors, Prof Erich Rohwer and Dr Pieter Neethling, I appreciate your wisdom, guidance and a huge support during this work. You are excellent advisors and scientists. I have learned a great deal from you not only in terms of this work, but also in the general understanding and interest of physics. I do not think I have thanked you enough.
- The entire family of the Laser Research Institute, for their support and helpful discussions.
- Shane Smith for his advice and discussion on everything is greatly appreciated.
- All my parents, brothers and friends back in Sudan.
- The Stellenbosch University and the African Institute for Mathematical Sciences who co-operatively funded this project.

Dedications

To my dearest father, Mr Zain Alabdeen and my mother Laila Hassan, the source of endless encouragement and inspiration.

Contents

List of Figures

List of Tables

Chapter 1

Introduction

1.1 Background of Terahertz (THz) radiation

Terahertz (THz) radiation is electromagnetic radiation, has frequency of a 0.3 to 10 THz, which lies in the gap between the microwave and infrared regions of the electromagnetic spectrum as illustrated in Figure 1.1. In this spectrum 1 THz radiation has a period $\tau = 1/\nu = 1$ ps, a wavelength $\lambda = c/\nu = 0.3$ mm $= 300$ μm, a wavenumber $\bar{\kappa} = \kappa/2\pi = 1/\lambda = 33.3$ cm^{-1}, and photon energy $h\nu = \hbar\omega = 4.1$ meV, where c is the velocity of light in vacuum, and h is Plank's constant. Similarly as X-rays can see shapes within the human body, radio waves can transmit information, and visible light can create a photograph, THz waves can create imaging as well as can transmit information [54].

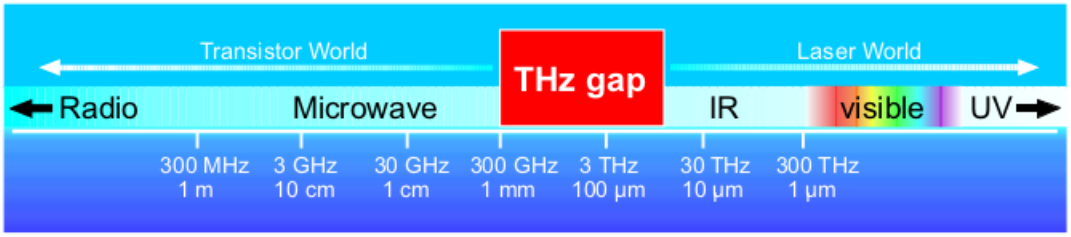

Figure 1.1: Electromagnetic spectrum showing THz gap [41].

There are many sources of THz radiation around us, like those sources from room temperature objects and those from cosmic background radiation to black body radiation. However most of these sources are incoherent, so they can hardly be useful. Until recently, a wide THz portion of the spectrum has not been useful due to unavailability of suitable THz emitters and detectors. Hence the THz radiation was called the THz gap in the electromagnetic spectrum. However, an immense effort has been made in order to reduce the THz gap in the electromagnetic spectrum by developing the THz sources using various technologies. Recent developments in THz technology has omened the possibility of applications in many different fields, such as microelectronics, forensic science and medicine among others [54].

Similar to the other electromagnetic waves, the behaviour and properties of the THz waves are determined by the Maxwell equations. According to the waves position on the electromagnetic

spectrum, THz waves are more difficult to handle than the other waves neighbouring to them [54].

The properties and the unique nature of THz waves has catalysed researchers to develop the frequency band of the THz wave for different applications, some of them are [54]

- Terahertz waves have low photon energies (non-ionizing), therefore (unlike X-rays) does not photoionize the biological tissues. Hence can be considered safe to use for the samples as well as the operator. As a result of extreme water absorption, THz waves, unlike microwaves, cannot penetrate through the human body. THz waves have a high ability to penetrate through the most dielectric materials, such as plastic, wood, paper, cardboard, and cloth [54].
- Due to dipole-allowed rotational and vibrational transitions many molecules exhibit strong absorption and dispersion at THz frequencies. These transitions are unique to the molecules thus spectroscopic fingerprinting within the range of the THz waves is possible [54].
- THz waves are coherent, therefore can be measured in the time domain by mapping the electric field in both phase and amplitude. This information gives us access to absorption and dispersion characteristics. The coherence of the THz radiation with a wide bandwidth provide a new procedure to investigate the vibronic, electronic, as well as the compositional properties of liquids, solids, and gases [54].

1.2 Applications of THz radiation

The properties and unique nature of THz waves enable it to have many important applications in different fields of science, such as material science and engineering, astrophysics, biomedical engineering, plasma physics, information science and technology, spectroscopy and imaging technology and environmental science, among others [56].

The THz applications exploit the characteristics of material responses to fundamental physical processes such as large-amplitude vibrational motions of organic compounds, rotational transitions of molecules, energy gaps in superconductors, and lattice vibrations in solids. THz region in the electromagnetic (EM) spectrum shows high atmospheric opacity compared with the other regions in the EM spectrum. Absorption by water vapour in the atmosphere is the main reason for the THz attenuation. In fact, for a THz wave applications, water vapour absorption is an important factor to be considered [20].

In the terahertz (THz) band, condensed matter is largely divided into conductors and insulators. Due to the high electrical conductivity, metals are considered as highly reflective in the THz region. In this region liquid water is strongly absorptive. Insulators such as clothes, paper, wood, plastic, etc, are transparent to THz waves. A brief characterization of the optical properties of different types of materials in the terahertz region are summarized in Table 1.1 [20].

Material type	Optical property
metal	high reflectivity ($> 99.5\%$ at 1 THz)
liquid water	high absorption ($\alpha \approx 250$ cm^{-1} at 1 THz)
plastic	low absorption ($\alpha < 0.5$ cm^{-1} at 1 THz), low refractive index ($n \approx 1.5$)
semiconductor	low absorption ($\alpha < 1$ cm^{-1} at 1 THz), high refractive index ($n \approx 3.4$)

Table 1.1: Optical properties of condensed matter in the THz region [20].

1.2.1 The application of THz radiation in biomedicine

Terahertz time domain spectroscopy (THz-TDS) can be applied in medical imaging, disease diagnosis, and organism detection. This is because biological macromolecules and DNA molecular vibration and rotation lie in the THz region, therefore the organism has a response to the THz radiation [56].

In the past decades, various applications for imaging in the biological and medical fields have been proposed, due to the technology development for generating as well as detecting the THz radiation. Recently several researchers have used THz waves imaging for observing dental tissue, liver cancer, skin burns and detecting skin cancer. However, the hindrance to this method is that liquid water in the tissue strongly absorbs THz waves [14].

1.2.2 The application of THz radiation in security and quality control

Over the past decade terahertz (THz) radiation has been applied in many significant interesting applications, such as imaging for security, and spectroscopy [7]. Since many non-polar and dielectric materials are transparent to THz waves, THz waves can be used to detect concealed weapons. Since THz radiation has a capability to penetrate through clothing, plastics and luggages and other dielectric materials, its can be use to detect illegal drugs and explosives even if they are concealed [7].

Terahertz (THz) radiation has low photon energy (non-ionising), therefore its can be considered as safe to use for high resolution imaging, as well as the identification through spectroscopy of dangerous materials, even if they are concealed in luggages or under clothes [2].

1.3 Objectives of the study

The main goals of our study are described as follows

- To give a brief description of the properties and some applications of the THz waves in different fields.
- To introduce the basic concept of terahertz time domain spectroscopy (THz-TDS).
- To understand and discuss the general concept of the electric circuits as well as a photoconductive antennas used in THz spectroscopy.

- To give a brief description of the fundamental physics involved in generation as well as detection of THz pulse in photoconductive antennas.
- To describe the THz pulse as an electromagnetic wave, and consider its interaction with dielectric materials.
- To use THz pulse to investigate the refractive index and absorption coefficient of different types of materials in the terahertz range.

1.4 Structure of the thesis

In Chapter 1, we give an introduction to the general background of THz waves and give a some general applications of THz waves in different fields such as biomedicine, security and quality control.

Chapter 2 discusses the general theoretical background of the electromagnetic wave (EM) (because THz wave can be described as EM wave). We start with Maxwell's equations in both vacuum and medium to obtain the wave equation. Secondly we discuss the interaction of the EM wave with dielectric media.

In Chapter 3 we discuss the general concept of the mathematical tool (Fourier transform) which relates time and frequency domain and allows us to obtain the spectrum of the THz pulse.

Chapter 4 deals with general background theory of the oscillation in a series RLC circuit showing the flowing current and the various types of damping by the circuit. Also a general description of the photoconductive antennas which is used for the generation as well as detection of the THz pulse will be highlighted.

In Chapter 5 we describe the experimental setup, and show how THz pulse can be measured experimentally using the photoconductive antenna as emitter and detector.

In Chapter 6 we present our results concerning the description of the absorption and transmissions of the THz pulse through the materials by investigating optical properties of materials. In Chapter 7 we give conclusions on this work.

Chapter 2

Theoretical background of the electromagnetic wave (EM)

2.1 Maxwell's equations

Maxwell's equations are the fundamental equations in the electromagnetic theory. Maxwell's equations describe the behaviour of the electric and magnetic fields when the electromagnetic wave propagates through a medium or free space. Maxwell's equations were developed over centuries by Gauss, Ampere, Faraday, and others. They predicted that the velocity c of the electromagnetic wave in a free space is $c = (\mu_0\epsilon_0)^{-1/2}$, which has the same value as the velocity of light. The values of the permeability and the permittivity of the free space are respectively $\mu_0 = 4\pi \times 10^{-7}$ H/m and $\epsilon_0 = 8.854 \times 10^{-12}$ F/m [40].

2.1.1 Maxwell's equation for a vacuum

The general expression of the Maxwell's waves equations in the vacuum can be written in the SI units, as [40, 10, 38]

$$\nabla \cdot \vec{E} = \frac{\rho}{\epsilon_0} \qquad \text{Gauss's law (electric),} \tag{2.1.1}$$

$$\nabla \cdot \vec{B} = 0 \qquad \text{Gauss's law (magnetic),} \tag{2.1.2}$$

$$\nabla \times \vec{E} = -\frac{\partial \vec{B}}{\partial t} \qquad \text{Faraday's law,} \tag{2.1.3}$$

$$\nabla \times \vec{B} = \mu_0 \left(\vec{J} + \epsilon_0 \frac{\partial \vec{E}}{\partial t} \right) \qquad \text{Ampere-Maxwell law.} \tag{2.1.4}$$

Where μ_0 and ϵ_0 are the permeability and permittivity of vacuum, respectively, ρ and $\vec{J}$ are, respectively, the charge and current densities and $\vec{E}$ and $\vec{B}$ are the electric and magnetic field, respectively [40, 10, 38].

In free space, and there are no charge and current densities, then the Maxwell's equations can be reduced to [10]

$$\nabla \cdot \vec{E} = 0, \quad \nabla \times \vec{E} = -\frac{\partial \vec{B}}{\partial t}, \tag{2.1.5}$$

$$\nabla \cdot \vec{B} = 0, \quad \nabla \times \vec{B} = \mu_0 \, \epsilon_0 \frac{\partial \vec{E}}{\partial t}. \tag{2.1.6}$$

2.1.2 Maxwell's equation for a dielectric medium

If the medium is a linear homogeneous and there is no free charge and no free current densities, then Maxwell's equations can be written as [10]

$$\nabla \cdot \vec{D} = 0, \quad \nabla \times \vec{E} = -\frac{\partial \vec{B}}{\partial t}, \tag{2.1.7}$$

$$\nabla \cdot \vec{B} = 0, \quad \nabla \times \vec{H} = \mu \, \epsilon \frac{\partial \vec{D}}{\partial t}, \tag{2.1.8}$$

$$\text{with} \;\; \vec{D} = \epsilon \, \vec{E}, \quad \text{and} \;\; \vec{H} = \vec{B} \frac{1}{\mu}, \tag{2.1.9}$$

where $\vec{D}$ is the electric displacement field, and $\vec{H}$ is the magnetic field intensity. These equations are known as Maxwell's equations in the differential form [10].

2.2 Plane wave equation

From the Maxwell's equations which are described above we are able to derive the general forms of the plane wave equation in free space (no charges and no currents) as follows [38]

If we take the curl of Eq 2.1.3, then we can write [38]

$$\nabla \times (\nabla \times \vec{E}) = -\frac{\partial (\nabla \times \vec{B})}{\partial t}, \tag{2.2.1}$$

by using the vector identity we can write

$$\nabla \times (\nabla \times \vec{E}) = \nabla (\nabla . \vec{E}) - \nabla^2 \vec{E},$$

that implies Eq. 2.2.1 become as

$$\nabla (\nabla \cdot \vec{E}) - \nabla^2 \vec{E} = -\frac{\partial (\nabla \times \vec{B})}{\partial t}, \tag{2.2.2}$$

since the Gauss's law for the electric field in free space given by [40, 10, 38]

$$\nabla \cdot \vec{E} = 0, \tag{2.2.3}$$

now by substituting Eq. 2.2.3 into Eq. 2.2.2, we have

$$\nabla^2 \vec{E} = \frac{\partial (\nabla \times \vec{B})}{\partial t}. \tag{2.2.4}$$

Since the Ampere-Maxwell law in free space can be written as [40, 10, 38]

$$\nabla \times \vec{B} = \mu_0 \, \epsilon_0 \frac{\partial \vec{E}}{\partial t}, \tag{2.2.5}$$

and by substituting Eq. 2.2.5 into Eq. 2.2.4, we have

$$\nabla^2 \vec{E} - \mu_0 \, \epsilon_0 \frac{\partial^2 \vec{E}}{\partial t^2} = 0. \tag{2.2.6}$$

By using the same method, we can obtain

$$\nabla^2 \vec{B} - \mu_0 \, \epsilon_0 \frac{\partial^2 \vec{B}}{\partial t^2} = 0. \tag{2.2.7}$$

Equations. 2.2.6, and 2.2.7, have a general solution (known as plane wave equation in free space), which can be written as [38]

$$\vec{E}(\vec{x}, t) = \vec{E_0} \exp i(\vec{k_0}.\vec{x} - \omega \, t), \tag{2.2.8}$$

and

$$\vec{B}(\vec{x}, t) = \vec{B_0} \exp i(\vec{k_0}.\vec{x} - \omega \, t), \tag{2.2.9}$$

where $\vec{k_0}$ is the wave vector in vacuum, also called propagation vector, $\vec{x}$ is the direction of the propagation, $\omega = 2\pi\nu$ is the angular frequency, and ν is the frequency [38].

Generally the plane wave equation allows us to see that the properties of the electromagnetic waves such as the direction of the wave propagation, wavelength, the speed of the wave, and the frequency are determined from the solution of wave equation. From the plane wave solution, we are able to derive the general form of the phase velocity c. If we consider the phase of the wave in a phase front, then $(kx - \omega \, t)$, is constant, then $v = \frac{dx}{dt} = \frac{\omega}{k} = \lambda\nu$ [38].

In a medium, the speed of the electromagnetic wave propagation can be written as [10]

$$v = \frac{1}{\sqrt{\epsilon \, \mu}} \quad = \frac{c}{n},$$

where n is the refractive index of the medium, and it is can be expressed as [10]

$$n = \frac{c}{v} = \sqrt{\frac{\epsilon \, \mu}{\epsilon_0 \, \mu_0}}.$$

For most mediums, μ is very close to μ_0, then [10]

$$n = \sqrt{\frac{\epsilon}{\epsilon_0}} = \sqrt{\epsilon_r}.$$

Here ϵ_r is the relative permittivetly or dielectric constant. For materials ϵ_r is always greater than 1, which leads to the fact that light travels slower through the material than the vacuum [10].

In order to write the general form of the refractive index, we wish use the concept of the polarization of the material, to get the relation between the polarization and the refractive index of the material, we can use the relation between the electric field and the polarization of the material, since the electric displacement vector $\vec{D}$ is defined as [40]

$$\vec{D} = \epsilon_0 \vec{E} + \vec{P} = \epsilon \vec{E}, \tag{2.2.10}$$

where ϵ_0 is permittivity of free space, and $\vec{P}$ is polarization.

Now from Eq. (2.1.9) and Eq. (2.2.10) we can write the relationship between the polarization and the electric field as [40]

$$\vec{P} = \epsilon_0(\epsilon_r - 1)\,\vec{E} = \chi_e \epsilon_0\,\vec{E}, \tag{2.2.11}$$

where χ_e is the electric susceptibility and it is equal to $(\epsilon_r - 1)$. It is a useful parameter, to consider effects in the optical frequency range; in case of the centro symmetric media such as glass, it is a simple scalar quantity and for an isotropic material, it can be expressed as a form of tensor to account of the change in polarization response for different directions of the applied electric field $\vec{E}$ [40].

For the general material, if there is a number of atoms or molecules N per unit volume, each is polarized by the electric field $\vec{E}$, to form a dipole with moment $\vec{P} = N\alpha\vec{E}$, where α denotes the individual polarizability, then the form of the relation between (ϵ_r) and $\vec{P}$, it can be written as [43]

$$\epsilon_r = 1 + \frac{\alpha N}{\epsilon_0} \quad = 1 + \frac{\vec{P}}{\epsilon_0\,\vec{E}}, \tag{2.2.12}$$

Consider an $\vec{E}$ wave propagating through medium with index of refraction $\tilde{n}$. In this case the refractive index is a complex number that has real and imaginary parts; and it is denoted by $\tilde{n} = n + i\kappa$. Then the wave number k is given by $k = \frac{\omega}{v} = \frac{\tilde{n}\omega}{c} = \tilde{n}k_0$ where k_0 is the wave number in vacuum. Also $k = \frac{2\pi}{\lambda} = \frac{\tilde{n}2\pi}{\lambda_0}$ where λ is the wavelength in the medium and λ_0 is the wavelength in vacuum. The expression for the electric wave becomes [43]

$$\vec{E} = \vec{E_0}\,\exp(i(n + i\kappa)\vec{k_0}.\vec{x} - i\,\omega t), \tag{2.2.13}$$

where n is the real part of the refractive index, and κ is the imaginary part of the refractive index.

We can write Eq. 2.2.13 as

$$\vec{E} = \vec{E_0}\,\exp(-\kappa\,\vec{k_0}.\vec{x})\;\exp(i\,n\,\vec{k_0}.\vec{x} - i\,\omega t), \tag{2.2.14}$$

here κ is referred to as the extinction coefficient. The wave proceeds at the phase velocity c/n, while the amplitude decays exponentially with distance [43].

Therefore

$$\tilde{n}^2 = (n + i\kappa)^2 = n^2 - \kappa^2 + i\,2n\,\kappa. \tag{2.2.15}$$

If κ is small enough, as the case of the transparent gas or any dielectric material where the attenuation is small, then the refractive index can be reduced as

$$\tilde{n}^2 \approx 1 + \frac{\alpha N}{\epsilon_0}. \tag{2.2.16}$$

Equations. (2.2.15) and (2.2.16) show the relationship between the refractive index of the materials and the response of the charged particles in the material to the oscillatory electric field $\vec{E}$. The response is represented by the polarizability α [43].

2.3 Interaction of the electromagnetic wave with dielectric medium

In this section we briefly discuss the specific case of the interaction of the EM with materials. Though the concept of the interactions of the EM waves with matter are generally explained with Quantum Mechanics, there are many situations when the classical EM theory gives a practically compete illustration. These include interesting phenomena like resonances inside an atom or molecule. Quantum Mechanics alone can account for the presence of these phenomena, however, it turns out to be suitable and illuminating to consider absorption and dispersion of the EM waves by the individual atoms and charges due to a classical EM approach [43].

Absorption with dispersion, describes the response of the materials to the applied EM waves. The interaction of the EM waves with electrons, particles and nuclei at a microscopic scale can be treated with EM phenomena [20]. The applied electric field of the EM waves in the medium induces electric dipole moments which is influenced by the EM properties of the medium. A good description of this phenomena could be provided by the classical Lorentzian model which we shall discuss in the next section [20].

2.3.1 Lorentz Model

Considering that a system with a bound charge oscillating about its equilibrium position with a very small amplitude, the response of such oscillators to the incident electric field of the EM wave can be derived, and calculated through the absorption or dispersion radiation from an individual oscillator. The model of this system can be represented as a simple harmonic oscillator as shown in Figure 2.1. The potential energy ($U(x)$) of the charged particle is quadratic for small displacements from the equilibrium position [20, 38, 43].

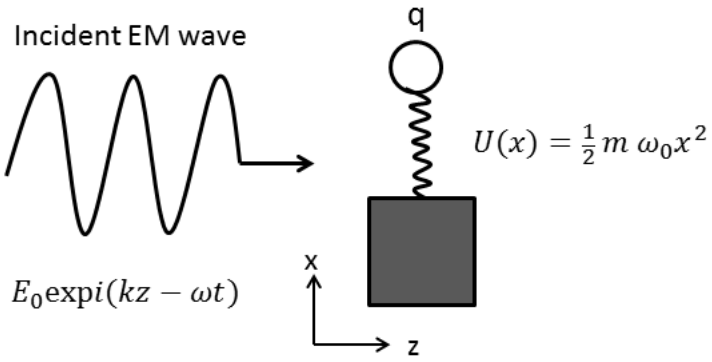

Figure 2.1: The Lorentz model accounts for the optical response of bound charges in dielectric material [20].

When the incoming EM wave ($\vec{E}(t) = \vec{E}_0 \exp(-i\omega t)$) of angular frequency ω, polarized along the x axis, interacts with a mass m and charge q, as seen in Figure 2.1, then the expression for the equation of motion can be given by [20, 38, 43]

$$\frac{d^2\vec{x}}{dt^2} + \gamma \frac{d\vec{x}}{dt} + \omega_0^2 \vec{x} = \frac{q}{m}\vec{E}(t), \tag{2.3.1}$$

where γ is the damping constant and ω_0 is the undamped resonant frequency. The solution of the equation of this motion can be written as [20, 43]

$$x(t) = x_0 \exp(-i\omega t), \quad \text{where, } x_0 = \frac{q}{m} \frac{\vec{E}_0}{\omega_0^2 - \omega^2 - i\omega\gamma}. \tag{2.3.2}$$

The electric dipole moment of the harmonic oscillator can be given by $\vec{p}(t) = qx(t)$. By assuming that the material has a number of oscillators N per unit volume, then the expression of the polarization of the material becomes [20, 43]

$$\vec{P}(t) = Nqx(t) = \frac{Nq^2}{m} \frac{\vec{E}_0 \exp(-i\omega t)}{\omega_0^2 - \omega^2 - i\omega\gamma} \equiv \epsilon_0 \chi_e(\omega) \vec{E}_0 \exp(-i\omega t), \tag{2.3.3}$$

where $\chi_e(\omega)$ is the linear electric susceptibility of the material. By substituting Eq. 2.3.3 into Eq. 2.2.10, we have [20, 43]

$$\epsilon_r(\omega) = \frac{\epsilon(\omega)}{\epsilon_0} = 1 + \chi_e(\omega) = 1 + \frac{Nq^2}{m\epsilon_0} \frac{1}{\omega_0^2 - \omega^2 - i\omega\gamma}, \tag{2.3.4}$$

where $\epsilon_r(\omega)$ is defined in section 2.2.

From Eq. 2.3.4 the expression for the real and imagineary parts of the complex dielectric constant of the material can be written as [20, 43]

$$n(\omega) = 1 + \frac{Nq^2}{m\epsilon_0} \frac{\omega_0^2 - \omega^2}{(\omega_0^2 - \omega^2)^2 + \omega^2\gamma^2}, \tag{2.3.5}$$

and

$$\kappa(\omega) = \frac{Nq^2}{m\epsilon_0} \frac{\omega\gamma}{(\omega_0^2 - \omega^2)^2 + \omega^2\gamma^2}. \tag{2.3.6}$$

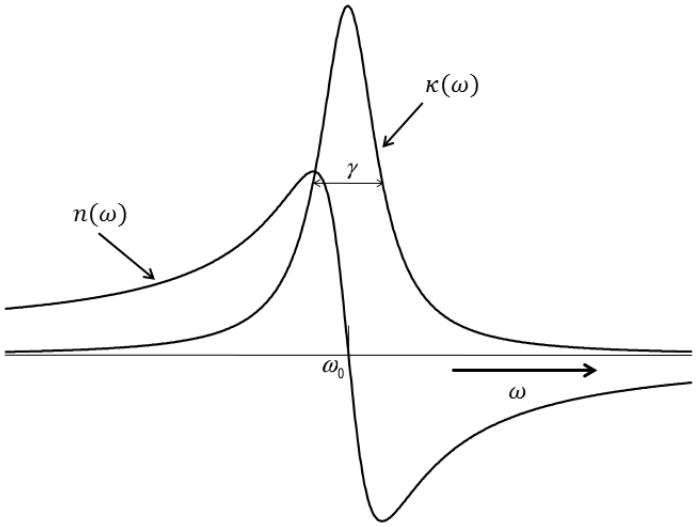

Figure 2.2: The change of the refractive index $n(\omega)$ and the extinction coefficient $\kappa(\omega)$ in the region of the resonant frequency [20, 43].

Figure 2.2 shows the spectral behaviour of the refractive index and the extinction coefficient in the vicinity of the resonant frequency. The refractive index increases as the frequency increases. However, at the resonant frequency ω_0 the refractive index typically drops sharply and it is known as anomalous dispersion, while the absorption coefficient is at its maximum value and its bandwidth is approximately γ [20, 43, 10].

2.4 Beer-Lambert law

In optics, that part of physics which deals with the characteristics of light, the total photon energy transmitted through a unit area in a given unit of time is known as the intensity (I). By comparing the incident intensity of light through the sample (I_0), with the intensity of light coming out from the sample (I), and taking the ratio between them I/I_0, to obtain an indication of what fraction of the incoming light in the sample was found going through the sample. This ratio known as the Transmittance T, which given by [33, 9]

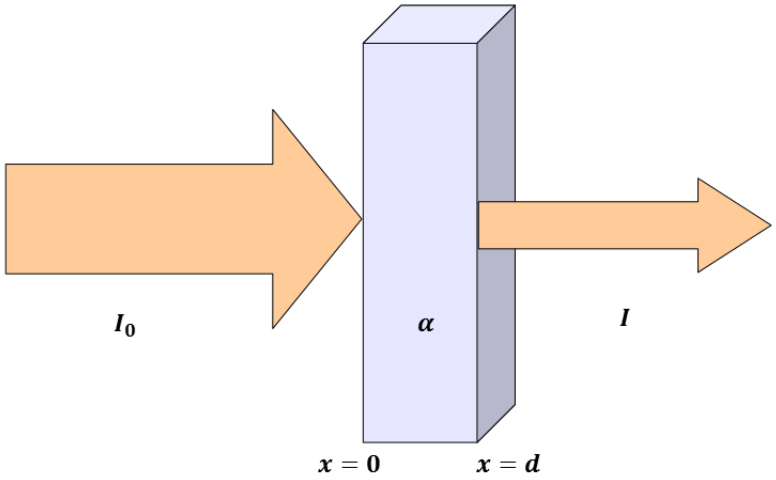

Figure 2.3: The change of intensity along the sample with thickness d.

$$T = \frac{I}{I_0}. \tag{2.4.1}$$

The absorbance A is the measurement of how much light can be absorbed by the sample, which is given by [33, 9]

$$A = -\ln T = -\ln \frac{I}{I_0}. \tag{2.4.2}$$

2.4.1 Derivation of the Beer-Lambert law

Generally, we can write the equation which describes the incident electric field of the electromagnetic wave on the material with complex refractive index as in Eq. 2.2.14

$$\vec{E} = E_0 \exp(-\kappa \vec{k_0}.\vec{x}) \exp[i(n \vec{k_0}.\vec{x} - \omega t)]. \tag{2.4.3}$$

Since the intensity can be expressed in term of the electric field $\vec{E}$, as [43]

$$I = \vec{E} \cdot \vec{E}^*, \tag{2.4.4}$$

where $\vec{E}^*$, is the complex conjugate of the electric field.

Now by substituting Eq. 2.4.3 into Eq. 2.4.4, we have

$$I(x) = E_0^2[\exp(-\kappa \vec{k_0}.\vec{x}) \exp(-\kappa \vec{k_0}.\vec{x}) \exp[i(n \vec{k_0}.\vec{x} - \omega t)] \exp[-i(n \vec{k_0}.\vec{x} - \omega t)]], \tag{2.4.5}$$

$$= E_0^2 \exp(-2\kappa \vec{k_0}.\vec{x}). \tag{2.4.6}$$

From Figure 2.3, the intensity at the boundary of the material at $(\vec{x} = 0)$, can be written as

$$I(0) = E_0^2, \tag{2.4.7}$$

and the intensity after passing through the material at ($\vec{x} = d$), can be written as

$$I_d = I_0 \exp(-2\kappa \vec{k_0}\, d), \tag{2.4.8}$$
$$= I_0 \exp(-\alpha\, d), \tag{2.4.9}$$

where d is the real thickness of the material, and $\alpha = (2\kappa \vec{k_0})$ represents the absorption coefficient.

Now we can write the Transmittance T, as [33, 9]

$$T = \frac{I_d}{I_0} = \exp(-\alpha\, d), \tag{2.4.10}$$

by taking the logarithm of Eq. 2.4.10, then we have

$$\ln T = \ln \frac{I_d}{I_0} = -\alpha\, d. \tag{2.4.11}$$

From Eq. 2.4.11, the absorbance A, can be written as [33, 9]

$$A = -\ln T = -\ln \frac{I_d}{I_0} = \alpha\, d. \tag{2.4.12}$$

Now we wish to write the Beer-Lambert law in terms of the electric field in order to obtain the complex refractive index of the samples [21].

From Eq. 2.4.3 the incident electric field of the EM wave on the sample can also be written as in Eq. 2.2.13 [43, 21]

$$E = E_0 \exp[-i(\tilde{k}(\omega).x - \omega t)]. \tag{2.4.13}$$

By considering the electric field at the boundary of the sample (when the electric field is at the front of the sample) such as ($x = 0$), this implies that Eq. 2.4.13 becomes [21]

$$E(x = 0) = E_0 \exp[-i(-\omega t)], \tag{2.4.14}$$

for the case of the electric field at the back of the sample (at $x = d$), then Eq. 2.4.13 becomes [21]

$$E(x = d) = E_0 \exp[-i(\tilde{k}(\omega)d - \omega t)] = E(0) \exp[-i(\tilde{k}(\omega))d]. \tag{2.4.15}$$

where the angular wave number $\tilde{k}(\omega)$ is given by [21]

$$\tilde{k}(\omega) = \frac{\omega}{c}\tilde{n}(\omega), \tag{2.4.16}$$

where $\tilde{n}$ is defined in Eq. 2.2.15.

In a vacuum, $\tilde{n}(\omega) = 1$, thus Eq. 2.4.16 becomes

$$\tilde{k}_{\text{ref}}(\omega) = \frac{\omega}{c}. \tag{2.4.17}$$

In the sample, the expression for $\tilde{k}(\omega)$ becomes [21]

$$\tilde{k}_{\text{sam}}(\omega) = \frac{\omega}{c}[n(\omega) + i\kappa(\omega)] = \frac{\omega}{c} + \frac{\omega}{c}[n(\omega) - 1] + i\frac{\alpha(\omega)}{2}. \tag{2.4.18}$$

Now, by considering the E-field at the back of the sample and the E-field without the sample present, we can write Eq. 2.4.15 as

$$E(d)_{\text{sam}} = E(0)\exp[-i(\tilde{k}_{\text{sam}}(\omega)d], \tag{2.4.19}$$

and

$$E(d)_{\text{ref}} = E(0)\exp[-i(\tilde{k}_{\text{ref}}(\omega)d]. \tag{2.4.20}$$

We can write the ratio of Eqs. 2.4.19 and 2.4.20 as [21]

$$\frac{E(d)_{\text{sam}}}{E(d)_{\text{ref}}} = \frac{E(0)\exp[-i(\tilde{k}_{\text{sam}}(\omega)d]}{E(0)\exp[-i(\tilde{k}_{\text{ref}}(\omega)d]} = \exp[-i(\tilde{k}_{\text{sam}}(\omega) - \tilde{k}_{\text{ref}}(\omega))d], \tag{2.4.21}$$

by substituting Eqs. 2.4.17 and 2.4.18 into Eq. 2.4.21, we have

$$\frac{E(d)_{\text{sam}}}{E(d)_{\text{ref}}} = \exp[-i(\frac{\omega}{c}[n(\omega) - 1] + i\frac{\alpha(\omega)}{2})d]. \tag{2.4.22}$$

In the experiment, E_{sam} and E_{ref} are measured in time domain as real quantities ($E_{\text{sam}}(t)$ and $E_{\text{ref}}(t)$). The complex representation of the E-field in the frequency domain will be obtained via a fast Fourier transform [21],

$$\frac{E(d,\omega)_{\text{sam}}}{E(d,\omega)_{\text{ref}}} = \exp[-i(\frac{\omega}{c}[n(\omega) - 1] + i\frac{\alpha}{2}(\omega))d]. \tag{2.4.23}$$

By taking the natural logarithm of Eq. 2.4.23, we can write [21]

$$\ln\left(\frac{E(d,\omega)_{\text{sam}}}{E(d,\omega)_{\text{ref}}}\right) = -i\frac{\omega}{c}d[n(\omega) - 1] + \frac{\alpha(\omega)}{2}d. \tag{2.4.24}$$

In our experiment, E_{sam} and E_{ref} have been recorded respectively as

$$E(d,\omega)_{\text{sam}} = E_{0\text{sam}}\exp(-i\phi_{\text{sam}}), \tag{2.4.25}$$

and

$$E(d,\omega)_{\text{ref}} = E_{0\text{ref}}\exp(-i\phi_{\text{ref}}). \tag{2.4.26}$$

Where ϕ_{ref} is the phase of the THz pulse before passing through sample, and ϕ_{sam} is the phase of the THz pulse after it has propagated through the sample.

The ratio of Eqs. 2.4.25 and 2.4.26 can be written in the form

$$\frac{E(d,\omega)_{\text{sam}}}{E(d,\omega)_{\text{ref}}} = \frac{E_{0\text{sam}}}{E_{0\text{ref}}}\exp[i(\phi_{\text{ref}} - \phi_{\text{sam}})]. \tag{2.4.27}$$

So that the natural logarithm of Eq. 2.4.27 is written as

$$\ln\left(\frac{E(d,\omega)_{\text{sam}}}{E(d,\omega)_{\text{ref}}}\right) = \ln\left(\frac{E_{0\text{sam}}}{E_{0\text{ref}}}\right) + i(\phi_{\text{ref}} - \phi_{\text{sam}}). \tag{2.4.28}$$

The real and imaginary parts of both Eqs. 2.4.24 and 2.4.28 which represent the refractive index and the absorption coefficient can respectively be extracted as

$$n(\omega) = \left[(\phi_{\text{ref}} - \phi_{\text{sam}})\frac{c}{\omega d}\right] + 1, \tag{2.4.29}$$

and

$$\alpha(\omega) = 2\left[\ln\left(\frac{E_{0\text{sam}}}{E_{0\text{ref}}}\right)\right]/d. \tag{2.4.30}$$

2.5 Birefringence

Birefringence is an optical characteristic of materials. Materials that are optically anisotropic are known as birefringent. Generally many crystals are sensitive to the direction of the electric field of the incident wave. There are some crystals that may have two characteristic orthogonal optical axes, which we call axis 1 and axis 2, as shown in Figure 5.3.1. This phenomenon is known as birefringence [25]. When linear-polarized light is incident on the material parallel or perpendicular to the optical axes, it has unequal refractive indices known as extraordinary and ordinary denoted by n_e and n_o respectively [19].

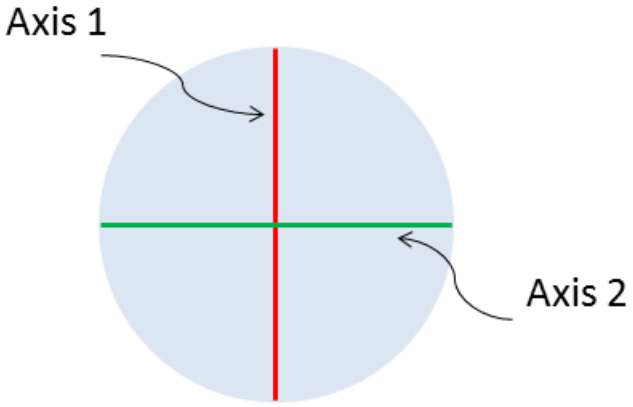

Figure 2.4: The two orthogonal axes of the crystal [25].

Now we wish to discuss all possible cases to illustrate the birefringence of a crystal. We consider two orthogonal polarization components of the incident wave on crystal surface, each along one of the axes. Let consider that the material has no absorption, meaning that the imaginary part of the refractive index ($\kappa = 0$). We can write the equation which describe the incident electric field on the material crystal as [38]

$$\vec{E} = \vec{E_0} \exp i(\vec{k}.\vec{x} - \omega\, t), \tag{2.5.1}$$

where $\vec{E_0}$ is the amplitude constant in time, and $k = \frac{2\pi\, n}{\lambda_0} = n\,\frac{\omega}{c} = nk_0$ is the wave number, also called propagation vector, λ_0 is the wavelength in vacuum [38] and k_0 is the wave number in vacuum.

Case I. If the polarization of the incident wave is parallel to the axis 1 or axis 2 of the material crystal, then the transmitted waves can pass without changing its polarization state, and the polarization is described as if the material crystal had either refractive indices n_1 or n_2 [25].

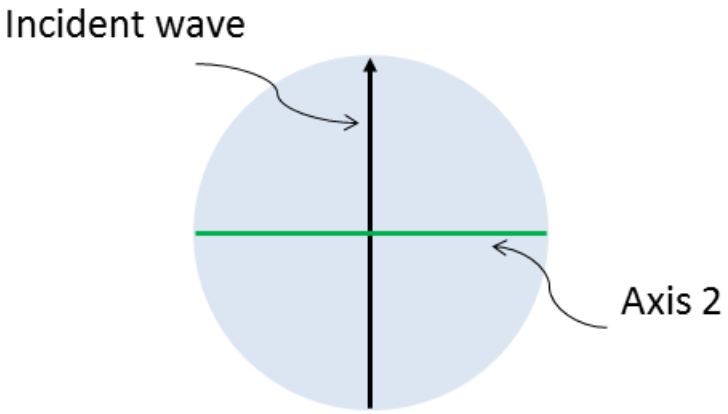

Figure 2.5: The polarization of the incident wave is parallel to axis 1. For this wave the refractive index is n_1 [25].

For the incident polarization parallel to axis 1 (as illustrated in Figure 2.5) the equation of the wave inside the birefringent crystal can be written as [38]

$$\vec{E} = \vec{E_0} \exp i([\vec{k}(\vec{x} - d) + \vec{k}\, n_1 d - \omega\, t]), \tag{2.5.2}$$

where d is the thickness of the sample.

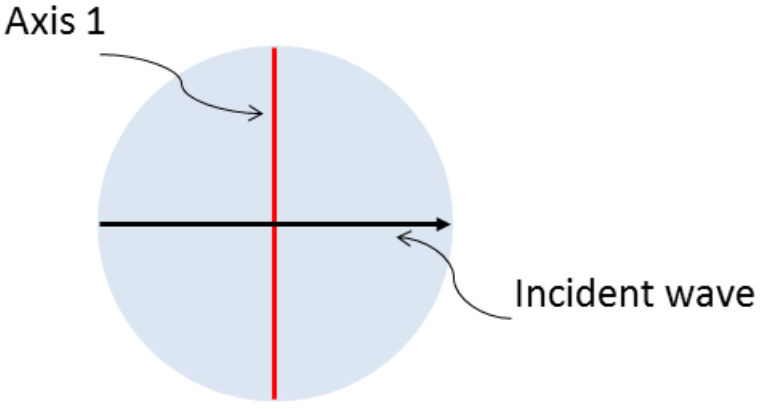

Figure 2.6: The second case for when the polarization of the incident wave is parallel to axis 2. For this wave the refractive index is n_2 [25].

For the incident polarization parallel to axis 2 (as illustrated in Figure 2.6) the equation of the wave inside the birefringent crystal can be written as [38]

$$\vec{E} = \vec{E_0} \exp i([\vec{k}(\vec{x} - d) + \vec{k}\, n_2 d - \omega\, t]), \tag{2.5.3}$$

Case III. If the direction of polarization of the incident wave makes an angle θ with axis 1, the transmitted wave has a more complicated polarization state, and the wave behaviour can be seen as the superposition of two waves with a different phases. The one wave can be considered oscillating in a plane which has refractive index n_1 and the other wave oscillate in a plane (perpendicular to the previously mentioned plane) which has a refractive index n_2.

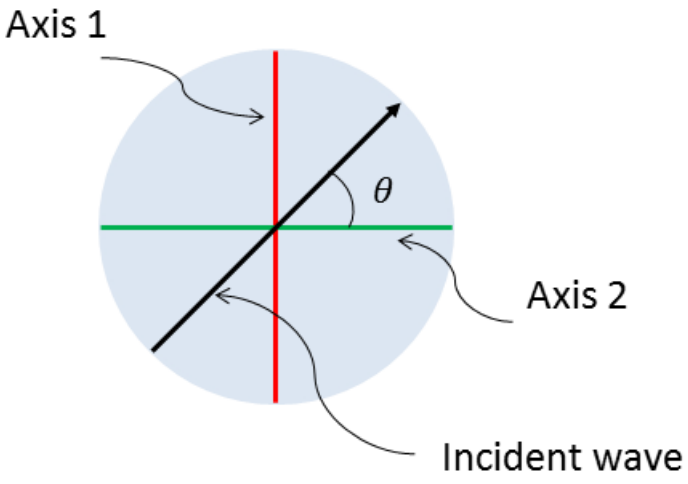

Figure 2.7: The third case, when the polarization of the incident wave makes an angle θ with axis 1. For this wave the refractive indices are n_1 and n_2 [25].

In the real field notation or in the complex field notation, we can write the equation of the incident electric field on the material crystal as [38]

$$\vec{E} = E_0\, [\cos\theta \exp i([\vec{k}(\vec{x} - d) + \vec{k}\, n_1 d - \omega\, t]) + \sin\theta \exp i([\vec{k}(\vec{x} - d) + \vec{k}\, n_2 d - \omega\, t])]. \tag{2.5.4}$$

2.6 Fresnel's equations

Fresnel equations are a set of equations that can be used to describe the behaviour of light at the interface between different media. Different media have their own optical properties such as reflection and transmission coefficients. In this section we will show how the Fresnel equations describe the reflection and transmission of the light wave incidence on a boundary of two media. We will also show how to get the reflection and transmission coefficients in all cases of the plane wave incidence i.e., both parallel and perpendicular to the plane of incidence at the interface. And we will use Snell's law to compute the incident and transmitted angles, because Fresnel equations can be stated in terms of the angles of the incidence and transmission [12].

The equation of the incident electric field on a boundary of two homogeneous, isotropic, lossless dielectric media can be written as [12]

$$\vec{E_i} = \vec{E_{0i}} \exp(i\ \vec{k_i}.\vec{r} - \omega_i t), \tag{2.6.1}$$

where E_i is the electric field of the incident wave, E_{0i} is the amplitude constant in time, and ω_i is the angular frequency [12]. We can rewrite Eq. 2.6.1 as

$$\vec{E_i} = \vec{E_{0i}} \cos(\vec{k_i}.\vec{r} - \omega_i t). \tag{2.6.2}$$

Then the reflected and transmitted waves are given in the following form

$$\vec{E_r} = \vec{E_{0r}} \cos(\vec{k_r}.\vec{r} - \omega_r t + \varepsilon_r). \tag{2.6.3}$$

$$\vec{E_t} = \vec{E_{0t}} \cos(\vec{k_t}.\vec{r} - \omega_t t + \varepsilon_t), \tag{2.6.4}$$

where ε_r and ε_t are the phase constants for reflected and transmitted waves relative to the incident wave respectively [12].

From the reflection law, which is defined as $(\theta_i = \theta_r)$, and Snell's law which can be written as [12]

$$n_i \sin\theta_i = n_t \sin\theta_t. \tag{2.6.5}$$

where n_i and n_t are refractive indices of the incident and transmission media, θ_i and θ_r are the incident and transmitted angles, we can obtain the formulas of the reflection and transmission coefficients of the Fresnel's equation in two cases [12]

Case I: If the $\vec{E}$-field is perpendicular to the plane of incidence, then the magnetic field must be parallel to it, as shown in Figure 2.8 [12].

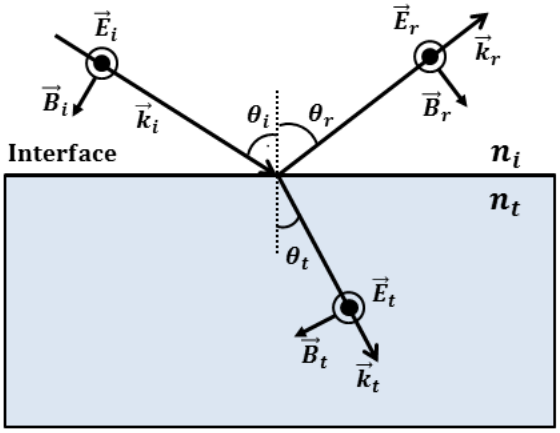

Figure 2.8: An incoming light whose electric field is normal to the plane of incidence [12].

In this case the Fresnel's equations for the dielectric media can be written as follows [12]

$$r_\perp \equiv \left(\frac{E_{0r}}{E_{0i}}\right)_\perp = \frac{n_i \cos\theta_i - n_t \cos\theta_t}{n_i \cos\theta_i + n_t \cos\theta_t}, \tag{2.6.6}$$

and

$$t_{\perp} \equiv \left(\frac{E_{0t}}{E_{0i}}\right)_{\perp} = \frac{2n_i \cos\theta_i}{n_i \cos\theta_i + n_t \cos\theta_t}, \tag{2.6.7}$$

where $r_{\perp}$ and $t_{\perp}$ are the amplitude reflection and transmission coefficients respectively [12].

Case II: $\vec{E}$-field parallel to plane of incidence, and $\vec{B}$ is perpendicular to it, as shown in Figure 2.9.

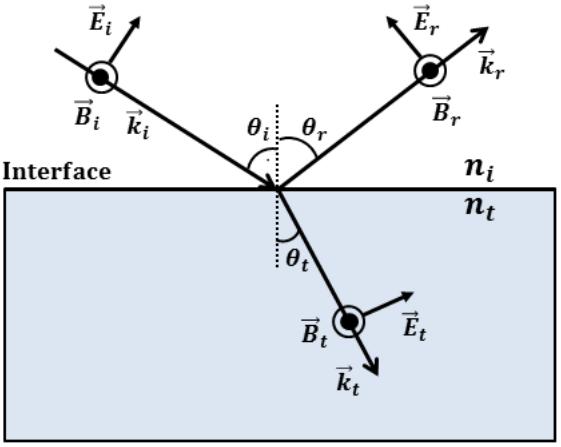

Figure 2.9: An incoming light whose electric field is in the plane of incidence [12].

Then we can obtain the second set of the Fresnel's equations for the dielectric media, can be written as [12]

$$r_{\parallel} \equiv \left(\frac{E_{0r}}{E_{0i}}\right)_{\parallel} = \frac{n_t \cos\theta_i - n_i \cos\theta_t}{n_i \cos\theta_t + n_t \cos\theta_i}, \tag{2.6.8}$$

and

$$t_{\parallel} \equiv \left(\frac{E_{0t}}{E_{0i}}\right)_{\parallel} = \frac{2n_i \cos\theta_i}{n_i \cos\theta_t + n_t \cos\theta_i}. \tag{2.6.9}$$

For more simplification, by using Snell's law we can rewrite the Fresnel's equations for non-magnetic media as [12]

$$r_{\perp} \equiv \left(\frac{E_{0r}}{E_{0i}}\right)_{\perp} = -\frac{\sin(\theta_i - \theta_t)}{\sin(\theta_i + \theta_t)}, \tag{2.6.10}$$

$$t_{\perp} \equiv \left(\frac{E_{0t}}{E_{0i}}\right)_{\perp} = +\frac{2\sin\theta_t \cos\theta_i}{\sin(\theta_i - \theta_t)}, \tag{2.6.11}$$

$$r_{\parallel} \equiv \left(\frac{E_{0r}}{E_{0i}}\right)_{\parallel} = +\frac{\tan(\theta_i - \theta_t)}{\tan(\theta_i + \theta_t)}, \tag{2.6.12}$$

$$t_{\parallel} \equiv \left(\frac{E_{0t}}{E_{0i}}\right)_{\parallel} = +\frac{2\sin\theta_t \cos\theta_i}{\sin(\theta_i + \theta_t)\cos(\theta_i - \theta_t)}. \tag{2.6.13}$$

2.6.0.1 Amplitude coefficients at a normal incidence

At a normal incidence, the angle of the incident light is zero ($\theta_i \simeq 0$). In this case we can write the forms of the amplitude coefficients as [12]

$$[r_{\parallel}]_{\theta_i=0} = [-r_{\perp}]_{\theta_i=0} = r = \frac{n_t - n_i}{n_t + n_i}, \tag{2.6.14}$$

and

$$[t_{\parallel}]_{\theta_i=0} = [t_{\perp}]_{\theta_i=0} = \frac{2n_i}{n_i + n_t}. \tag{2.6.15}$$

A plot of the transmission and reflection coefficients ($r_{\perp}$, $r_{\parallel}$, $t_{\perp}$ and $t_{\parallel}$) is shown in Figure 2.10 [12].

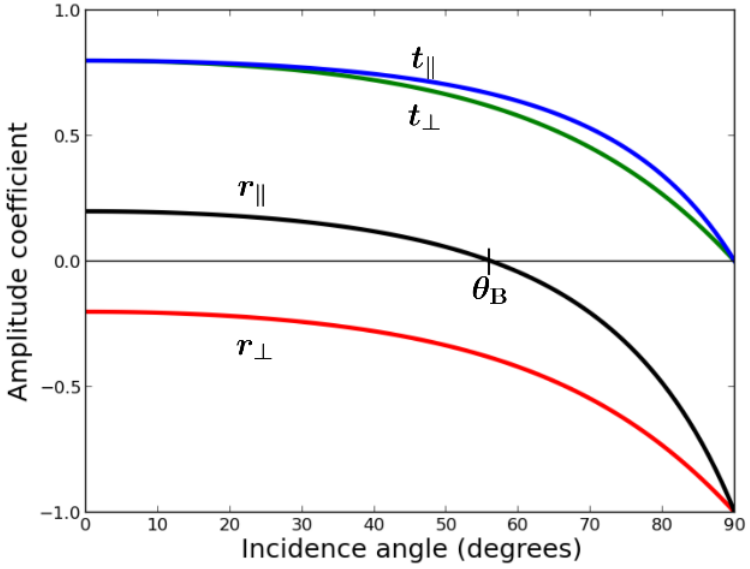

Figure 2.10: A graph showing the amplitude coefficients of reflection and transmission as a function of incident angle, in case of external reflection (i.e $n_t > n_i$) with $n_i = 1$ and $n_t = 1.5$ [12].

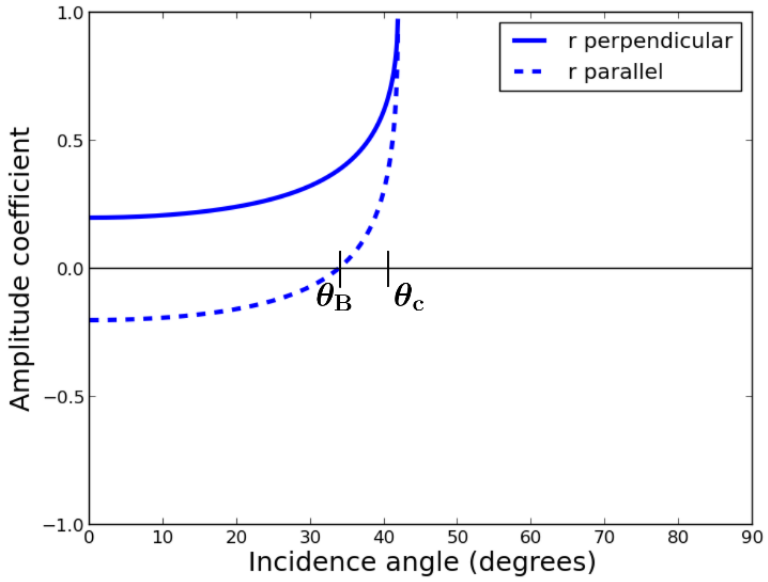

Figure 2.11: A graph showing the amplitude coefficients of reflection and transmission as a function of incident angle, in case of total internal reflection (i.e $n_t < n_i$) with $n_i = 1$ and $n_t = 1.5$ [12].

2.6.1 Reflectance and transmittance

For electromagnetic fields incident on dielectric media interfaces, part of the fields will be reflected from the media interface and the other part will be transmitted through the media. Both electric (E) and magnetic (B) fields obey the boundary condition. Using this boundary condition we determine the ratios of the incident amplitude field to the reflected and transmitted amplitudes fields, as discussed in section 2.6. Here we briefly discuss the concept of the reflectance and transmittance [20, 12].

The reflectance R is defined as the ratio of the reflected intensity to the incident intensity, and the transmittance T is defined as the ratio of the transmitted intensity to the incident intensity. Their expressions can be written as [20, 12]

$$R = \frac{I_r}{I_i} = \left(\frac{E_{0r}}{E_{0i}}\right)^2 = r^2, \tag{2.6.16}$$

and

$$T = \frac{I_t}{I_i} = \frac{n_t \cos\theta_t}{n_i \cos\theta_i}\left(\frac{E_{0t}}{E_{0i}}\right)^2 = \left(\frac{n_t \cos\theta_t}{n_i \cos\theta_i}\right) t^2. \tag{2.6.17}$$

Where r and t are equal to $\left(\frac{E_{0r}}{E_{0i}}\right)$ and $\left(\frac{E_{0t}}{E_{0i}}\right)$, respectively [20, 12].

The reflectance's expressions for the parallel and perpendicular polarized wave can be written as [20, 12]

$$R_\parallel = r_\parallel^2, \quad \text{and } R_\perp = r_\perp^2. \tag{2.6.18}$$

The transmittance's expressions for the parallel and perpendicular polarized wave can be written as [20, 12]

$$T_{\parallel} = \left(\frac{n_t \cos\theta_t}{n_i \cos\theta_i}\right) t_{\parallel}^2. \tag{2.6.19}$$

and

$$T_{\perp} = \left(\frac{n_t \cos\theta_t}{n_i \cos\theta_i}\right) t_{\perp}^2. \tag{2.6.20}$$

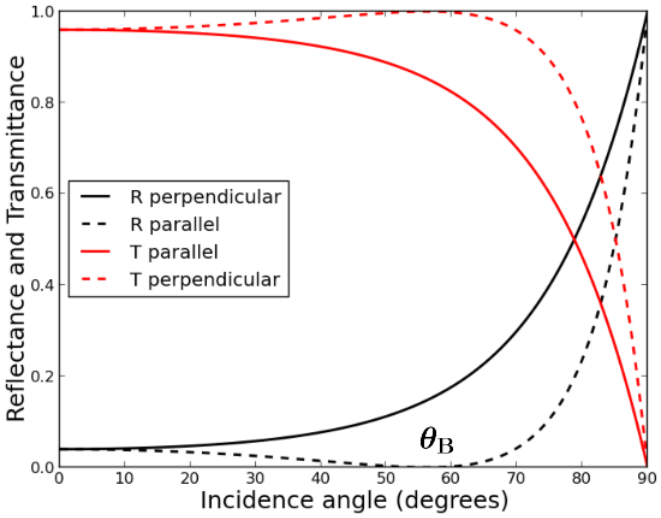

Figure 2.12: A plot of the reflectance and transmittance versus incidence angle for internal reflection ($n_i = 1$, $n_t = 1.5$).

Figure 2.12 shows the behaviour of the reflectance and transmittance of the parallel and perpendicular polarized waves versus incidence angle for the $n_i = 1$ and $n_t = 1.5$. At the Brewster's angle (θ_B), the reflectance component of the parallel polarization is completely exterminated while the transmittance component of the parallel polarization goes to the maximum value as can be seen in Figure 2.12 [20, 12].

2.6.2 Polarization at Brewster's angle

In this section we wish to discuss how the parallel and perpendicular components of incident light is effect at each interface of the sample (with parallel interfaces), when it's placed at the Brewster's angle. We will calculate how much of the light is reflected and transmitted at each interface. We will then calculate the effects of adding more samples at equal spacing. This is done in order to show that this method can be used to polarize light by making use of the Brewster's angle.

When linearly polarized light that is polarized parallel to the plane of incidence is incident on a surface, we find from the Fresnel's equations that for the condition ($\theta_i + \theta_t = 90°$) there will be

no light reflected from the surface, it follows that the incident linearly polarized light is totally transmitted. This condition is called the Brewster's condition [12].

Now if the incident light is unpolarized, we consider to consist two orthogonal linear polarizations, then from the Fresnel equations we find that at a Brewster's angle only light polarized perpendicular to the plane of incidence will be reflected [12]. These situations are shown in Figure 2.13.

Let us consider Figure 2.13 to derive the expressions for the perpendicular and parallel components of the unpolarized light through a medium. Using the Brewster's angle condition, i.e. $\theta_B + \theta_t = 90°$ together with Snell's law, we have that [12]

$$\tan\theta_B = \frac{n_2}{n_1} \Rightarrow \theta_B = \arctan\left(\frac{n_2}{n_1}\right), \tag{2.6.21}$$

where n_1 is the refractive index of air and n_2 is the refractive index of the medium. For a Silicon sample $n_2 = 3.5$, the Brewster angle is given by $\theta_B = \arctan(3.5) \simeq 74.1°$. Again using Snell's law we can calculate the corresponding angle of refraction θ_t, as $\theta_t = \arcsin(\frac{n_1}{n_2}\sin\theta_B) \simeq 15.9°$.

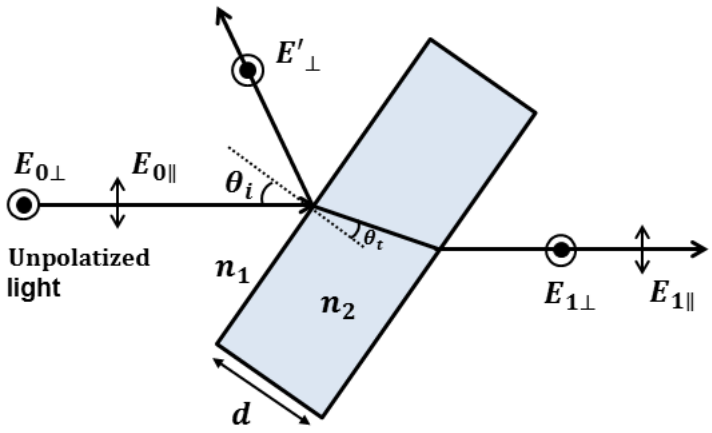

Figure 2.13: Unpolarized light incident on a medium at Brewster's angle [12].

From Figure 2.13, we can write the expressions for the electric field components of the transmitted polarized light as follows [12]

$$E_{1\perp} = E_{0\perp} \times t_{12\perp} \times t_{21\perp}, \tag{2.6.22}$$

and

$$E_{1\parallel} = E_{0\parallel} \times t_{12\parallel} \times t_{21\parallel}, \tag{2.6.23}$$

where $E_{1\perp}$ and $E_{1\parallel}$ are the transmitted orthogonal polarized light components and $E_{0\perp} = E_{0\parallel} = 1$ are the assumed initial electric fields of the unpolarized incident light [12].

θ_i' is angle of incidence at the second interface of the sample. Since the sample has parallel interfaces, then by using Snell's law we are able to derive the expression for the θ_i' as $\theta_i' = \arcsin(\frac{n_1}{n_2}\sin\theta_i)$, which is equal to θ_t geometrically.

By applying Eqs. 2.6.7 and 2.6.9, we have

$$t_{12\perp} = \left[\frac{2n_1\cos\theta_i}{n_1\cos\theta_i + n_2\cos\theta_t}\right], \quad \text{and} \quad t_{21\perp} = \left[\frac{2n_2\cos\theta_i'}{n_1\cos\theta_i + n_2\cos\theta_i'}\right], \tag{2.6.24}$$

and

$$t_{12\parallel} = \left[\frac{2n_1\cos\theta_i}{n_1\cos\theta_t + n_2\cos\theta_i}\right], \text{ and } t_{21\parallel} = \left[\frac{2n_2\cos\theta_i'}{n_1\cos\theta_i' + n_2\cos\theta_i}\right]. \tag{2.6.25}$$

Now substituting Eqs. 2.6.24 and 2.6.25 into Eqs. 2.6.22 and 2.6.23, respectively, one can obtain the following

$$E_{1\perp} = E_{0\perp}\left[\frac{2n_1\cos\theta_i}{n_1\cos\theta_i + n_2\cos\theta_t}\right]^2\left[\frac{2n_2\cos\theta_i'}{n_1\cos\theta_i + n_2\cos\theta_i'}\right], \tag{2.6.26}$$

and

$$E_{1\parallel} = E_{0\parallel}\left[\frac{2n_1\cos\theta_i}{n_2\cos\theta_i + n_1\cos\theta_t}\right]^2\left[\frac{2n_2\cos\theta_i'}{n_2\cos\theta_i + n_1\cos\theta_i'}\right]. \tag{2.6.27}$$

Let us define the ratio of the two polarized light electric fields (V), as

$$V = \frac{E_{1\perp}}{E_{1\parallel}} = \frac{E_{0\perp}\left[n_2\cos\theta_i + n_1\cos\theta_t\right]^2}{E_{0\parallel}\left[n_1\cos\theta_i + n_2\cos\theta_t\right]^2}. \tag{2.6.28}$$

For light incident from air ($n_1 = 1$) on a Silicon sample ($n_2 = 3.5$) at Brewster's angle, Eqs. 2.6.26 and 2.6.27 yields $E_{1\perp} = 7.78 \times 10^{-2}$ and $E_{1\parallel} = 1.0$, respectively. This implies that $V = 7.78 \times 10^{-2}$.

If we add more samples (every sample has two surfaces), by applying the same method, then the resultant ratio of polarization can be derived. The results are summarized in Table 2.1.

m	1	2	3	4	5
V	7.78×10^{-2}	6.05×10^{-3}	4.71×10^{-4}	3.66×10^{-5}	2.85×10^{-6}

Table 2.1: The ratio of the two polarizations for m number of Silicon samples.

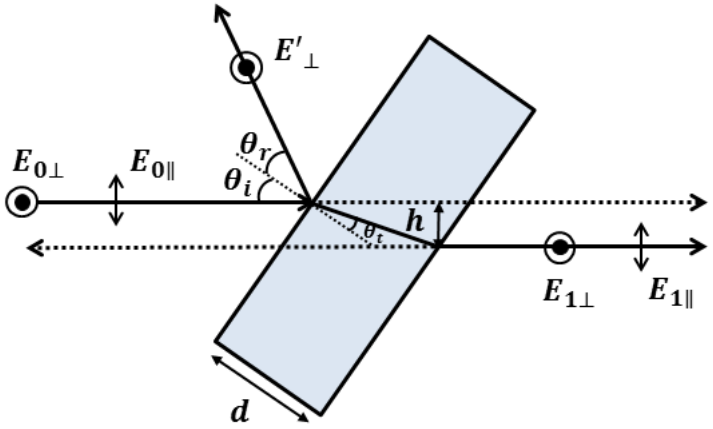

Figure 2.14: Incident unpolarized light on a medium at Brewster's angle with the perpendicular distance h between the incident light and the transmitted light [12].

The distance between the incident light and the transmitted light (h), as shown in Figure 2.14, can be given by

$$h = d\left[\frac{\sin(\theta_i - \theta_t)}{\cos(\theta_t)}\right]. \tag{2.6.29}$$

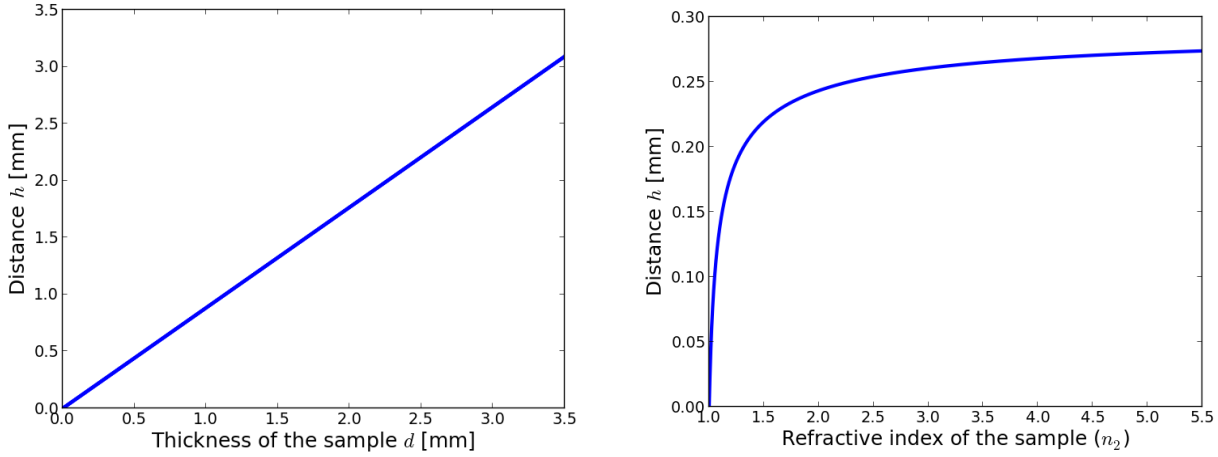

(a) (b)

Figure 2.15: (a) The distance between the incident light and transmitted light versus sample thickness (d) for a fixed refractive index, i.e., $n_2 = 3.5$, (b) the distance between the incident light and transmitted light versus refractive index of the sample (n_2) for a fixed sample thickness, i.e., $d = 0.3$ mm.

Figure 2.15(a) shows the variation of the distance between the incident light and transmitted light (h) with respect to sample thickness (d). h is calculated from Eq. 2.6.29 for a fixed refractive index, i.e., $n_2 = 3.5$. Next we vary the refractive index and determine the distance between the incident light and the transmitted light at fixed sample thickness, i.e., $d = 0.3$ mm. The results are shown in Figure 2.15(b).

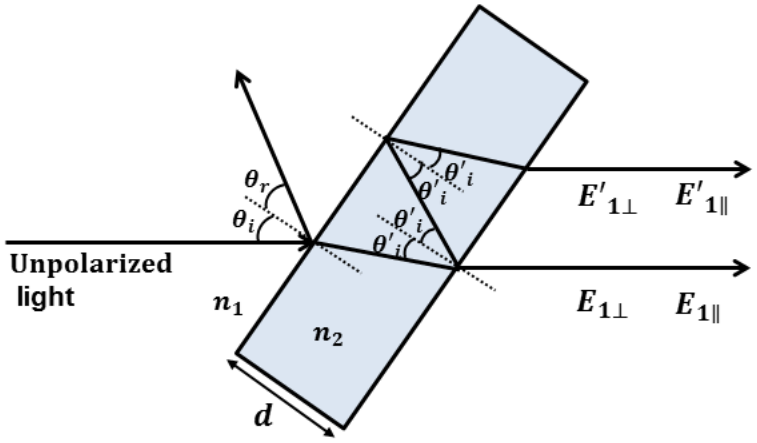

Figure 2.16: Incident unpolarized light on a sample, with the transmitted light after reflection through the sample.

The expressions for the electric field components of the transmitted light after reflection through the sample, as shown in Figure 2.16 can be written as [12]

$$E'_{1\perp} = E_{0\perp} \times t_{12\perp} \times t_{21\perp} \times r_{\perp}^2. \tag{2.6.30}$$

and

$$E'_{1\parallel} = E_{0\parallel} \times t_{12\parallel} \times t_{21\parallel} \times r_{\parallel}^2. \tag{2.6.31}$$

From Fresnel's equations the reflectance can be derived as [12]

$$r_{\perp} = \left[\frac{\sin(\theta_i - \theta_i')}{\sin(\theta_i + \theta_i')}\right], \tag{2.6.32}$$

and

$$r_{\parallel} = \left[\frac{\tan(\theta_i - \theta_i')}{\tan(\theta_i + \theta_i')}\right]. \tag{2.6.33}$$

By substituting Eqs. 2.6.32 and 2.6.33 into Eqs. 2.6.30 and 2.6.31, we have

$$E'_{1\perp} = E_{0\perp} \times t_{12\perp} \times t_{21\perp} \left[\frac{\sin(\theta_i - \theta_i')}{\sin(\theta_i + \theta_i')}\right]^2, \tag{2.6.34}$$

and

$$E'_{1\parallel} = E_{0\parallel} \times t_{12\parallel} \times t_{21\parallel} \left[\frac{\tan(\theta_i - \theta_i')}{\tan(\theta_i + \theta_i')}\right]^2. \tag{2.6.35}$$

By substituting Eqs. 2.6.24 and 2.6.25 into Eqs. 2.6.34 and 2.6.35, we have

$$E'_{1\perp} = E_{0\perp} \left[\frac{2n_1 \cos\theta_i}{n_1 \cos\theta_i + n_2 \cos\theta_t}\right] \left[\frac{2n_2 \cos\theta_i'}{n_1 \cos\theta_i + n_2 \cos\theta_i'}\right] \left[\frac{\sin(\theta_i - \theta_i')}{\sin(\theta_i + \theta_i')}\right]^2, \tag{2.6.36}$$

and

$$E'_{1\parallel} = E_{0\parallel}\left[\frac{2n_1\cos\theta_i}{n_2\cos\theta_i + n_1\cos\theta_t}\right]\left[\frac{2n_2\cos\theta'_i}{n_2\cos\theta_i + n_1\cos\theta'_i}\right]\left[\frac{\tan(\theta_i - \theta'_i)}{\tan(\theta_i + \theta'_i)}\right]^2. \tag{2.6.37}$$

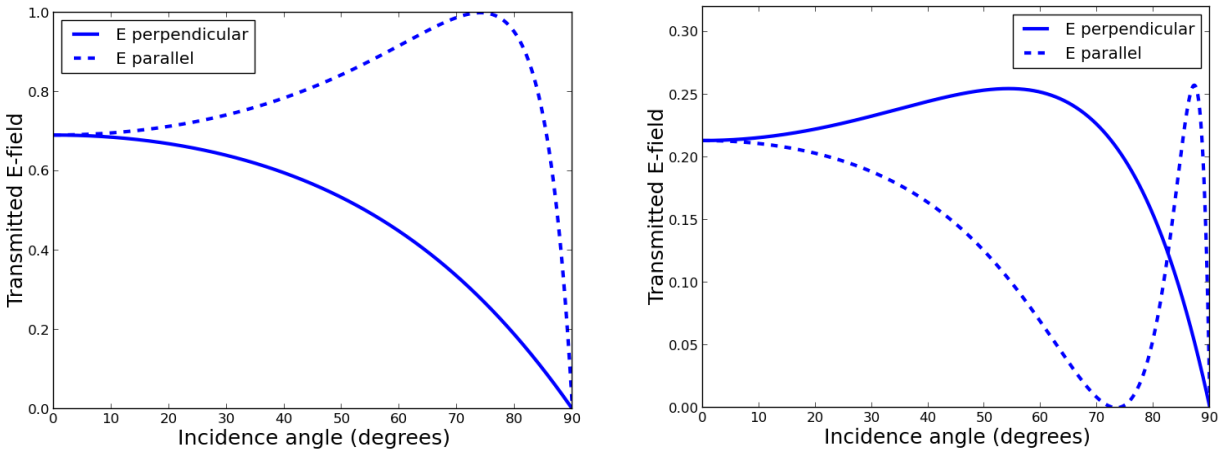

(a) (b)

Figure 2.17: (a) The E-field transmitted after the first pass, $E_{1\perp}$ and $E_{1\parallel}$ versus angle of incidence, and (b) the transmitted E-field after the second pass $E'_{1\perp}$ and $E'_{1\parallel}$ versus angle of the incidence [12].

Figure 2.17(a) shows the variation of the transmitted E-field after the first pass, $E_{1\perp}$ and $E_{1\parallel}$ for the Silicon sample which is calculated using Eqs. 2.6.26 and 2.6.27. The variation of the transmitted E-field with the angle of incidence after the second pass, $E'_{1\perp}$ and $E'_{1\parallel}$ for the Silicon sample which is calculated using Eqs. 2.6.36 and 2.6.37 is shown in Figure 2.17(b).

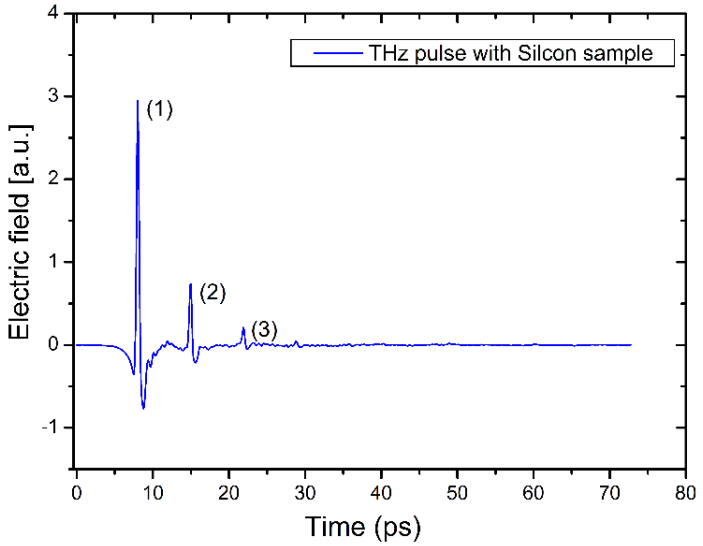

Figure 2.18: The electric field of the THz pulse is plotted versus time with the Silicon sample.

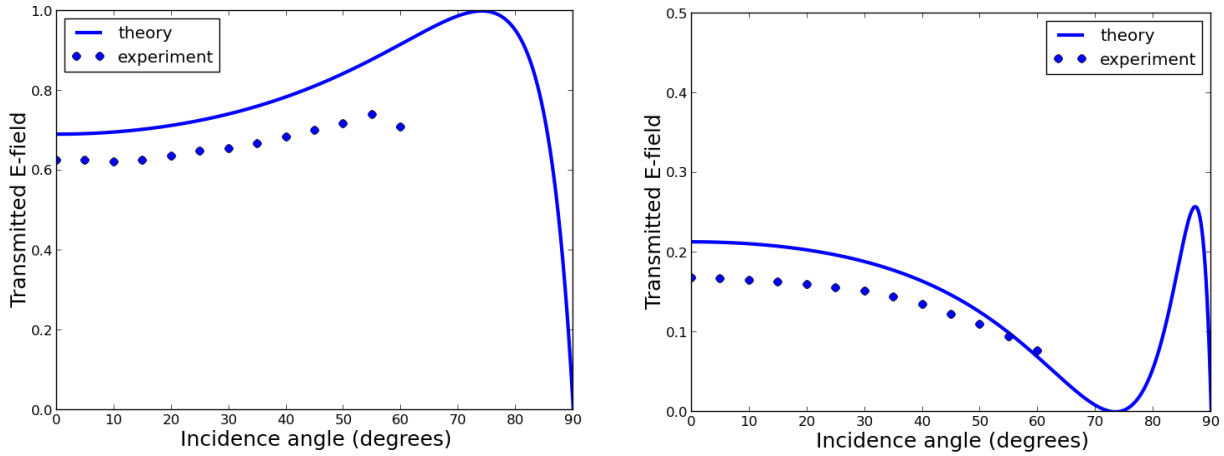

(a) (b)

Figure 2.19: (a) The transmitted E-field after the first pass $E_{1\|}$ versus angle of the incidence, and (b) the transmitted E-field after the second pass $E'_{1\|}$ versus angle of the incidence. In both figures the solid line represents the theoretical result plotted using Eqs. 2.6.27 and 2.6.37, and the points represent the experimental result obtained from the numerical integration of the THz pulses spectrum as described below.

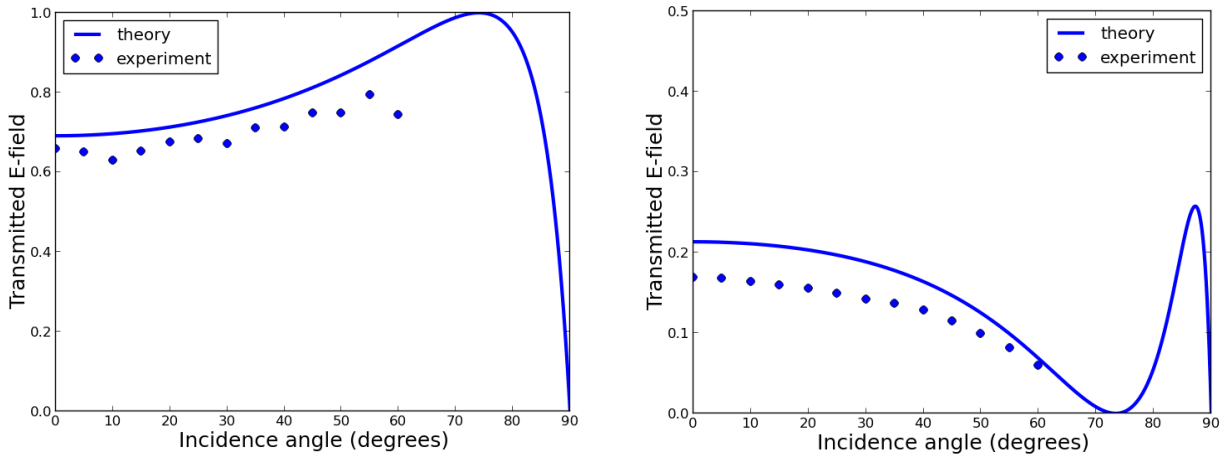

(a) (b)

Figure 2.20: (a) The transmitted E-field after the first pass $E_{1\|}$ versus angle of the incidence, and (b) the transmitted E-field after the second pass $E'_{1\|}$ versus angle of the incidence. In both figures the solid line represents the theoretical result plotted using Eqs. 2.6.27 and 2.6.37, and the points represent the experimental result obtained by calculating the ratio between the initial amplitude (E_{ref}) of the THz pulse before passing through the sample and the maximum value of the amplitude (E_{sam}) of the THz pulse after passing through the Silicon sample.

We measure how the transmitted electric field changes when passing through a Silicon sample if we vary the angle of incidence. We compare the experimental values for $E_{1\|}$ and $E'_{1\|}$ with the theoretical values, as generated via Eqs. 2.6.27 and 2.6.37. We selected the first peak of the pulse, as measured in the time domain, (as shown in Figure 2.18), then we take Fourier transform to transform the data from the time domain to the frequency domain, in order to find the spectrum of the pulse. Then we integrate the area under the resulting curve numerically by using

the trapezoidal rule. We repeat this procedure for every angle of incidence from 0° up to 60°, the results are represented in the data of Figure 2.19(a). We repeated this processes for the second peak, as in Figure 2.18, and the results are represented in the data, which is shown in Figure 2.19(b).

In Figure 2.20 we compare the experimental values for $E_{1\parallel}$ and $E'_{1\parallel}$ with the theoretical values, as generated via Eqs. 2.6.27 and 2.6.37. We selected the value of the initial amplitude (E_{ref}) of the THz pulse before passing through the sample, and the maximum value of the amplitude of the first peak (E_{sam}) of the THz pulse after passing through the Silicon sample, (as shown in Figure 2.18). We calculate the transmitted value, which is given by the ratio between (E_{sam}) and (E_{ref}). We repeat this procedure for every angle of incidence from 0° up to 60°, the results are represented in the data of Figure 2.20(a). We repeated this processes for the second peak, as in Figure 2.18, and the results are represented in the data, which is shown in Figure 2.20(b).

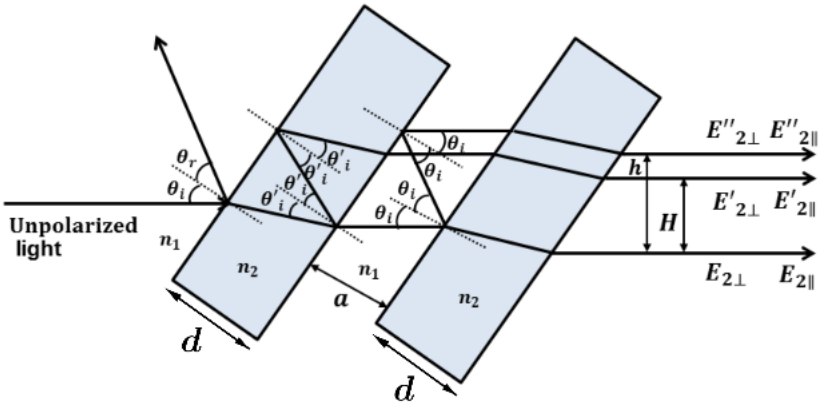

Figure 2.21: Transmitted and reflected components of incident unpolarized light between two samples separated by distance a [12].

The expressions for the $E'_{2\perp}$ and $E'_{2\parallel}$ as shown in Figure 2.21, can be written as

$$E'_{2\perp} = E_{0\perp}(t_{12\perp} \times t_{21\perp} \times r_{\perp}^2 \times t_{12\perp} \times t_{21\perp}), \tag{2.6.38}$$

and

$$E'_{2\parallel} = E_{0\parallel}(t_{12\parallel} \times t_{21\parallel} \times r_{\parallel}^2 \times t_{12\parallel} \times t_{21\parallel}). \tag{2.6.39}$$

Now by substituting Eqs. 2.6.32, 2.6.33, 2.6.24 and 2.6.25 into Eqs. 2.6.38 and 2.6.39, we have

$$E'_{2\perp} = E_{0\perp}\left[\frac{2n_1\cos\theta_i}{n_1\cos\theta_i + n_2\cos\theta_t}\right]^2\left[\frac{2n_2\cos\theta'_i}{n_1\cos\theta_i + n_2\cos\theta'_i}\right]^2\left[\frac{\sin(\theta_i - \theta'_i)}{\sin(\theta_i + \theta'_i)}\right]^2, \tag{2.6.40}$$

and

$$E'_{2\parallel} = E_{0\parallel}\left[\frac{2n_1\cos\theta_i}{n_2\cos\theta_i + n_1\cos\theta_t}\right]^2\left[\frac{2n_2\cos\theta'_i}{n_2\cos\theta_i + n_1\cos\theta'_i}\right]^2\left[\frac{\tan(\theta_i - \theta_t)}{\tan(\theta_i + \theta_t)}\right]^2. \tag{2.6.41}$$

The distance between the initial transmitted light through the second sample and that transmitted after reflection through the first sample, as shown in Figure 2.21, is given by

$$H = d\left[\frac{\sin(2\theta_i')}{\cos(\theta_i')}\right]. \tag{2.6.42}$$

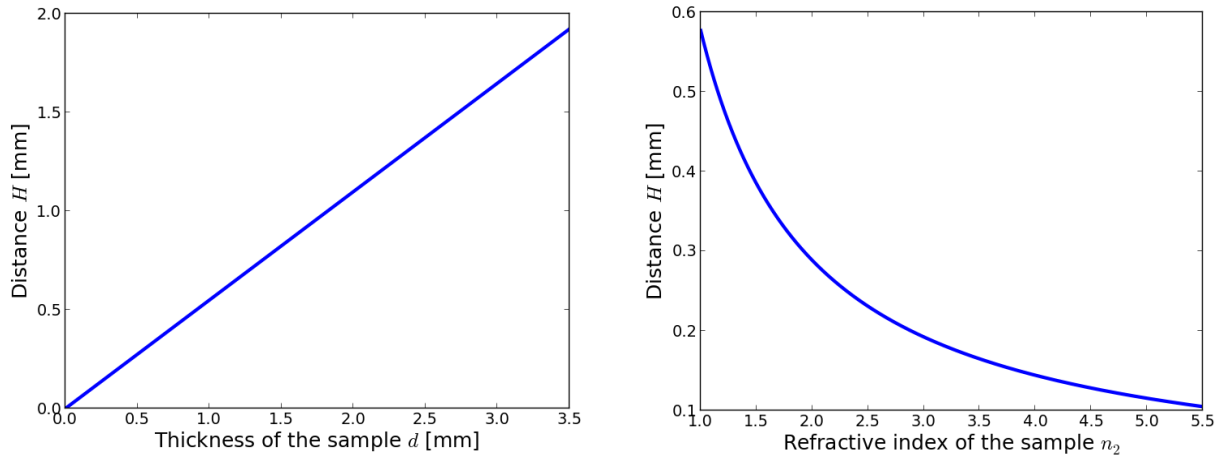

(a) (b)

Figure 2.22: (a) The distance between the initial transmitted light through the second sample and that transmitted after reflection through the first sample versus sample thickness (d) for a fixed refractive index, i.e., $n_2 = 3.5$, (b) the distance between the initial transmitted light through the second sample and that transmitted after reflection through the first sample versus refractive index of the sample (n_2) for fixed sample thickness, i.e., $d = 0.3$ mm.

Figure 2.22(a) shows the variation of the distance between the initial transmitted light through the second sample and that transmitted after reflection through the first sample (H) with respect to sample thickness (d). H is calculated from Eq. 2.6.42 for a fixed refractive index, i.e., $n_2 = 3.5$. Next we vary the refractive index and determine the distance between the initial transmitted light through the second sample and that transmitted after reflection through the first sample at fixed sample thickness, i.e., $d = 0.3$ mm. The results are shown in Figure 2.22(b).

From Figure 2.21, we observe that part of the light transmitted through the first sample is reflected back to the first sample and the rest is transmitted through the second sample. The light reflected to the first sample is again reflected back the second sample. The distance between the initial transmitted light through the second sample and that transmitted after reflection from the first sample is given by Eq. 2.6.43.

$$h = a\left[\frac{\sin(2\theta_i)}{\cos(\theta_i)}\right]. \tag{2.6.43}$$

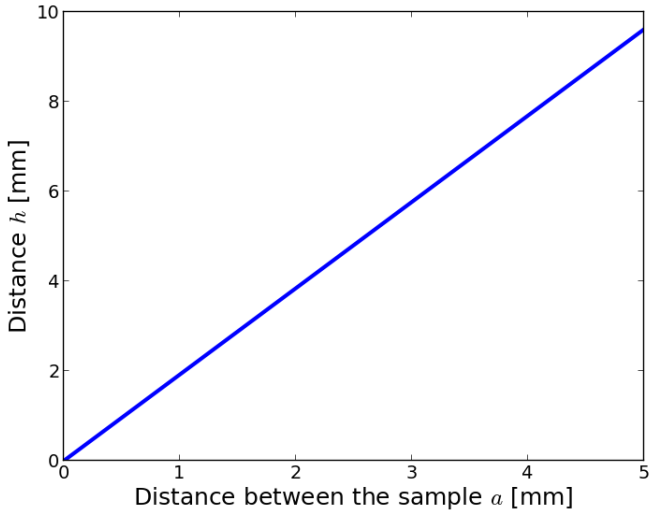

Figure 2.23: Variation of h and the distance between two sample a.

Figure 2.23 shows the variation of h with the distance between two sample (a) at fixed refractive index, i.e., ($n_2 = 3.5$).

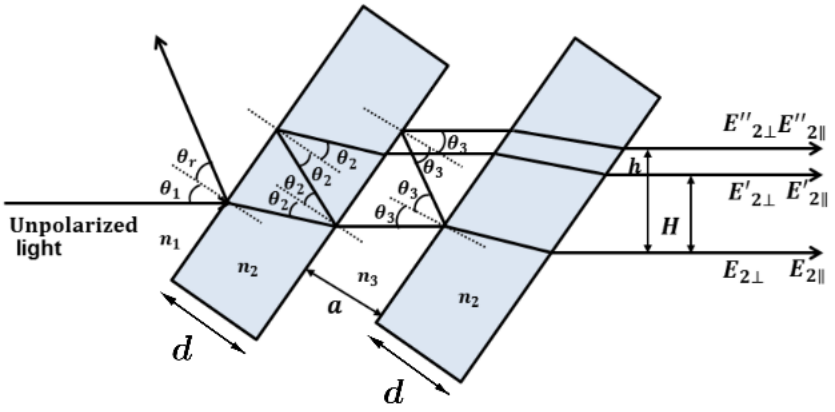

Figure 2.24: Transmitted and reflected components of incident unpolarized light between two samples separated by different mediums with different refractive index (n_3) [12].

If the refractive index of the medium between the two samples is not air, then the expressions for the $E_{2\perp}$ and $E_{2\parallel}$, as shown in Figure 2.24, are given by

$$E_{2\perp} = E_{0\perp}\left[t_{12\perp} \times t_{21\perp} \times t_{23\perp} \times t_{32\perp}\right], \tag{2.6.44}$$

and

$$E_{2\parallel} = E_{0\parallel}\left[t_{12\parallel} \times t_{21\parallel} \times t_{23\parallel} \times t_{32\parallel}\right], \tag{2.6.45}$$

the expressions for the $E'_{2\perp}$ and $E'_{2\parallel}$, as shown in Figure 2.24, can be written as

$$E'_{2\perp} = E_{0\perp}\left[t_{12\perp} \times t_{21\perp} \times t_{23\perp} \times t_{32\perp} \times r_{23\perp} \times r_{21\perp}\right], \tag{2.6.46}$$

and

$$E'_{2\parallel} = E_{0\parallel}\left[t_{12\parallel} \times t_{21\parallel} \times t_{23\parallel} \times t_{32\parallel} \times r_{23\parallel} \times r_{21\parallel}\right], \tag{2.6.47}$$

and the expressions for the $E''_{2\perp}$ and $E''_{2\parallel}$, as in Figure 2.24, can be written as

$$E''_{2\perp} = E_{0\perp}\left[t_{12\perp} \times t_{21\perp} \times t_{23\perp} \times t_{32\perp} \times r_{32\perp} \times r_{32\perp}\right], \tag{2.6.48}$$

and

$$E''_{2\parallel} = E_{0\parallel}\left[t_{12\parallel} \times t_{21\parallel} \times t_{23\parallel} \times t_{32\parallel} \times r_{32\parallel} \times r_{32\parallel}\right]. \tag{2.6.49}$$

From Snell's Law we can calculate the corresponding angles of incidence θ_1, and reflection (θ_2 and θ_3), as [12]

$$\theta_1 = \arcsin\left(\frac{n_2}{n_1}\sin\theta_2\right), \theta_2 = \arcsin\left(\frac{n_1}{n_2}\sin\theta_1\right), \quad \text{and } \theta_3 = \arcsin\left(\frac{n_2}{n_3}\sin\theta_2\right).$$

From Fresnel's equations we can derive expressions for the transmission t and reflection r as [12]

$$t_{12\perp} = \left[\frac{2n_1\cos\theta_1}{n_1\cos\theta_1 + n_2\cos\theta_2}\right], \text{ and } t_{21\perp} = \left[\frac{2n_2\cos\theta_2}{n_1\cos\theta_1 + n_2\cos\theta_2}\right], \tag{2.6.50}$$

and

$$t_{23\perp} = \left[\frac{2n_2\cos\theta_2}{n_2\cos\theta_2 + n_3\cos\theta_3}\right]^2, \text{ and } t_{32\perp} = \left[\frac{2n_3\cos\theta_3}{n_2\cos\theta_2 + n_3\cos\theta_3}\right], \tag{2.6.51}$$

$$r_{21\perp} = \left[\frac{\sin(\theta_2 - \theta_1)}{\sin(\theta_2 + \theta_1)}\right], \quad \text{and } r_{23\perp} = \left[\frac{\sin(\theta_2 - \theta_3)}{\sin(\theta_2 + \theta_3)}\right], \tag{2.6.52}$$

and

$$r_{32\perp} = \left[\frac{\sin(\theta_3 - \theta_2)}{\sin(\theta_3 + \theta_2)}\right] = -r_{23\perp}. \tag{2.6.53}$$

Now by substituting Eq. 2.6.50 and Eq. 2.6.51 into Eq. 2.6.44, we have

$$E_{2\perp} = E_{0\perp}\left[\frac{2n_1\cos\theta_1}{n_1\cos\theta_1 + n_2\cos\theta_2}\right]\left[\frac{2n_2\cos\theta_2}{n_1\cos\theta_1 + n_2\cos\theta_2}\right]\left[\frac{2n_2\cos\theta_2}{n_2\cos\theta_2 + n_3\cos\theta_3}\right]\left[\frac{2n_3\cos\theta_3}{n_2\cos\theta_2 + n_3\cos\theta_3}\right], \tag{2.6.54}$$

by substituting Eqs. 2.6.50, 2.6.51 and 2.6.52 into Eq. 2.6.46, we have

$$E'_{2\perp} = E_{0\perp}\left[\frac{2n_1\cos\theta_1}{n_1\cos\theta_1 + n_2\cos\theta_2}\right]\left[\frac{2n_2\cos\theta_2}{n_1\cos\theta_1 + n_2\cos\theta_2}\right]\left[\frac{2n_2\cos\theta_2}{n_2\cos\theta_2 + n_3\cos\theta_3}\right]\left[\frac{2n_3\cos\theta_3}{n_2\cos\theta_2 + n_3\cos\theta_3}\right]\left[\frac{\sin(\theta_2 - \theta_1)}{\sin(\theta_2 + \theta_1)}\right]\left[\frac{\sin(\theta_2 - \theta_3)}{\sin(\theta_2 + \theta_3)}\right], \tag{2.6.55}$$

and by substituting Eqs. 2.6.50, 2.6.51 and 2.6.53 into Eq. 2.6.48, we have

$$E''_{2\perp} = E_{0\perp}\left[\frac{2n_1\cos\theta_1}{n_1\cos\theta_1 + n_2\cos\theta_2}\right]\left[\frac{2n_2\cos\theta_2}{n_1\cos\theta_1 + n_2\cos\theta_2}\right]\left[\frac{2n_2\cos\theta_2}{n_2\cos\theta_2 + n_3\cos\theta_3}\right]\left[\frac{2n_3\cos\theta_3}{n_2\cos\theta_2 + n_3\cos\theta_3}\right]\left[\frac{\sin(\theta_3-\theta_2)}{\sin(\theta_3+\theta_2)}\right]. \quad (2.6.56)$$

The distance between the initial transmitted light through the second sample and that transmitted light after reflection through the first sample, as shown in Figure 2.24, is given by

$$H = d\left[\frac{\sin(2\theta_2)}{\cos(\theta_2)}\right]. \quad (2.6.57)$$

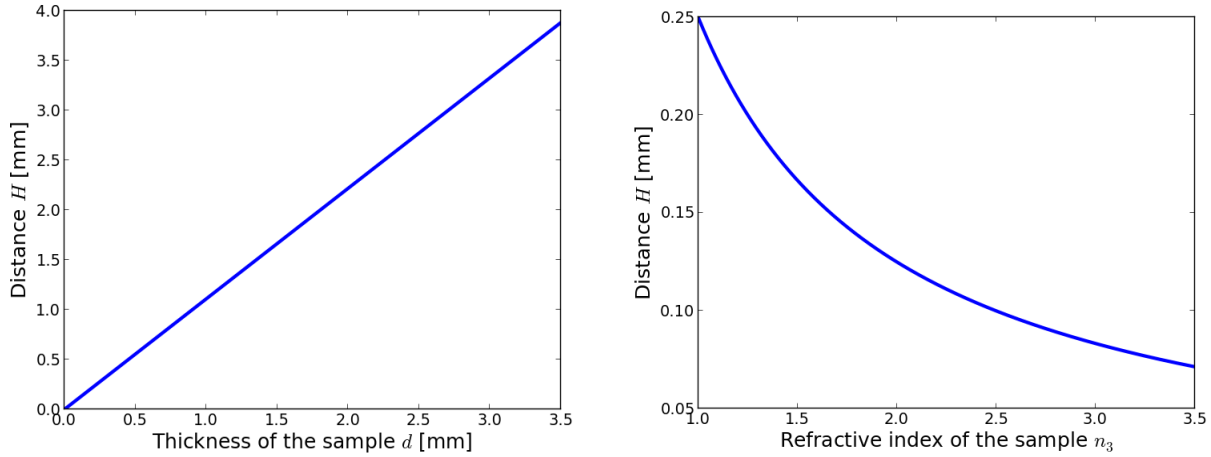

(a) (b)

Figure 2.25: (a) The distance between the initial transmitted light through the second sample and that transmitted after reflection through the first sample versus sample thickness (d) for a fixed refractive index, i.e., $n_3 = 1.5$, (b) the distance between the initial transmitted light through the second sample and that transmitted after reflection through the first sample versus refractive index of the sample (n_3) for fixed sample thickness, i.e., $d = 0.15$ mm.

Figure 2.25(a) shows the variation of the distance between the initial transmitted light through the second sample and that transmitted after reflection through the first sample (H) with respect to sample thickness (d). H is calculated from Eq. 2.6.57 for a fixed refractive index, i.e., $n_3 = 1.5$. Next we vary the refractive index and determine the distance between the initial transmitted light through the second sample and that transmitted after reflection through the first sample at fixed sample thickness, i.e., $d = 0.15$ mm. The results are shown in Figure 2.25(b).

From Figure 2.24, we observe that part of the light transmitted through the first sample is reflected back to the first sample and the rest is transmitted through the second sample. The light reflected to the first sample is again reflected back to the second sample. The distance between the initial transmitted light through the second sample and that transmitted after reflection from the first sample is given by Eq. 2.6.58.

$$h = a\left[\frac{\sin(2\theta_3)}{\cos(\theta_3)}\right]. \quad (2.6.58)$$

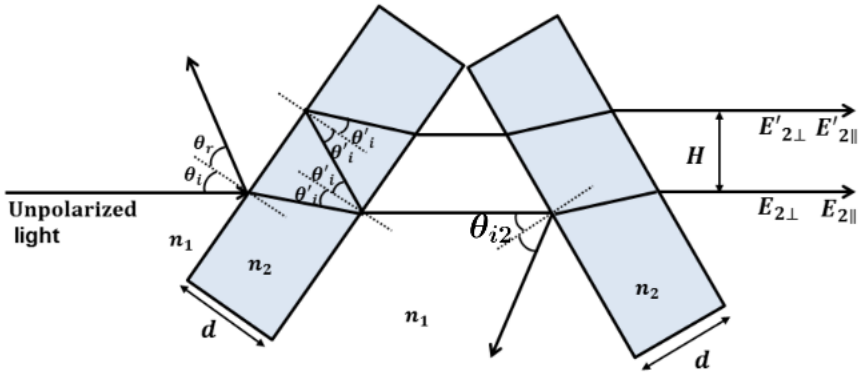

Figure 2.26: Transmitted and reflected components of incident unpolarized light between two samples situated at specific position. Mention that samples are positioned in such a way that $\theta_{i2} = \theta_i$ and that these angles of incidence can be chosen to be the Brewster angle.

Now by changing the position of the second sample, as shown in Figure 2.26, the expression for the $E_{2\perp}$, is given by

$$E_{2\perp} = E_{0\perp}\left[t_{12\perp} \times t_{21\perp} \times t_{12\perp} \times t_{21\perp}\right], \tag{2.6.59}$$

the value of $E_{2\perp}$ is equal to 6.05×10^{-3}, at the Brewster's angle. With $E_{0\perp}$ set to 1.

The expression for the $E'_{2\perp}$, as shown in Figure 2.26, can be written as

$$E'_{2\perp} = E_{0\perp}\left[t_{12\perp} \times t_{21\perp} \times t_{12\perp} \times t_{21\perp} \times r_{\perp}^{2}\right], \tag{2.6.60}$$

the value of $E'_{2\perp}$ is equal to 4.35×10^{-3}, at the Brewster's angle. With $E_{0\perp}$ set to 1.

The distance between the initial transmitted light through the second sample and that transmitted after reflection through the first sample, as shown in Figure 2.26, is given by

$$H = d\left[\frac{\sin(2\theta'_i)}{\cos(\theta'_i)}\right], \tag{2.6.61}$$

by using Snell's law we are able to derive the expression for the θ'_i as [12]

$$\theta'_i = \arcsin(\frac{n_1}{n_2}\sin\theta_i), \tag{2.6.62}$$

substituting Eq. 2.6.62 into Eq. 2.6.61, we have

$$H = d\left[\frac{\sin(2(\arcsin(n_1/n_2\sin\theta_i)))}{\cos(\arcsin(n_1/n_2\sin\theta_i))}\right]. \tag{2.6.63}$$

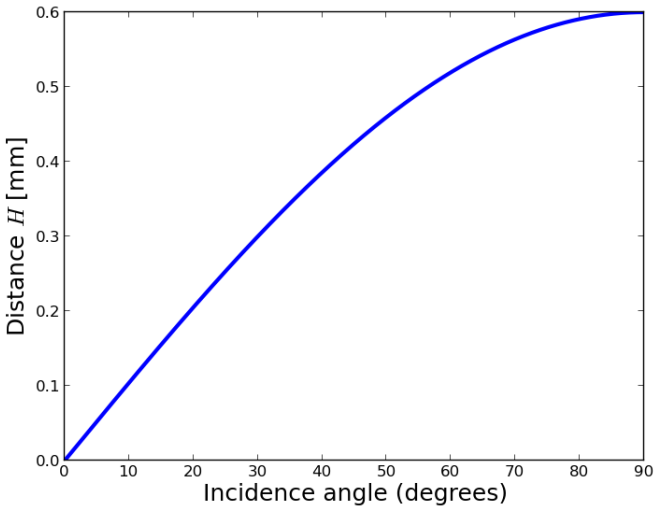

Figure 2.27: The distance between the initial transmitted light through the second sample and that transmitted after reflection through the first sample versus angle of the incidence (θ_i) for a fixed refractive index, i.e., $n_2 = 3.5$, and for a fixed sample thickness, i.e., $d = 0.3$ mm.

Figure 2.27 shows the variation of the distance between the initial transmitted light through the second sample and that of the light transmitted after reflection through the first sample (H) with respect to the angle of the incidence (θ_i). H is calculated from Eq. 2.6.63 for a fixed refractive index, i.e., $n_2 = 3.5$, and for fixed sample thickness, i.e., $d = 0.3$ mm. The result is shown in Figure 2.27.

In summary, the results obtained in the previous calculations showed that if we placed a sample (with parallel interfaces) at the Brewster's angle, the parallel polarization component of the incident light will be 100 % transmitted together with a small amount of the perpendicular polarized light. This small amount can be determined from the ratio between the two polarizations of the light after passing through the sample $\left(E_{1\perp}/E_{1\parallel} = 7.78 \times 10^{-2}\right)$. The extinction ratio $(I_{1\perp}/I_{1\parallel})$ can hence be determined in a similar fashion $\left(\left(E_{1\perp}/E_{1\parallel}\right)^2 = 6.05 \times 10^{-3}\right)$. In the case where there are two samples placed mirroring each other, it was found that $\left(E_{2\perp}/E_{2\parallel} = 6.05 \times 10^{-3}\right)$ and the extinction ratio was $\left(3.66 \times 10^{-5}\right)$. This shows that by placing two samples at mirrored Brewster's angles, the incident pulse can be polarized without introducing a lateral offset.

2.7 Multiple reflections

In this section we wish to discuss the interaction of the THz pulse with the sample of thickness d. If the THz pulse propagates from a medium with refractive index n_1 into the sample of refractive index n_2 as shown in Figure 2.29. Then the multiple reflection will occur at the sample interfaces, and the refractive index can be measured by the reflection [46].

The THz pulse can be detected as illustrated in Figure 2.28.

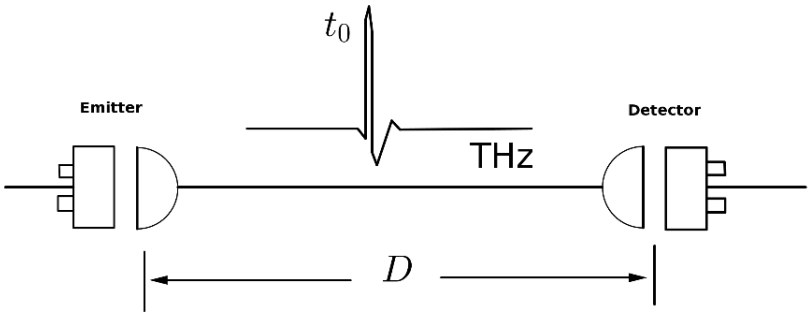

Figure 2.28: THz pulse generation.

The time the THz pulse takes to travel from the emitter to the detector can be expressed as follows:

$$t_0 = \frac{D}{c}, \tag{2.7.1}$$

where D is the total distance between the emitter and the detector, and c is speed of THz pulse in free space. Let us consider a sample of thickness d placed between the emitter and the detector as shown in Figure 2.29. Assume that THz radiation enters the sample at $\theta_i = 0°$.

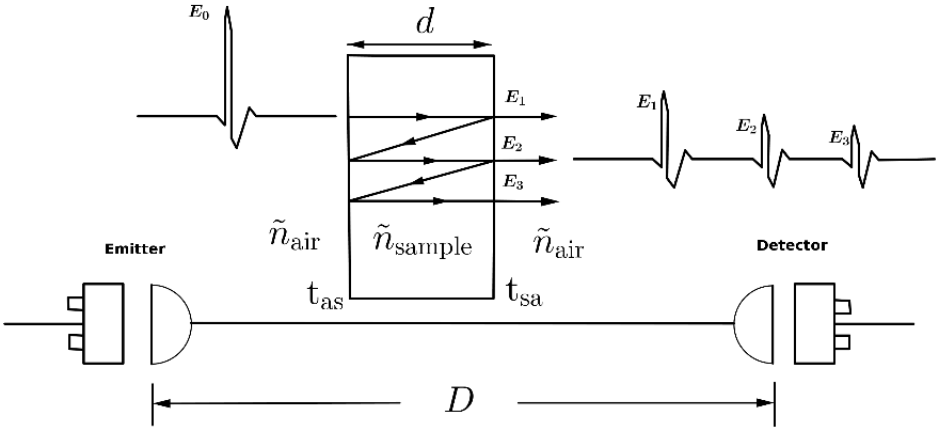

Figure 2.29: Multiple reflections at the sample interfaces.

In general, the refractive index of the sample can be written as [10]

$$n = \frac{c}{v}. \tag{2.7.2}$$

According to the multiple reflection concept as shown in Figure 2.29, and there are three distinct peaks, labelled (1), (2), and (3). For peak 1, we can write the time t_1 the THz pulse takes to travel from the emitter to the detector passing through the sample as

$$t_1 = \frac{D-d}{c} + \frac{n\,d}{c}. \tag{2.7.3}$$

For peak 2, Eq. 2.7.3 becomes

$$t_2 = \frac{D-d}{c} + \frac{3n\,d}{c}. \tag{2.7.4}$$

For peak 3, Eq. 2.7.3 can be expressed as

$$t_3 = \frac{D-d}{c} + \frac{5n\,d}{c}. \tag{2.7.5}$$

Where d is the physical length of the sample, and v is the speed of the THz pulse through the sample.

Hence, by measuring the arrival time t_0, t_1, t_2 and t_3, the refractive index can be calculated.

Chapter 3

Fourier analysis

3.1 Fourier series

This chapter deals with the importance of Fourier series analysis as well as the concepts of the fast Fourier transform. Methods based on the Fourier analysis are essential in analysing many different types of waves such as signal processing and communication, quantum particle waves, among others. Fourier series is named after Joseph Fourier, due to his work on heat flow and the development of cohesive theory of such series [50].

Fourier series deals with analysing the periodic phenomena, while the nonperiodic phenomena are analysed using Fourier transform. The spectrum of the signals can be obtained when the discrete set of frequencies in the periodic phenomena become a continuum of frequencies in the nonperiodic phenomena [51].

Most studied phenomena were modelled by the fundamental differential equations of physics (wave equations, heat equations) and their solutions are often constrained by boundary conditions. So then, the idea of using Fourier series is to find the explicit solutions [51].

Fourier showed that any general periodic function with a period of $2L$ or 2π can be represented as infinite series as seen in Eq. 3.1.1[50].

$$f(x) = \frac{1}{2}a_0 + \sum_{n=1}^{\infty}(a_n \cos\frac{n\pi x}{L} + b_n \sin\frac{n\pi x}{L}), \tag{3.1.1}$$

where a_0, a_n, and b_n are known as the Fourier coefficients.

3.2 Fourier transform

Fourier transform is the mathematical tool widely used for transforming both functions (single or multidimensional) and data sequences from time domain to the frequency domain, and the converse can be obtained by applying the inverse Fourier transform. In addition, Fourier transform is used to obtain the frequency as well as the amplitude information for nonperiodic functions. The results obtained from the functions on which Fourier transform are applied are known as the power spectrum or the frequency spectrum [39].

The general form of the integral for Fourier transformation can be written as [50]

$$f(t) = \frac{1}{2\pi} \int_{-\infty}^{\infty} e^{i\omega t} d\omega \int_{-\infty}^{\infty} f(u) e^{-i\omega u} du. \tag{3.2.1}$$

and

$$\mathcal{F}\left[f(t)\right] = \int_{-\infty}^{\infty} f(t) e^{-i\omega t} dt = F(\omega). \tag{3.2.2}$$

The expression $F\left[f(t)\right]$ is known as the Fourier transform of the $f(t)$, which transforms it from time domain into frequency domain. The inverse Fourier transform can be written as

$$\mathcal{F}^{-1}\left[F(\omega)\right] = \frac{1}{2\pi} \int_{-\infty}^{\infty} F(\omega) e^{i\omega t} dt.$$

3.2.1 The properties of the Fourier transform

In this section we will briefly summarize some properties of the Fourier transform, which make it a useful tool in practice. Most of this properties are proved from the definition of the Fourier transform and its inverse [39, 50, 15].

- Symmetry property of the Fourier transform: e.g. Let $\mathcal{F}[f(t)] = F(\omega)$, then $\mathcal{F}[f(t)] = 2\pi f(-\omega)$.
- Linearity property of the Fourier transform: e.g. $\mathcal{F}[nf(t) + mg(t)] = n\mathcal{F}[f(t)] + m\mathcal{F}[f(t)]$, where n and m are any constants.
- Time and frequency shifting properties of the Fourier transform: e.g. $\mathcal{F}[f(t - t_0)] = e^{-i\omega t_0} F(\omega)$, and $\mathcal{F}[f(\omega - \omega_0)] = e^{-i\omega_0 t} f(t)$,

  where t_0 and ω_0 are constants.

The main tool we used in our work is the fast Fourier transform (FFT), which is an algorithm that can be used in order to speed up the discrete Fourier transform (DFT) calculation by reducing the multiplication numbers and additions required [11]. Using the FFT algorithm the data to be transferred could either be in time or frequency and can be put in a file or an array. The transform compiles very quickly and the new array will contain the transformed function, which can be achieved by various software programmes [15].

Chapter 4

Generation and detection of THz radiation

4.1 Theory of the oscillation in a series RLC circuit

In this chapter we wish to give a brief explanation of the theory behind the oscillation in a series RLC circuit, and we will discuss the possible different cases of current flow in a RLC circuit. This enable us to understand the theory behind the generation of THz radiation.

To investigate the oscillation of the current flow in a RLC circuit, let's assume that we have a second-order circuit, whose resistance R, inductance L, and capacitance C are connected in series as shown in Figure 4.1. Initially the inductor in the circuit has no initial current and the capacitor is charged with a voltage V_0. The current can start flowing in the circuit due to the initial energy stored in the capacitor when the circuit is closed ($t = 0$). The different types of oscillations in the circuit can be characterized by solving the differential equation which describes the circuit [23].

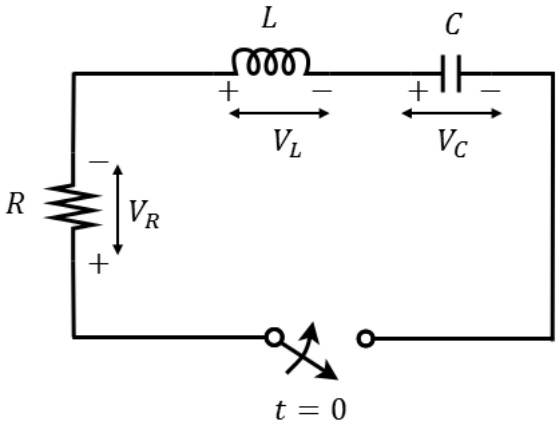

Figure 4.1: Schematic diagram for a typical RLC circuit.

The differential equation that describes the series RLC circuit can be written as

$$L\frac{dI(t)}{dt} + RI(t) + \frac{1}{C}\int I(t)dt = 0. \tag{4.1.1}$$

Now by differentiating Eq. 4.1.1, we have

$$\frac{d^2I(t)}{dt^2} + \frac{R}{L}\frac{dI(t)}{dt} + \frac{1}{LC}I(t) = 0, \tag{4.1.2}$$

and we can see that Eq. 4.1.2 is a homogeneous differential equation, which has a solution of the form

$$I(t) = k\exp(nt), \tag{4.1.3}$$

where k and n are constants that can be determined. Substituting Eq. 4.1.3 into Eq. 4.1.2 , we have

$$n^2 + (R/L)\,n + (1/LC) = 0, \tag{4.1.4}$$

which is the characteristic equation of the RLC circuit, with two roots n_1 and n_2 given as

$$n_1 = -\frac{R}{2L} + \sqrt{\frac{R^2}{4L^2} - \frac{1}{LC}}, \tag{4.1.5}$$

and

$$n_2 = -\frac{R}{2L} - \sqrt{\frac{R^2}{4L^2} - \frac{1}{LC}}. \tag{4.1.6}$$

The values of the square roots can be either positive, negative, or zero, which we shall discuss subsequently.

- Case I: if $\frac{R^2}{4L^2} = \frac{1}{LC}$ (critically damped), therefore $n_1 = n_2 = -\frac{R}{2L}$. In this case, the form of $I(t)$ in Eq. 4.1.3 become as

$$I(t) = (k_1 t + k_2)\exp[-(R/2L)\,t]. \tag{4.1.7}$$

After calculating the initial conditions (at $t = 0$), with doing some mathematical calculation, we can write

$$I(t) = -(V_0/L)t\exp[-(R/2L)\,t]. \tag{4.1.8}$$

Now the formula of the voltage across the capacitor V_C can be obtained by using the following equation

$$V_C(t) = (1/C)\int_0^t I(u)\,du + V_0. \tag{4.1.9}$$

By substituting Eq. 4.1.8 into Eq. 4.1.9 and integrating the result, we can write

$$V_C(t) = V_0\,[1 + (R/2L)t]\exp[-(R/2L)\,t]. \tag{4.1.10}$$

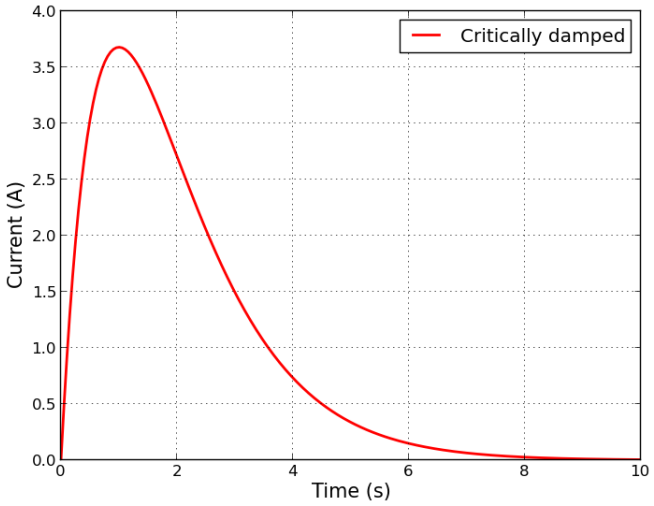

Figure 4.2: Example of the current versus time for the case of a critically damped RLC circuit.

Figure 4.2 shows the current in a critically damped series RLC circuit. At time ($t = 0$) there is no current flow in the circuit ($I(0) = 0$), which implies that the value of the voltage across the resister is zero. According to the Kirchoff's Voltage Laws "KVL", the magnitude of the voltage across the inductor is ($V_L = V_0$), which lead to the current flow in the inductor. As the current flows through an inductor, some part of the energy is stored in the magnetic field of the inductor and the other part of the energy will be dissipated as heat in the resistor. $\frac{dI}{dt}$ through the inductor will decrease due to the presence of the voltage across the resistor, which make the current flow slowly through the inductor, and as a result the current $I(t)$ starts to rises until it reaches a maximum value, before decreasing to zero [23].

- Case II: if $(\frac{R^2}{4L^2}) > (\frac{1}{LC})$ (overdamped), n_1 and n_2 are real but different from each other ($n_1 \neq n_2$). In this case $I(t)$ in Eq. 4.1.3 become as

$$I(t) = k_1 \exp(n_1 t) + k_2 \exp(n_2 t). \tag{4.1.11}$$

Again by applying the initial conditions and doing some mathematical calculation, we can write

$$I(t) = \frac{V_0}{L(n_1 - n_2)}(\exp(n_2 t) - \exp(n_1 t)). \tag{4.1.12}$$

By substituting Eq. 4.1.9 into Eq. 4.1.12, we can write the voltage across the capacitor as

$$V(t) = \frac{V_0}{(n_1 - n_2)}(n_1 \exp(n_2 t) - n_2 \exp(n_1 t)). \tag{4.1.13}$$

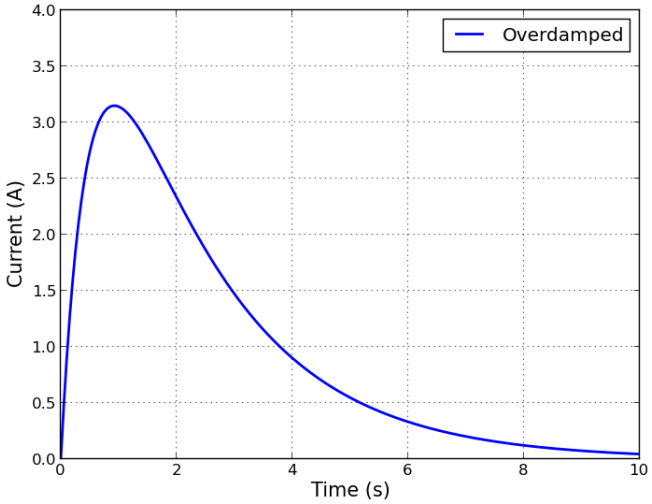

Figure 4.3: Example of the current versus time for the case of an overdamped RLC circuit.

Figure 4.3 shows the current for the case of an overdamped series RLC circuit, which is some what similar to the previous case (critically damped), except that the loss of the energy through the resistor, in the case of overdamped occurs faster than in the case of critical damped circuits [23].

- Case III: if $(\frac{R^2}{4L^2}) < (\frac{1}{LC})$ (underdamped), n_1 and n_2 are complex conjugates and $(n_1 \neq n_2)$ in this case $I(t)$ in Eq. 4.1.3 become

$$I(t) = k_1 \exp(n_1 t) + k_2 \exp(n_2 t), \tag{4.1.14}$$

and we can write n_1 and n_2 for the complex case as

$$n_1 = -\frac{R}{2L} + i\sqrt{\frac{1}{LC} - \frac{R^2}{4L^2}}, \tag{4.1.15}$$

and

$$n_2 = -\frac{R}{2L} - i\sqrt{\frac{1}{LC} - \frac{R^2}{4L^2}}. \tag{4.1.16}$$

By doing some mathematical calculations we can write

$$I(t) = -\frac{V_0}{(bL)} \exp(-at) \sin(bt), \tag{4.1.17}$$

where a and b are equal to $(R/2L)$ and $\sqrt{1/LC - R^2/4L^2}$ respectively.

By substituting Eq. 4.1.9 into Eq. 4.1.17, we can write the voltage across the capacitor as

$$V_C(t) = (\frac{V_0}{b\sqrt{LC}}) \exp(-at) \cos\left[bt - \arctan(a/b)\right]. \tag{4.1.18}$$

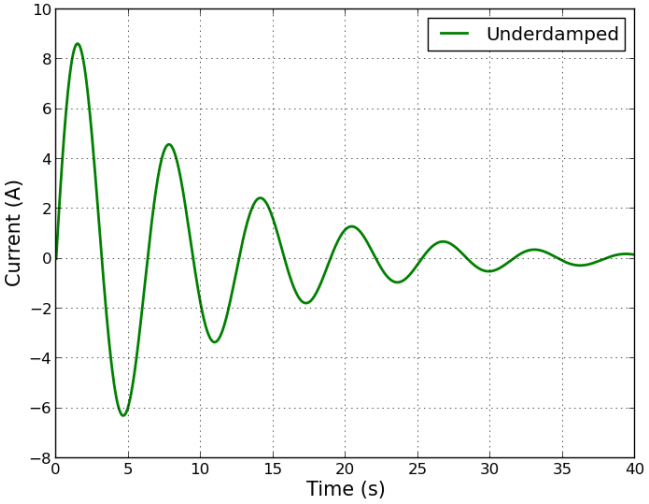

Figure 4.4: Example of the current versus time for the case of an underdamped RLC circuit.

Figure 4.4 shows the current in an underdamped series RLC circuit, where the value of the resistor is $R < 2\sqrt{L/C}$, which leads to a slower rate energy dissipation. Therefore, there is sufficient energy which allows the exchange of energy from the magnetic field of the inductor to the electric field of the capacitor for an extended period of time. As the energy in the capacitor increases (due to the increase of the voltage), the energy in the inductor will decrease (due to the decrease of the current). The oscillations seen in the above figure are due to the continuous exchange of energy. The resistor in the circuit determines the rate of energy loss, so that the magnitude of the oscillations decay with time (at the rate of $\exp(-at)$). Eventually, the oscillations will die down, because of the unavailability of energy when the voltage across the capacitor and the current reach zero [23].

4.2 Photoconductive (PC) antenna

A photoconductive (PC) antenna is an electrical circuit consisting of a resistor and a bias voltage that are connected in series with a semiconductor photoconductive switch as shown in Figure 4.5. There is a current in the PC circuit due to the free carriers (free electron and holes) that are generated via light when the photon energy is larger than the band gap of the semiconductor [20].

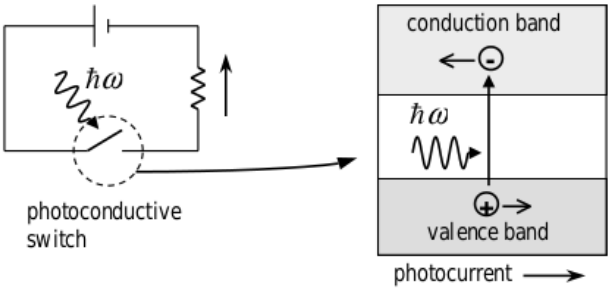

Figure 4.5: Schematic diagram of a photoconductive (PC) switch [20].

Generally, photoconductive antennae are widely used for the generation as well as the detection of a terahertz (THz) pulse [44]. In order to either produce or detect a THz pulse, the switching action in the PC switch must occur on a very short time scale (subpicosecond). The switching-on time depends on the laser pulse duration, while the switching-off time depends on the photoexcited carrier lifetime. In other words, to obtain a switching action on a very short time scale in the PC antenna, a short laser pulse duration as well as a short photoexcited carrier lifetime are required [20].

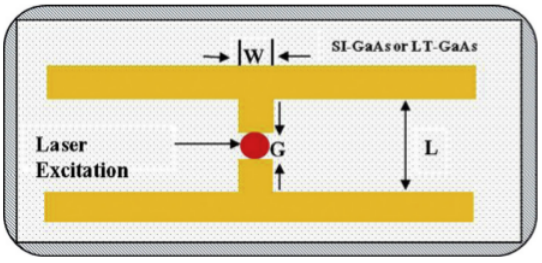

Figure 4.6: Schematic structure of a photoconductive (PC) dipole antenna [45].

A typical structure of a photoconductive (PC) dipole antenna is illustrated in Figure 4.6 [44]. It consists of two metal electrodes (yellow) coated on a semiconductor (grey) and separated with the gap area from each other [54]. The typical magnitudes of the geometrical parameters for the Hertzian dipole-type antenna are $G = 5 - 10\,\mu$m, $L = 30 - 50\,\mu$m, and $W = 10 - 20\,\mu$m, where G is the PC gap area, L is the PC length and W is the PC width, all of which are illustrated in Figure 4.6 [44]. However, the magnitudes of the geometrical parameters for the PC antenna, which are used in our experiment for both generation and detection of the THz pulse are $G = 10\,\mu$m, $L = 40\,\mu$m, and $W = 20\,\mu$m [24].

There are various photoconductive materials used for the PC switches, such as radiation damaged silicon on sapphire (RD-SOS), indium phosphide (InP), low temperature grown gallium arsenide (LT-GaAs) and chromium-doped gallium arsenide (Cr-GaAs). However, the most widely used materials for the generation as well as detection of THz pulses are (LT-GaAs) and (RD-SOS), because of their very short carrier lifetimes (in the subpicosecond range) [20].

4.3 LT-GaAs

Low temperature grown gallium arsenide (LT-GaAs) is widely used for the photoconductuve antennae for both the generation and detection of THz radiation. Furthermore, LT-GaAs is also an important material widely used for many fast optoelctronic devices such as large bandwidth photodetectors and high speed and high voltage photoconductive (PC) antennae [28, 13].

The initial fast response will occur due to removal of electrons from the conduction band in LT-GaAs. However, this does not imply electron and hole recombination. Recently, researchers have developed experiments for measuring the recombination times in the LT-GaAs material [22].

In the next section we will give a brief explanation of the simplified model that describes the dynamics of the the carriers in the LT-GaAs material, which is developed by Hany S.Loka et al [22].

4.3.1 Dynamics rate equations model describe the carriers in LT-GaAs material

The important processes that occur in the band diagram of the LT-GaAs are due to the absorption photon energy, as illustrated in Figure 4.7 [13].

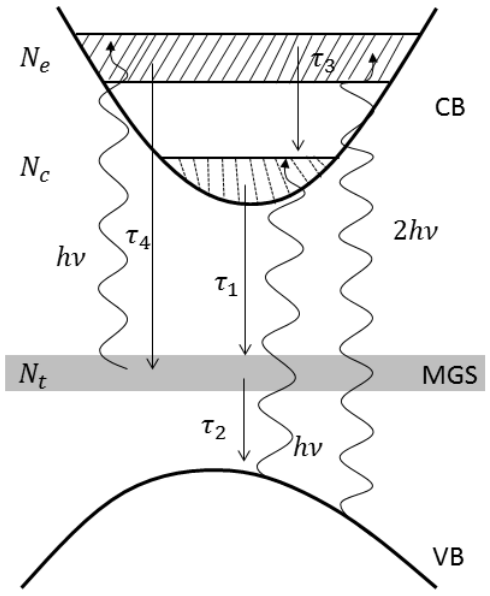

Figure 4.7: Band diagram for LT-GaAs describing various processes in the rate equations model [13, 22].

In general, photons with energy ($h\nu$) that is greater that the band gap (E_g) will be absorbed. Carriers will be excited from the valance band (VB) to the high conduction band (CB). In Figure 4.7, N_e represents the carriers that are generated by either the two photon processes or by the absorbed photons with energy ($h\nu > E_g$), N_c represents the carrier population at the edge of the conduction band, and N_t represents carriers that are trapped in the mid gap states (MGS).

The carriers from N_c can be trapped in MGS with time constant τ_1. Also the carriers from the upper states N_e can be trapped in MGS with time constant τ_4. The carriers trapped in the MGS N_t will decay to the valance band with time constant τ_2. In the mid gap states of this LT-GaAs model, photons are absorbed by the carriers, as seen in Figure 4.7. This is remarkable, because it can produce a substantially larger carrier concentration in the conduction band (CB). The rate equations describing the carriers in the LT-GaAs diagram can be written as [13, 22].

$$\frac{dN_c}{dt} = \frac{I\alpha}{h\nu} - \frac{N_c}{\tau_1} + \frac{N_e}{\tau_3}, \tag{4.3.1}$$

where I is the intensity of the incident light with photon energy $h\nu$, and α is the absorption coefficient of carriers in the valance band (VB).

$$\frac{dN_t}{dt} = -\frac{I\alpha_t}{h\nu} - \frac{N_t}{\tau_2} + \frac{N_c}{\tau_1} + \frac{N_e}{\tau_4}, \tag{4.3.2}$$

where α_t is the absorption coefficient of carriers in the mid gap states (MGS), and

$$\frac{dN_e}{dt} = \frac{I\alpha_t}{h\nu} + \frac{I^2\beta}{2h\nu} - \frac{N_e}{\tau_3} - \frac{N_e}{\tau_4}, \tag{4.3.3}$$

where β is the two-photon absorption coefficient. In all cases the total absorption can be written as

$$\alpha_{\text{total}} = \alpha + \alpha_t + \beta I = \sigma N_0(1 - N_c/N_0) + \sigma_t N_t + \beta I, \tag{4.3.4}$$

where σ is the cross section of band to band transitions, and N_0 is the saturation carrier density [22]. With typical time constants of $\tau_1 = 0.5\,\text{ps}$, $\tau_2 = 10\,\text{ps}$, $\tau_3 = 100\,\text{ps}$, and $\tau_4 = 0.31\,\text{ps}$, and a ultrashort optical pulse of approximately 100 fs FWHM, the excited state dynamics are dominated by τ_1 (if $2h\nu$ absorption is kept negligible) which results in a subpicosecond optical switch [13].

Chapter 5

Terahertz time domain spectroscopy (THz-TDS)

5.1 Introduction

In general the response of solids to monochromatic radiation can be measured over a large frequency range. By performing the experiment in the time domain the optical constants of materials can be obtained over a broad band using suitably short pulses [6, 55].

In most spectroscopic measurements, such as ultraviolet-visible (uv-vis) spectroscopy, the experiments are performed in the frequency and/or wavelength domain [26, 32]. Due to the high frequency of the infrared, visible and ultraviolet light, the experiments are difficult to perform in the time domain [5]. Hence uv-vis spectroscopy only produces amplitude information. However, in THz-TDS the experiments are performed in the time domain [26, 32]. Since THz radiation has low frequencies the direct measurement of the time varying electric field is technologically possible using a short optical laser pulses [5]. Performing experiments in the time domain allows us to measure the time varying electric field of a THz pulse rather than only the intensity [26, 32]. By applying the fast Fourier transform to this time varying electric field, frequency information of the pulse such as amplitude and phase can be obtained.

Since the intensity is proportional to the electric field and its complex conjugate ($I = \frac{1}{2}\sqrt{\varepsilon/\mu}\, EE^*$), there is no phase information contained in the intensity measurement. However, measurements of time varying electric field of the THz pulse contain complete phase information. Much information about the characteristics of the materials could be obtained through time domain spectroscopic experiments [5].

5.2 Experimental setup

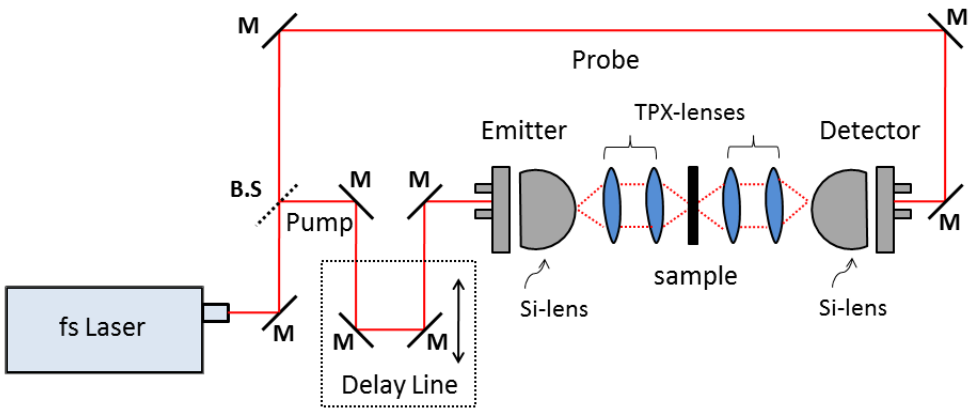

Figure 5.1: Experimental setup for terahertz time domain spectroscopy (THz-TDS). B.S is a beam splitter and M are mirrors.

Our experimental setup for THz-TDS measurements is illustrated in Figure 5.1. The setup is very similar to an optical pump probe experiment [20, 24]. An ultra-short optical pulse from a pulsed fibre laser (780 nm central wavelength, 100 fs pulse duration, 20 mW average power) [24] is split into two pulses by a beam splitter (B.S.). The one pulse (pump pulse) goes to the photoconductive emitter antenna whilst the other pulse (probe pulse) goes to the detector antenna. The interaction of the optical pulse with the emitter generates a short pulse of THz radiation. The THz pulse is collimated by a silicon lens to minimize reflection losses, after which it passes through four polymethylpentene (TPX) lenses before being collected by another silicon lens and focussed onto the detector antenna. The optical pulse that interacts with the detector, gates the detector through the generation of free charge carriers, allowing it to measure the part of the THz pulse (both amplitude and phase) that overlaps temporally with the optical pulse. By changing the delay between the generation pulse and the detection pulse through a mechanical delay line (see Figure 5.1), we are able to map out the electric field of the THz pulse in time.

5.3 Mechanical procedure for THz pulse measurements

When the THz pulse coming from the PC emitter reaches the PC detector at a time coinciding with the gate pulse exciting charge carriers into the conduction band of the detector, a current is generated. We are able to measure this photocurrent induced by the incoming electric field of the THz pulse. The measurement of this induced current is done by integrating the current within the gate area, which provides a single data point in time. Using the delay stage, the gated period of the pulse is moved, again we integrate to obtain another a signal data point and so on. A lock-in amplifier is used to improve the signal to noise ratio. By measuring this current with varying the time delay between the optical gate pulse and the incoming THz pulse, the electric field of the THz pulse can be mapped out in the time domain.

5.3.1 Generation of THz pulses with a photoconductive (PC) antenna

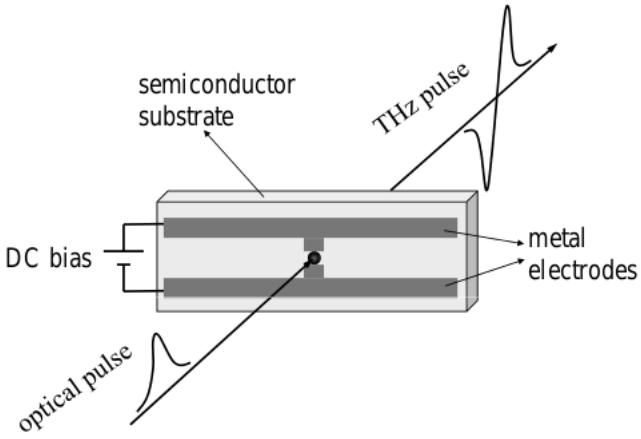

Figure 5.2: Schematic diagram of THz pulse generation with a photoconductive (PC) antenna [20].

In order to generate a THz pulse with a PC antenna, the PC gap area at the centre of the antenna is exited by applying a DC voltage and illuminating it with a femtosecond optical laser pulse as illustrated in Figure 5.2 [44]. When the PC gap is excited, an ultrashort current pulse is generated with accelerated photoexcited carriers under the bias field. There is an ultrashort electromagnetic pulse (THz pulse) generated by the transient photocurrent density $J(t)$ in the PC antenna. The electric field of the THz pulse is proportional to the time derivative of the photocurrent density in the PC antenna, given as [44]

$$E_{\mathrm{THz}} \propto \frac{\partial J(t)}{\partial t}. \tag{5.3.1}$$

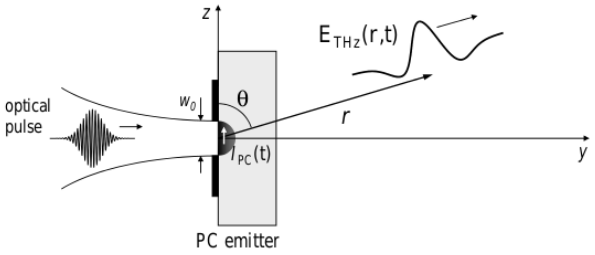

Figure 5.3: Electric field of the THz dipole radiation from a photoconductive (PC) antenna [20].

For simplicity we consider THz dipole radiation in free space, and the expression for the THz dipole radiation in free space can be written as [20]

$$E_{\mathrm{THz}}(r,t) = \frac{\mu_0 \sin\theta}{4\pi r} \frac{d^2}{dt_r^2}[P(t_r)]\hat{\theta}, \tag{5.3.2}$$

where μ_0 is the permeability of free space, $P(t_r)$ is the dipole moment of the source at the related time ($t_r = t - \frac{r}{c}$), and r is the distance from the source, which is referred to as the far-field. The expression for the time derivative of the dipole moment is given by [20]

$$\frac{dP(t)}{dt} = \frac{d}{dt}\int \rho(r',t)r'd^3r' = \int r'\frac{\partial\rho(r',t)}{dt}d^3r', \tag{5.3.3}$$

where $\rho(r',t)$ is the charge carrier density.

Now we can simplify the integration of Eq. 5.3.3 by using the continuity equation which is given by [20]

$$\nabla \cdot J + \frac{\partial\rho}{\partial t} = 0. \tag{5.3.4}$$

Substituting Eq. 5.3.4 into Eq. 5.3.3, and integrating by parts, we have

$$\frac{dP(t)}{dt} = -\int r'\nabla.J(r',t)d^3r' = \int J(r',t)d^3r', \tag{5.3.5}$$

where $J(r',t)$ is the photocurrent density. Assuming that the carrier transport is one dimensional, then we can integrate Eq. 5.3.5 from $-\frac{\omega_0}{2}$ to $\frac{\omega_0}{2}$, to obtain

$$\frac{dP(t)}{dt} = \int J(z',t)d^3r' = \int_{-\frac{\omega_0}{2}}^{\frac{\omega_0}{2}} I_{\mathrm{PC}}(z',t)dz' = \omega_0 I_{\mathrm{PC}}(t), \tag{5.3.6}$$

where I_{PC} is the photocurrent, and ω_0 is the spot size of the optical beam. By substituting Eq. 5.3.6 into Eq. 5.3.2, the THz dipole radiation becomes [20]

$$E_{\mathrm{THz}}(t) = \frac{\mu_0\omega_0 \sin\theta}{4\pi r}\frac{d}{dt_r}[I_{\mathrm{PC}}]\hat{\theta} \propto \frac{dI_{\mathrm{PC}}(t)}{dt}. \tag{5.3.7}$$

The above equation shows that the electric field of the THz dipole radiation is proportional to the time derivative of the photocurrent in the PC gap of the antenna [20].

5.3.2 Detection of THz pulses with a Photoconductive (PC) antenna

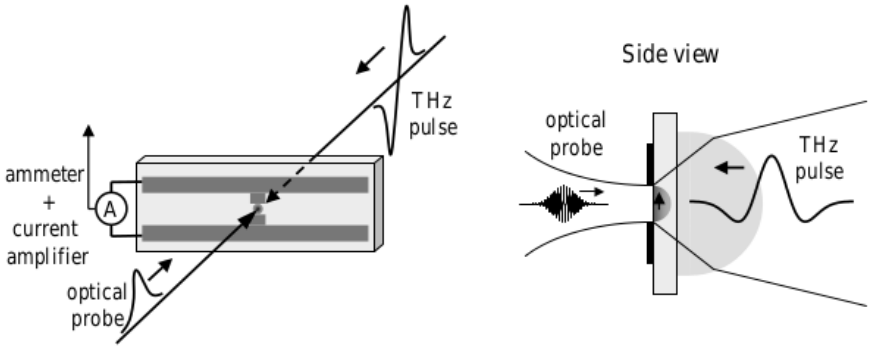

Figure 5.4: Schematic diagram of THz pulse detection with a photoconductive (PC) antenna, the small upper arrow in the PC gap area represents the current induced by incoming electric field with optical probe beam in the PC detector. [20].

The principle for the THz pulse detection in the PC antenna is very similar to the THz pulse generation method we discussed in the previous section [13]. In both methods (generation and detection), low temperature grown gallium arsenide (LT-GaAs) is the standard material used [31]. The carrier dynamics generated by the optical laser pulse as discussed in the previous section again are available for THz pulse detection in a PC antenna [20]. However, the main difference between the two methods is that the PC emitter is connected to a DC voltage, where the PC detector is connected to an ammeter [35]. Since there is no bias field in the PC detector, the incoming electric field of the THz pulse from the PC emitter will induce a current in the PC gap when the photocarriers are injected by the optical probe pulse as shown in Figure 5.4. For the time resolved waveform measurement, the photocurrent carrier lifetime is much shorter than the THz pulse duration [20]. The amplitude of the photocurrent induced through the receiving antenna is proportional to the amplitude of the incoming THz electric field. Both amplitude and phase information of the incoming THz field can be extracted by measuring the induced photocurrent [34]. The detected photocurrent density $J(t)$ in the PC detector depends on the time-dependent THz electric field $E(t)$ [47] as well as the transient surface conductivity $\sigma_s(t)$ as described by [20]

$$J(t) = \int_{-\infty}^{t} \sigma_s(t - t')E_{\mathrm{THz}}(t')dt'. \tag{5.3.8}$$

Chapter 6

Results and discussion

In this chapter we wish to use THz pulses to investigate the refractive index and absorption coefficient of specific materials. To achieve this task we need to study THz pulses before and after considering the effect of the sample. Thus we measure the electric field of THz pulses as it changes with time. The result of the measurement is shown in Figure 6.1.

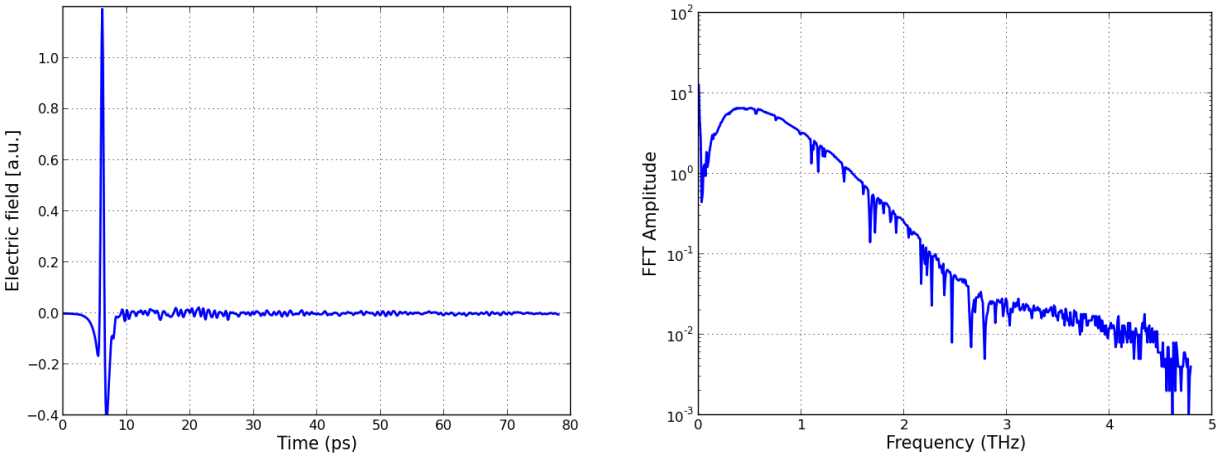

(a) (b)

Figure 6.1: (a) The electric field of the THz pulse versus time and (b) the spectrum obtained by applying a fast Fourier transform to the electric field of the THz pulse. This measurement was done in ambient air.

6.1 Water vapour

In contrary to what we expect of having a pure THz pulse, we notice various sharp resonances (absorption lines) at discrete frequencies in the frequency domain as shown in Figure 6.1(b). These can also be seen as small oscillations in the time domain signal as shown in Figure 6.1(a), which indicates the presence of a material, which is water vapour in our case. These absorption lines are due to the rotational transitions of the water vapour molecules [49].

Generally, the absorption of THz radiation by the Earth's atmosphere is characterized by two components. The first one is known as the line absorption contributions, which arise mainly from the resonance water vapour absorption. The second component is called continuum absorption,

which in practice is known as the residual absorption that is not contributed by the resonance water vapour spectrum [37, 18, 27]. The absorption coefficient depends on the pressure broadening of water vapour lines, which occur due to the collisions between water vapour molecules themselves as well as the other atmospheric molecules such as O_2 and N_2 [37, 53].

The detail of the interaction of water vapour with THz pulses depends on frequency. Water vapour has many modes, and it exhibits pure rotational modes of transition energies ranging from the millimetre wave to the mid infrared region [49, 17, 3].

Both pure rotational transition lines and rotation-vibration bands are distinct in the THz to infrared region [49, 8]. These transitions lead to the occurrence of the absorption of THz radiation in a number of narrow frequency bands, unique to the water vapour molecules [49].

As was mentioned our primary task is to investigate a sample solely, hence we need to remove the unwanted water vapour effect. This is done by flushing the experimental setup with Nitrogen gas, because it does not absorb THz radiation. The resulting electric field in time and frequency is shown in Figure 6.2.

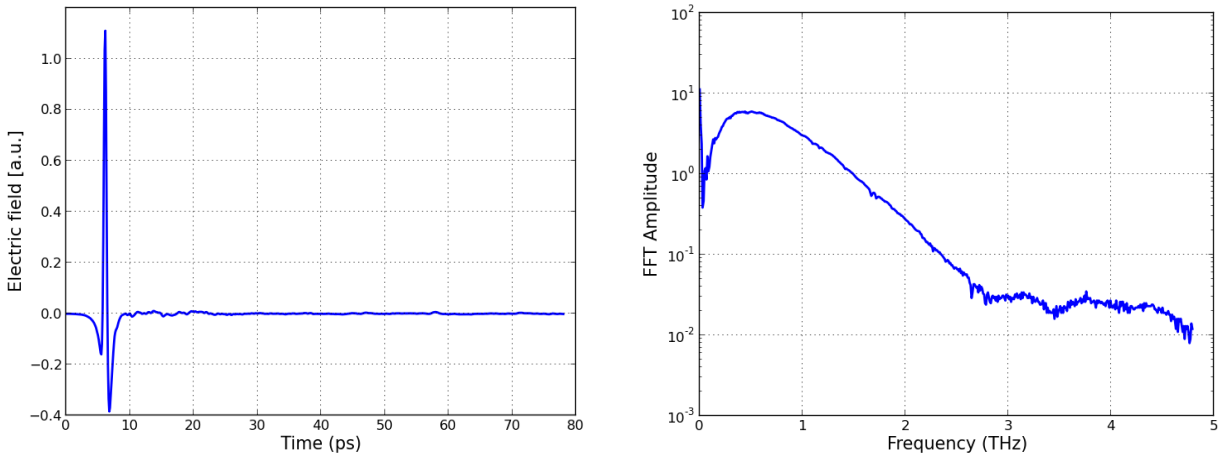

(a) (b)

Figure 6.2: (a) The electric field of the THz pulse versus time and (b) the spectrum obtained by applying a fast Fourier transform to the electric field of the THz pulse, after removing the water vapour.

As a result of removing the water vapour we see no absorption lines in Figure 6.2 which means that we successfully removed the unwanted water vapour by flushing with Nitrogen gas.

In our experiment, we first measure the electric field (E_{sam}) of the THz pulse in the presence of water vapour. Secondly we measure the electric field (E_{ref}) of the THz pulse in the absence of water vapour. From section 2.4, it has been shown that the refractive index and the absorption coefficient can be obtained as [42, 52, 21]

$$n(\omega) = \left[(\phi_{\text{ref}} - \phi_{\text{sam}})\frac{c}{\omega d}\right] + 1, \tag{6.1.1}$$

and

$$\alpha(\omega) = 2\left[\ln\left(\frac{E_{0\text{sam}}}{E_{0\text{ref}}}\right)\right]/d. \tag{6.1.2}$$

Where d is the measured distance between the emitter and the detector. From the above two equations, we calculated the refractive index and the absorption coefficient for water vapour, and the results are shown in Figure 6.3.

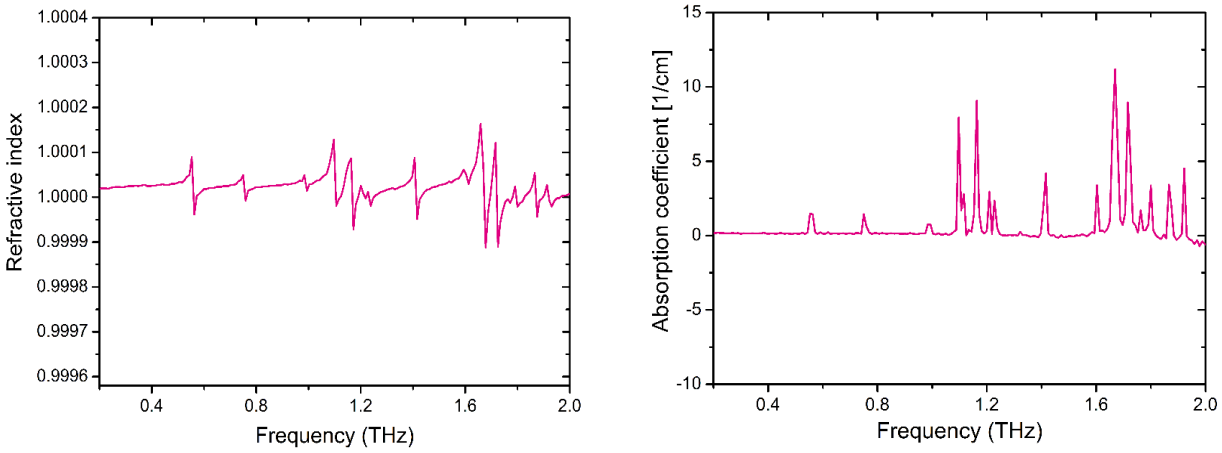

(a) (b)

Figure 6.3: (a) Refractive index of a 0.27 m atmospheric sample containing water vapour versus frequency obtained via Eq. 6.1.1, and (b) the absorption spectrum of the same sample versus frequency in the spectral range 0.2 to 2.0 obtained via Eq. 6.1.2 [20].

Figure 6.3(a) shows the frequency dependent refractive index of a 0.27 m atmospheric sample containing water vapour in the spectral range 0.2 to 2.0 which is calculated using Eq. 6.1.1, and (b) the frequency dependent absorption coefficient of the same sample in the same spectral range which is calculated using Eq. 6.1.2. As can be seen in (a) at the specific frequencies, there are dips which correspond to the absorption lines in the absorption spectrum of the sample as shown in (b). The measured $n(\omega)$ and $\alpha(\omega)$ spectra in Figure 6.3 agree with the change of $n(\omega)$ and $\kappa(\omega)$ as given by theory and illustrated in Figure 2.2.

6.2 Investigating Silicon properties

The sample that we investigate is Silicon with thickness 0.3 mm. For the measurement of the refractive index of silicon, we consider the electric field of the THz pulse E_0 incident on the silicon sample. The results obtained from the experiment are shown in Figure 6.4.

Figure 6.4(b) shows three distinct peaks, labelled (1), (2) and (3). This observation can be related to the multiple reflections inside the material. We can explain the three observable peaks as follows by referring to Figure 2.29. The first peak, labelled as (1), is part of the pulse that passes the material on the way to the detector without undergoing multiple reflections in the material (E_1 in Figure 2.29). The second peak is part of the pulse that undergoes two reflections inside the material and then makes its way to the detector (E_2 in Figure 2.29). The third peak is part of the pulse that undergoes four reflections (and hence travels 5 times through the material) and then makes its way to the detector (E_3 in Figure 2.29).

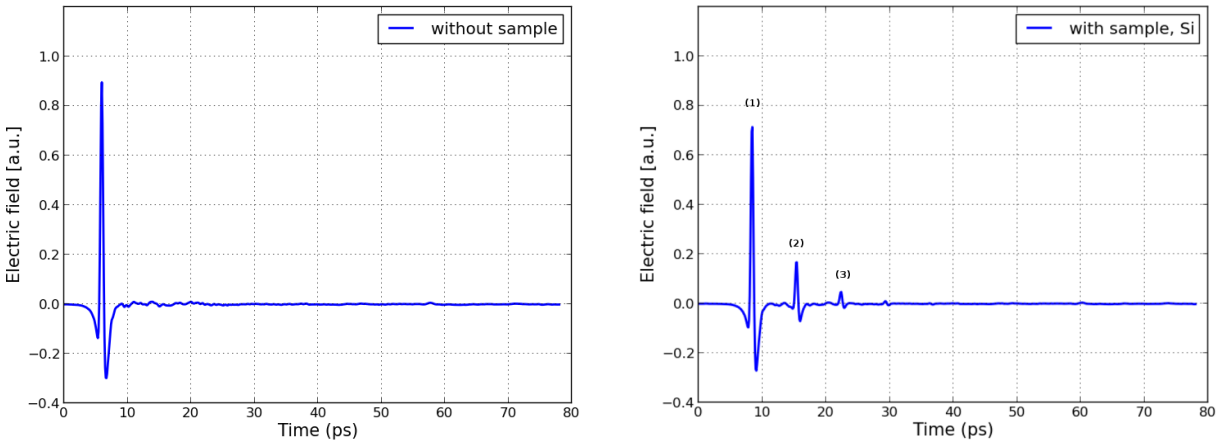

(a) (b)

Figure 6.4: (a) The electric field versus time without the sample and (b) the electric field versus time with the Silicon sample, as labelled.

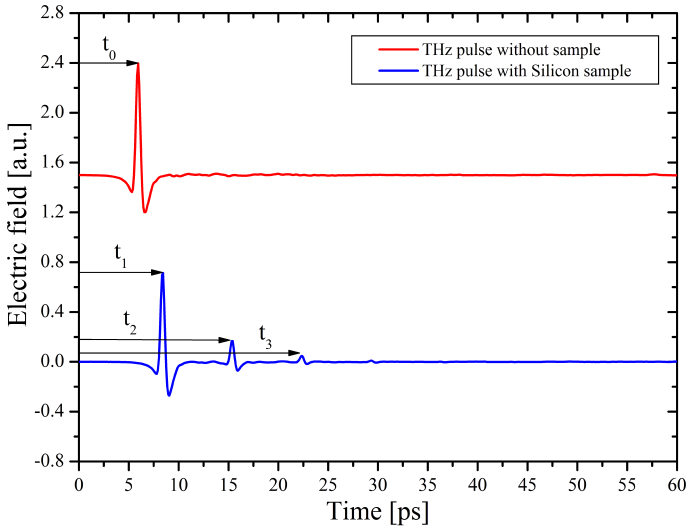

Figure 6.5: THz pulse without sample and with Silicon sample. The pulse without sample offset for clarity.

Now we wish to compute the average refractive index of the Silicon sample. By subtracting Eq. 2.7.3 from Eq. 2.7.1, we have

$$(t_1 - t_0) = \frac{D-d}{c} + \frac{n\,d}{c} - \frac{D}{c}. \tag{6.2.1}$$

This implies that

$$n = \frac{c}{d}(t_1 - t_0) + 1 \equiv n_a, \tag{6.2.2}$$

where n_a is the refractive index calculated using peak 1.

Using peak 2, and by subtracting Eq. 2.7.4 from Eq. 2.7.3, we have

$$(t_2 - t_1) = \frac{D-d}{c} + \frac{3n\,d}{c} - \frac{D-d}{c} - \frac{n\,d}{c}. \tag{6.2.3}$$

This implies that

$$n = \frac{c}{2d}(t_2 - t_1) \equiv n_b, \tag{6.2.4}$$

where n_b is the refractive index calculated using peak 2.

Using peak 3, and by subtracting Eq. 2.7.5 from Eq. 2.7.4, we have

$$(t_3 - t_2) = \frac{D-d}{c} + \frac{5n\,d}{c} - \frac{D-d}{c} - \frac{3n\,d}{c}. \tag{6.2.5}$$

This implies that

$$n = \frac{c}{2d}(t_3 - t_2) \equiv n_c, \tag{6.2.6}$$

where n_c is the refractive index calculated using peak 3.

We compute the refractive index of the Silicon sample by using equations 6.2.2, 6.2.4 and 6.2.6, and the resulting n is the same for the three values of t (as shown in Table.6.1) as the material has a unique refractive index. Based on our experiment, the values of n we obtained are summarized in Table.6.2. These values were calculated using the time corresponding to the three peaks respectively.

t_0(ps)	t_1 (ps)	t_2(ps)	t_3(ps)	d (mm)
5.94	8.44	15.42	22.40	0.30

Table 6.1: Time measured for the Silicon sample.

n_a	n_b	n_c	average ($\bar{n}$)
3.50	3.49	3.49	3.49

Table 6.2: Refractive index for Silicon sample.

These measurements constitute the refractive index of Silicon, averaged across the frequency range. In order to determine the frequency dependent refractive index, we can make use of Eq. 6.1.1. We unfortunately can't make use of the complete measured temporal data as measured in Figure 6.4(b) as this contains the multiple reflections. These multiple reflections introduces artefacts in the spectral data. To calculate the refractive index using Eq. 6.1.1 we therefore only used the temporal data between 0 and 13 ps, before the first Fabry Perot reflection. The fast Fourier transform of this truncated temporal data set was used to calculate the spectral phase used in Eq. 6.1.1. The results of this procedure is shown in Figure 6.6.

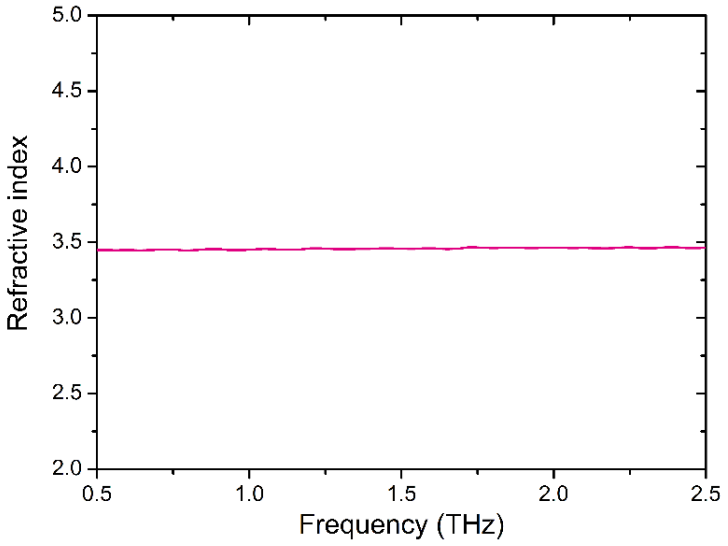

Figure 6.6: Refractive index of Silicon vs frequency obtained via Eq. 6.1.1.

As can be seen in Figure 6.6, the refractive index of Silicon does not vary significantly with frequency. It should also be noted that the resolution with which one can extract the frequency dependent refractive index with this technique is limited by the temporal window before the first Fabry Perot reflection, which is determined by the thickness of the sample.

In summary, we measured the electric field of the THz pulse before and after passing through the Silicon sample. In this way, we were able to investigate the refractive index of the sample. Due to multiple reflection that occur inside the sample, three distinct peaks are observed. Each of these peaks can be used to calculate the refractive index. The three calculations are almost the same. Eq. 6.1.1 can also be used to determine the refractive index of Silicon. Figure 6.6 shows the result using this method.

6.3 Investigating Sapphire properties

In the previous section, the sample investigated was Silicon and we observed three distinct peaks in the electric field. We would like to know whether we can obtain similar results if we consider different materials. The sample considered in this section is Sapphire of thickness 1.94 mm. The same techniques that were used for the Silicon sample are again used. The results of our experiment are depicted in Figure 6.7.

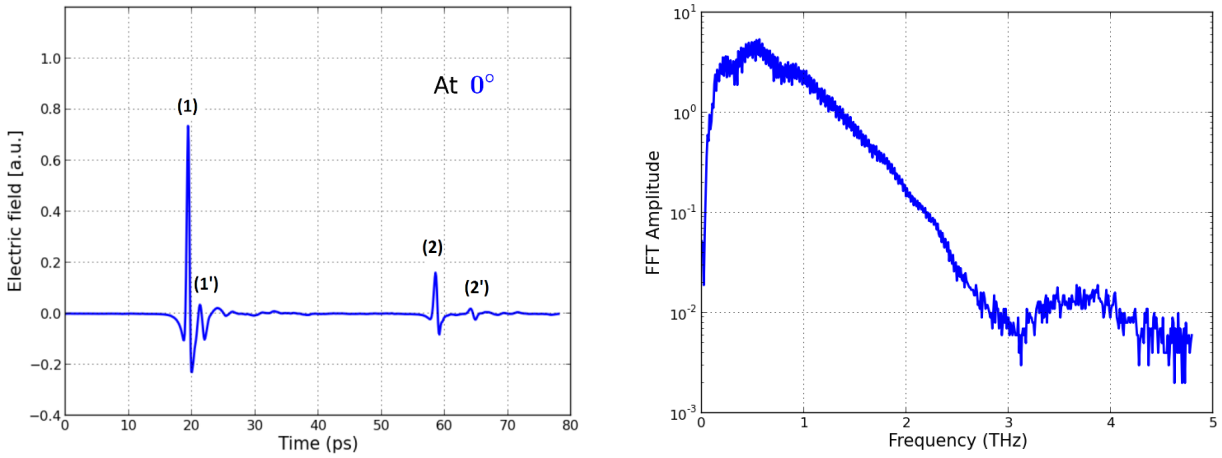

(a) (b)

Figure 6.7: (a) The electric field of the THz pulse versus time and (b) the spectrum obtained by applying a fast Fourier transform to the electric field of the THz pulse. The sample (Sapphire) was placed in a rotational mount in order to able to measure its relative orientation with respect to the incident polarization.

Figure 6.7(a) shows that the results obtained in the case of Sapphire are similar to those obtained for Silicon, except that in the former, we observe two peaks succeeding each other labelled as (1), (1′), (2) and (2′). This might be related to the refractive index of the material. It is clearly observed that peak (2) is smaller compared to peak (1) and peak (2′) is also smaller compared to peak (1′) because of multiple reflection inside the sample. The observed modulations in the spectrum are due to the four distinct peaks. As we do not know the configuration of the sample's optical axes we are going to rotate the optical axes by 15° at time using the rotation mount, to see the effect of rotation on the behaviour of the four observable peaks.

After we rotate the sample by 15° using the rotation mount, the result of our measurement is shown in Fiq.6.8.

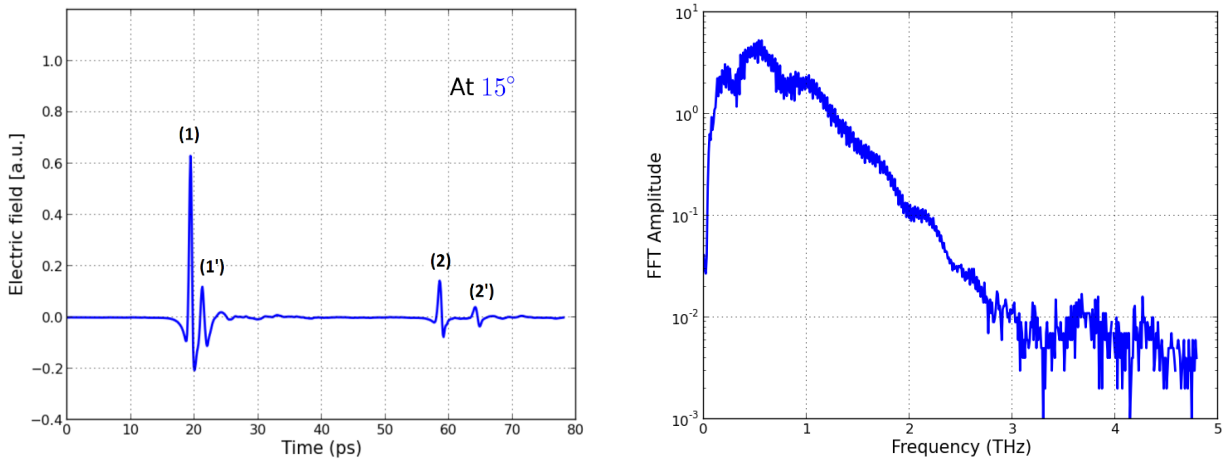

(a) (b)

Figure 6.8: (a) The electric field of the THz pulse versus time and (b) the spectrum obtained by applying a fast Fourier transform to the electric field of the THz pulse. The sample (Sapphire) with angle measured as 15° relative to the original orientation.

We notice that peaks (1′) and (2′) become bigger where as peaks (1) and (2) slightly decrease. The reason is that the angle of the incident THz pulse's polarization with respect to the optical axes has been changed. As a result of having peaks (1′) and (2′) increase significantly, we observed that the modulations in the spectrum, Figure 6.8(b), increase considerably.

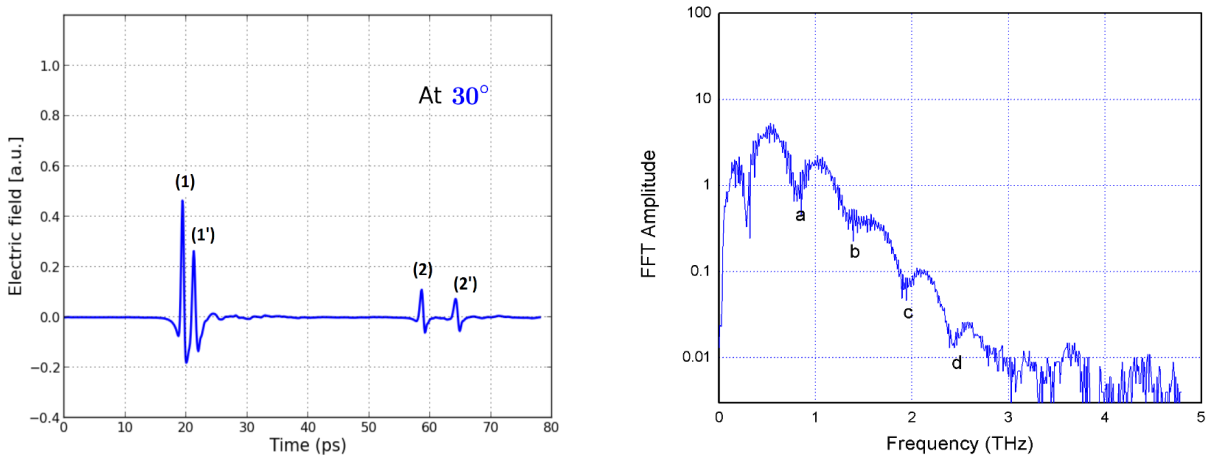

(a) (b)

Figure 6.9: (a) The electric field of the THz pulse versus time and (b) the spectrum obtained by applying a fast Fourier transform to the electric field of the THz pulse. The sample (Sapphire) with angle measured as 30° with relative to the original orientation.

Figure 6.9 shows that with the sample at 30° peaks (1′) and (2′) increased considerably and the modulations in the spectrum increased as well.

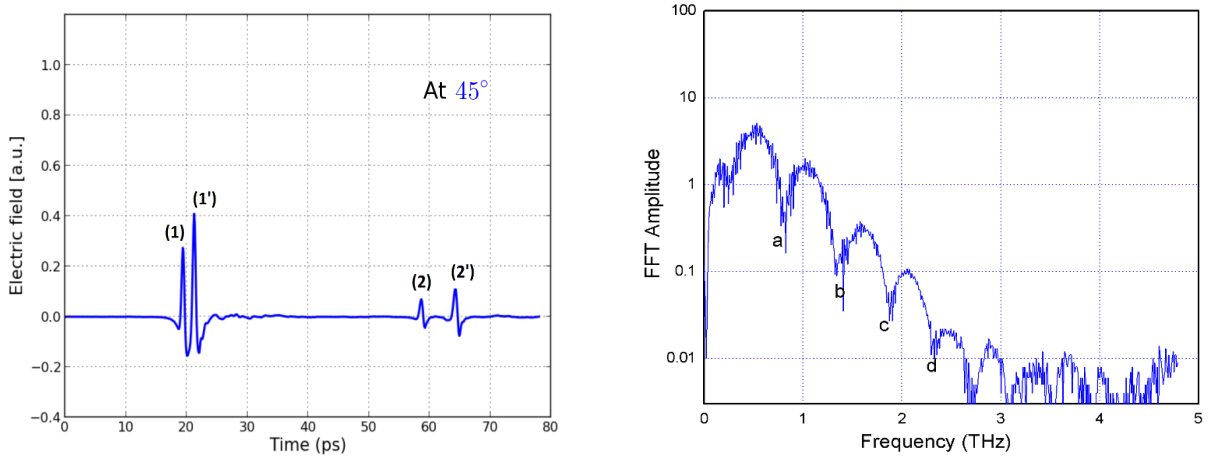

(a) (b)

Figure 6.10: (a) The electric field of the THz pulse versus time and (b) the spectrum obtained by applying a fast Fourier transform to the electric field of the THz pulse. The sample (Sapphire) with angle measured as 45° relative to the original orientation.

Figure 6.10 interestingly, shows that with the sample at 45° peaks (1) and (2) become smaller than peaks (1′) and (2′) respectively, and in the spectrum the modulations increase considerably.

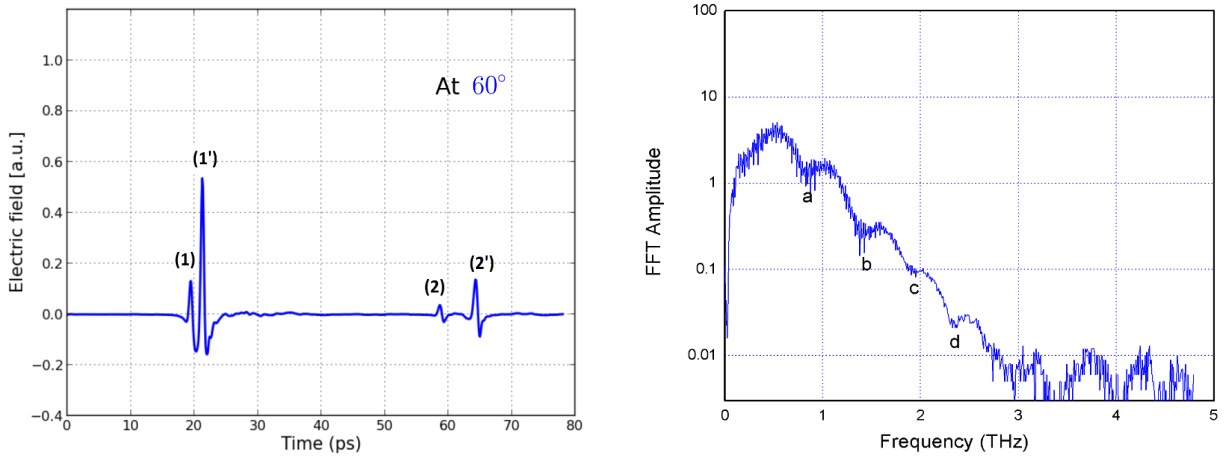

(a) (b)

Figure 6.11: (a) The electric field of the THz pulse versus time and (b) the spectrum obtained by applying a fast Fourier transform to the electric field of the THz pulse. The sample (Sapphire) with angle measured as 60° relative to the original orientation.

Figure 6.11 shows that with the sample at 60° peaks (1) and (2) continues decreasing and as a result the modulations in the spectrum decrease.

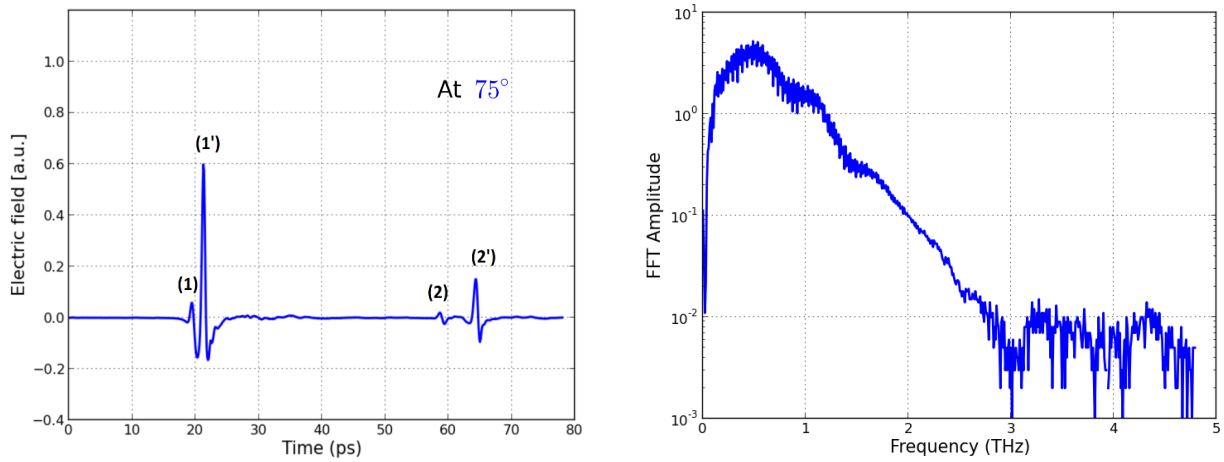

(a) (b)

Figure 6.12: (a) The electric field of the THz pulse versus time and (b) the spectrum obtained by applying a fast Fourier transform to the electric field of the THz pulse. The sample (Sapphire) with angle measured as 75° relative to the original orientation.

In Figure 6.12 with the sample at 75° peaks (1) and (2) have almost disappeared, and so have the modulations in the spectrum.

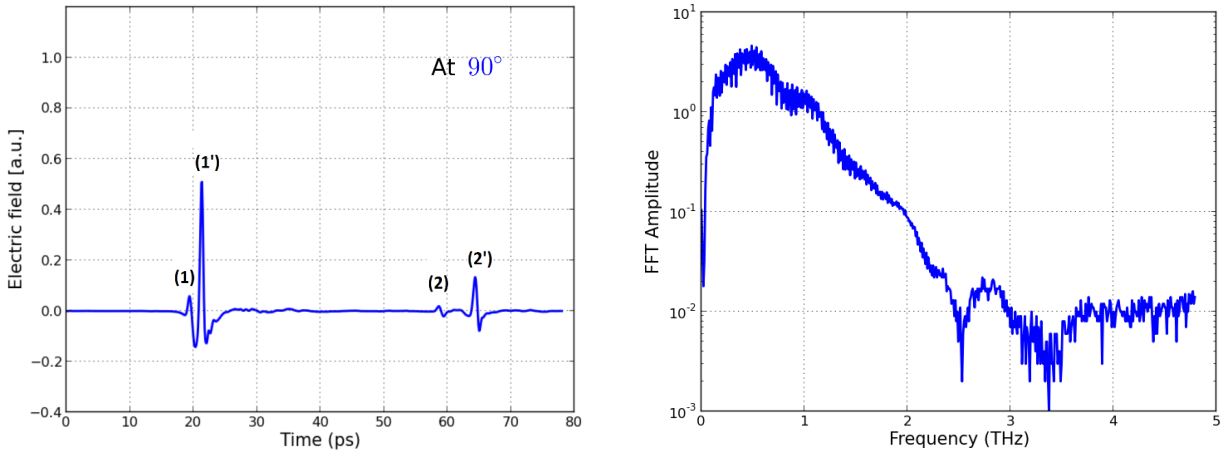

(a) (b)

Figure 6.13: (a) The electric field of the THz pulse versus time and (b) the spectrum obtained by applying a fast Fourier transform to the electric field of the THz pulse. The sample (Sapphire) with angle measured as 90° relative to the original orientation.

Figure 6.12 (sample at 75°) and Figure 6.13 (sample at 90°) look almost identical.

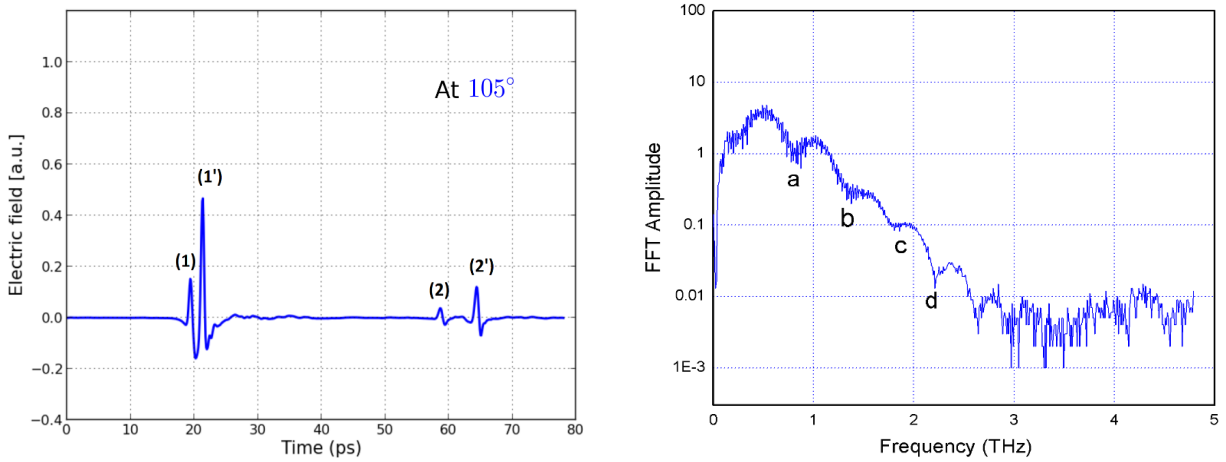

(a) (b)

Figure 6.14: (a) The electric field of the THz pulse versus time and (b) the spectrum obtained by applying a fast Fourier transform to the electric field of the THz pulse. The sample (Sapphire) with angle measured as 105° relative to the original orientation.

Figure 6.14 shows that with the sample at 105°peaks (1) and (2) start increasing again and hence the modulations in the spectrum increase as well.

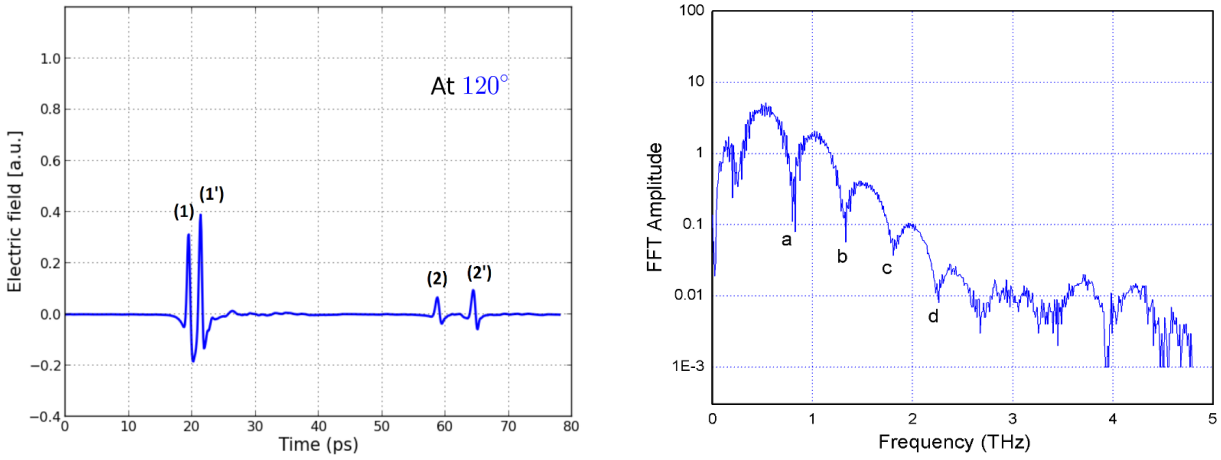

(a) (b)

Figure 6.15: (a) The electric field of the THz pulse versus time and (b) the spectrum obtained by applying a fast Fourier transform to the electric field of the THz pulse. The sample (Sapphire) with angle measured as 120° relative to the original orientation.

In figure 6.15 (sample at 120°) the four peaks are almost equal and consequently stronger modulations are observed in the spectrum.

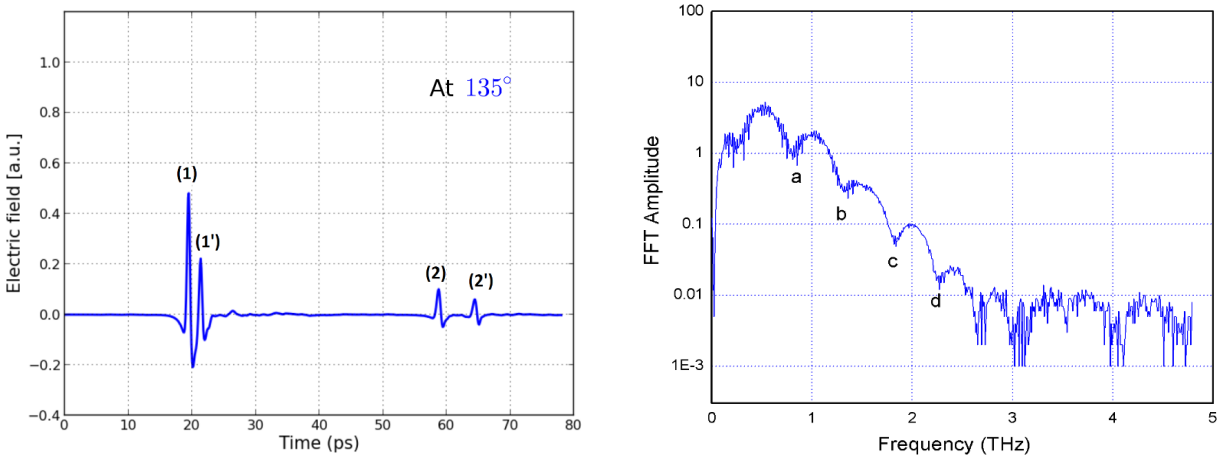

(a) (b)

Figure 6.16: (a) The electric field of the THz pulse versus time and (b) the spectrum obtained by applying a fast Fourier transform to the electric field of the THz pulse. The sample (Sapphire) with angle measured as 135° relative to the original orientation.

Figure 6.16 (sample at 135°) shows that peaks (1) and (2) become bigger than peaks (1′) and (2′) respectively and in the spectrum, the modulations decrease considerably.

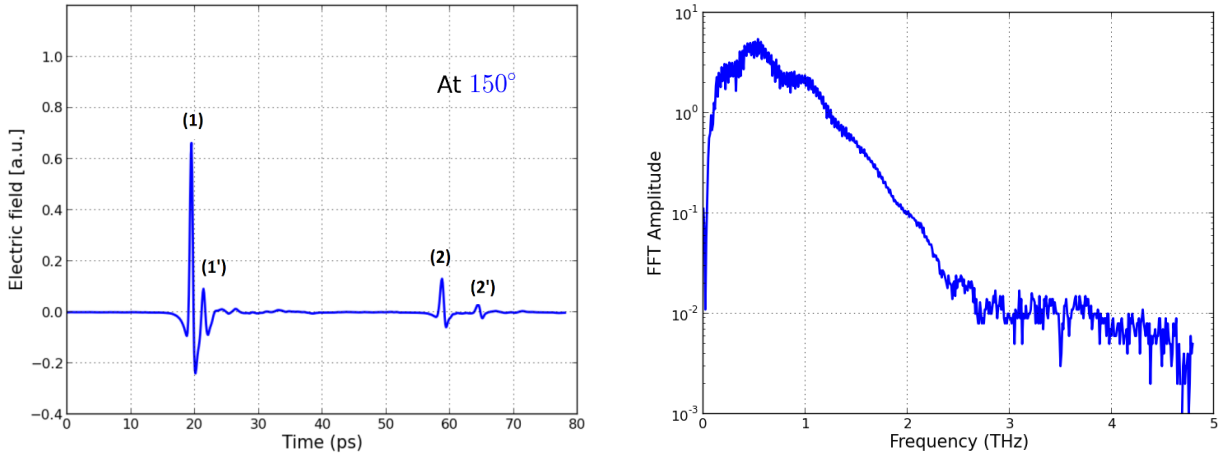

(a) (b)

Figure 6.17: (a) The electric field of the THz pulse versus time and (b) the spectrum obtained by applying a fast Fourier transform to the electric field of the THz pulse. The sample (Sapphire) with angle measured as 150° relative to the original orientation.

Figure 6.17 (sample at 150°) shows that peaks (1′) and (2′) decrease considerably and thus the modulations in the spectrum decrease as well.

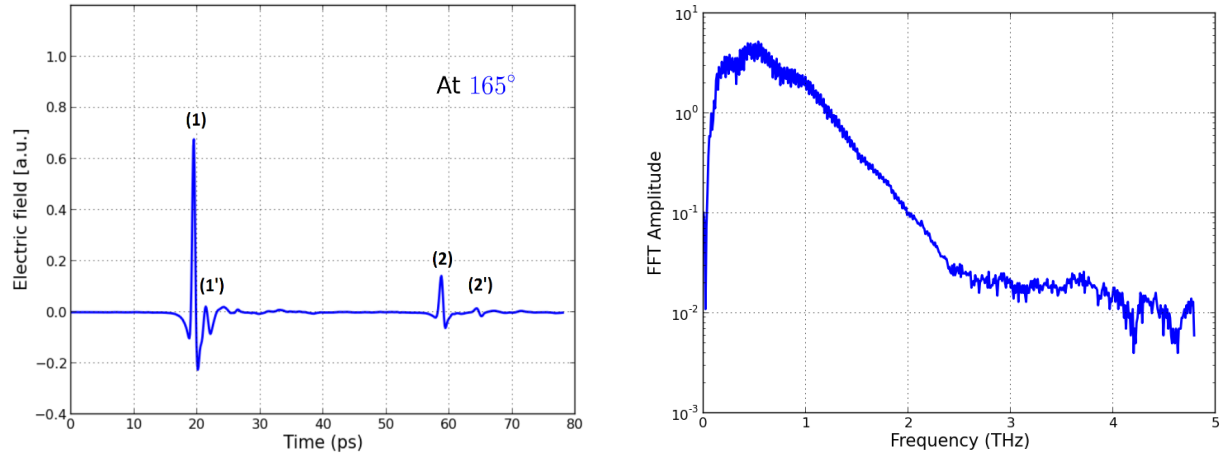

(a) (b)

Figure 6.18: (a) The electric field of the THz pulse versus time and (b) the spectrum obtained by applying a fast Fourier transform to the electric field of the THz pulse. The sample (Sapphire) with angle measured as 165° relative to the original orientation.

Figure 6.17 looks very similar to Figure 6.18 (sample at 165°).

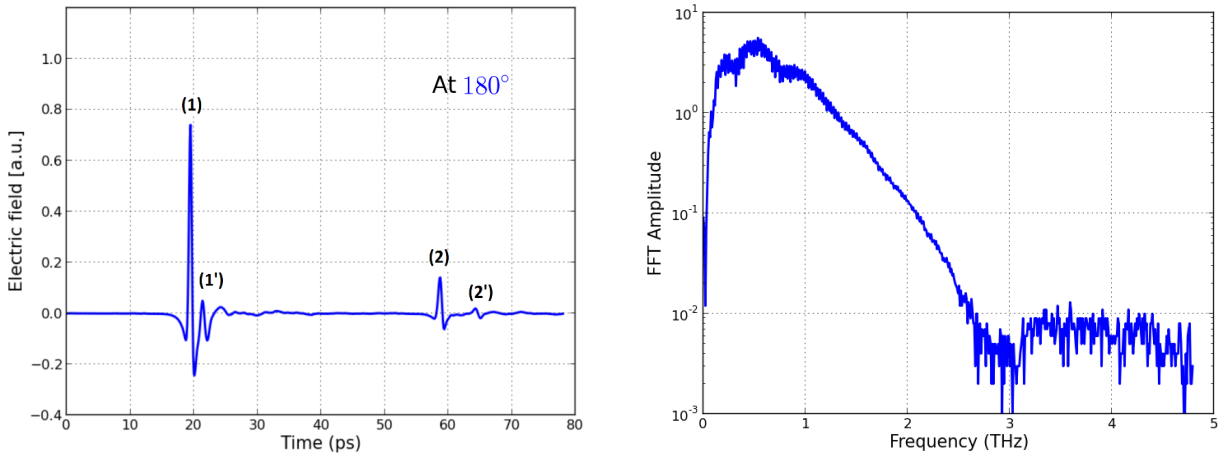

(a) (b)

Figure 6.19: (a) The electric field of the THz pulse versus time and (b) the spectrum obtained by applying a fast Fourier transform to the electric field of the THz pulse. The sample (Sapphire) with angle measured as 180° relative to the original orientation.

Figure 6.19 (sample at 180°) shows that peaks $(1')$ and $(2')$ continues to decrease and as a result the modulations in the spectrum decrease.

All figures considered above, the positions of the four peaks are fixed meaning that no matter what the angle of rotation is, the four peaks occur at a fixed time. However the amplitude of each peak change significantly with the angle of rotation.

Angle of rotation (ϕ)	a (THz)	b (THz)	c (THz)	d (THz)
30°	0.853	1.388	1.941	2.466
45°	0.797	1.322	1.875	2.361
60°	0.872	1.397	1.922	2.372
105°	0.797	1.331	1.856	2.259
120°	0.825	1.331	1.838	2.259
135°	0.825	1.331	1.866	2.316

Table 6.3: Positions of the minimum values in term of frequency for the measured spectra from Figures 6.9(b), 6.10(b), 6.11(b), 6.14(b), 6.15(b) and 6.16(b).

Angle of rotation (ϕ)	$\Delta f = (b - a)$ (THz)	$\Delta f = (d - c)$ (THz)	$\Delta f = (c - b)$ (THz)	Average (THz)
30°	0.535	0.525	0.555	0.535
45°	0.525	0.505	0555	0.530
60°	0.525	0.450	0.525	0.500
105°	0.535	0.405	0.525	0.485
120°	0.505	0.420	0.505	0.480
135°	0.505	0.450	0.535	0.495

Table 6.4: Difference between the positions of the minimum values in terms of frequency for the measured spectra, rounded to the nearest 0.005.

Angle of rotation (ϕ)	$T = (t_1' - t_1)$ (ps)	$F = \frac{1}{T}$ (THz)
30°	1.90	0.52
45°	1.90	0.52
60°	1.95	0.51
105°	1.95	0.51
120°	1.90	0.52
135°	1.90	0.52

Table 6.5: Frequency calculated using the measured time, rounded to the nearest 0.05.

Table 6.3 shows the positions of the minimum values in the measured spectra for different angles of rotation of the Sapphire sample, and the difference (Δf) between the positions of the minimum values in the measured spectra is shown in Table 6.4.

We calculated the frequency difference (Δf) between the minima of our measured spectra at different angles of rotation of the Sapphire sample, in order to show that the $\Delta f'$s are equal for all the calculations, and the results are shown in Table 6.4.

In Table 6.5, the frequency (F) is calculated by using the arrival time of the pulses measured in the time domain for different angles of rotation of the Sapphire sample. These values are compared with the $\Delta f's$ to show that they are equal (within experimental error). This confirms that the modulations in the spectra are as a result of the multiple pulses in the time domain.

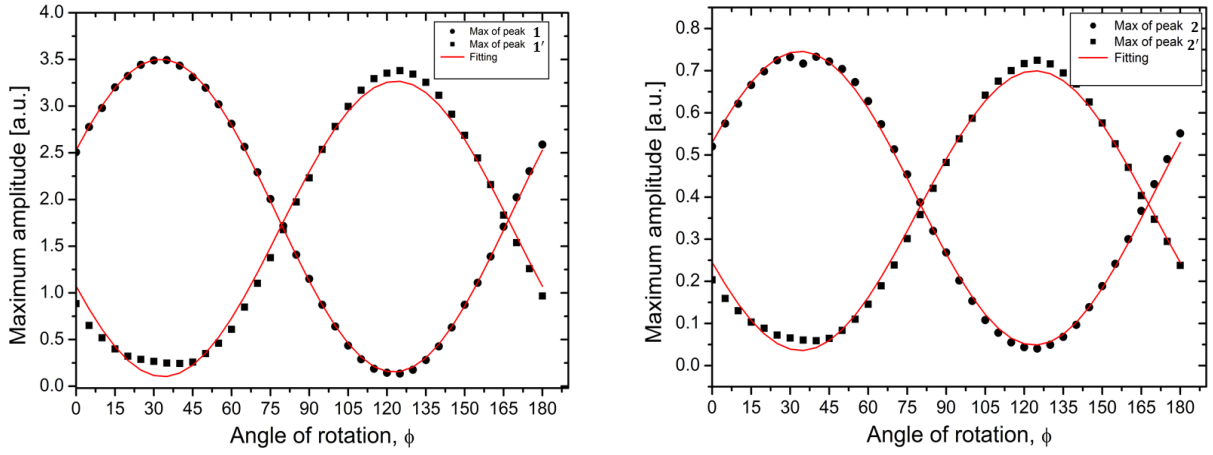

(a) (b)

Figure 6.20: The points represent the measured maxima of the peaks in the time domain, while the solid lines represent a fit to the data according to Eq. 6.3.1. The sample was rotated 5° at a time.

Figure 6.20 shows the result of our experiment in which we rotate the sample (Sapphire) by 5° at a time in order to determine the direction of the optical axes of the sample. The maxima of peaks 1 and $1'$ are plotted as function of angle ϕ.

We use Origin Pro7 to fit our data with the following equation

$$y = y_\circ + A \times cos^2(\phi - \Theta_c). \tag{6.3.1}$$

The parameters $y_\circ$, and A vary according to the peak. For peak (1) we find $y_\circ = 0.15$, and the maximum amplitude $A = 3.35$, and $\Theta_c = 32.59$. For peak (2) we find $y_\circ = 0.24$, and the maximum amplitude $A = 3.12$, and $\Theta_c = 123.65$. For peak (3) we find $y_\circ = 0.04$, and the maximum amplitude $A = 0.71$, and $\Theta_c = 33.79$, and for peak (4) we find $y_\circ = 0.05$, and the maximum amplitude $A = 0.69$, and $\Theta_c = 124.20$,

The Figure 6.20 shows that the sample is birefringent. From the figure, we can determine the direction of the two optical axes. The one is at 123.9° relative to the original orientation and the other is at 33.2°, approximately 90° with respect to each other.

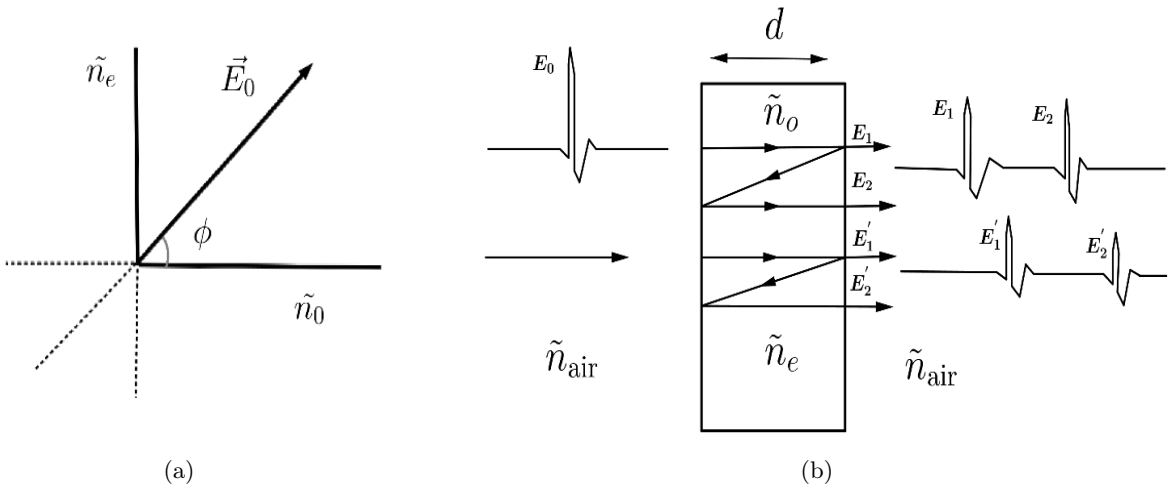

(a) (b)

Figure 6.21: (a) The electric field and angle ϕ relative to the ordinary optical axis of the material and (b) multiple reflections at the Sapphire sample interfaces.

Figure 6.21(a) show the direction of the incident electric field along an arbitrary axis of the Sapphire sample, and we see that the electric field has two components along the two optical axis. The interaction of the electric field of the THz pulse with the Sapphire sample is illustrated in Figure 6.21(b).

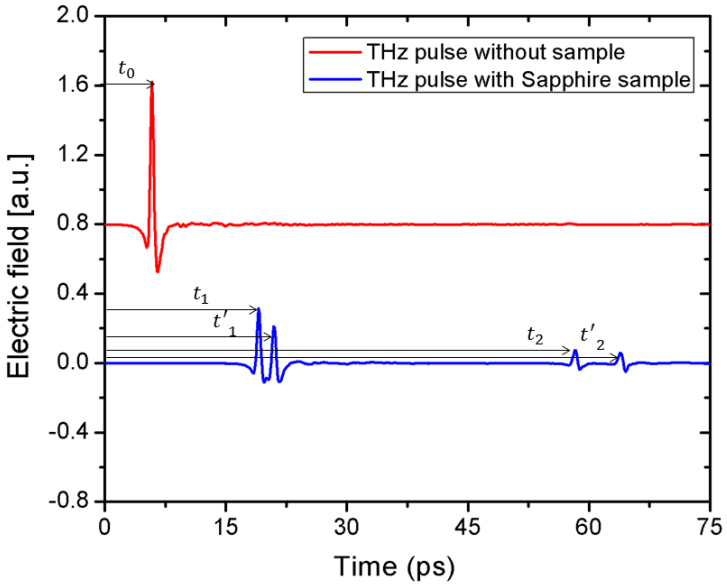

Figure 6.22: THz pulse without sample and with Sapphire sample. The pulse without sample is offset for clarity.

Now we wish to compute the refractive indices of the Sapphire sample. According to Figure 6.21(b), Figure 6.22 and by using Eq. 2.7.3 we can write the different times the THz pulse takes to propagate through the sample as follows:

for peaks (1) and (1′), we can write

$$t_1 = \frac{D-d}{c} + \frac{n\,d}{c}, \tag{6.3.2}$$

and

$$t_1^{'} = \frac{D-d}{c} + \frac{n^{'}\,d}{c}. \tag{6.3.3}$$

For peaks (2) and (2′), we can write

$$t_2 = \frac{D-d}{c} + \frac{3n\,d}{c}, \tag{6.3.4}$$

and

$$t_2^{'} = \frac{D-d}{c} + \frac{3n^{'}\,d}{c}. \tag{6.3.5}$$

As already mentioned, the Sapphire sample is birefringent, therefore, it has two refractive indices n_e and n_o. We can write the different forms of these indices by subtracting Eq. 2.7.1 from Eq. 6.3.2 and Eq. 2.7.1 from Eq. 6.3.3, respectively.

Now by subtracting Eq. 2.7.1 from Eq. 6.3.2, then we have

$$\begin{aligned}(t_1 - t_0) &= \frac{D-d}{c} + \frac{n\,d}{c} - \frac{D}{c} \\ &= -\frac{d}{c} + \frac{n\,d}{c} = \frac{d}{c}(n-1) \\ (n-1) &= \frac{c}{d}(t_1 - t_0),\end{aligned}$$

therefore

$$\boxed{n = \frac{c}{d}(t_1 - t_0) + 1 \equiv n_a.} \tag{6.3.6}$$

By subtracting Eq. 2.7.1 from Eq. 6.3.3, then we have

$$\begin{aligned}(t_1^{'} - t_0) &= \frac{D-d}{c} + \frac{n'\,d}{c} - \frac{D}{c} \\ &= -\frac{d}{c} + \frac{n'\,d}{c} = \frac{d}{c}(n'-1) \\ (n'-1) &= \frac{c}{d}(t_1^{'} - t_0),\end{aligned}$$

therefore

$$\boxed{n' = \frac{c}{d}(t_1^{'} - t_0) + 1 \equiv n_{a'}.} \tag{6.3.7}$$

Another different form of these indices can be written by subtracting Eq. 6.3.2 from Eq. 6.3.4 and Eq. 6.3.3 from Eq. 6.3.5, respectively.

By subtracting Eq. 6.3.2 from Eq. 6.3.4, then we have

$$(t_2 - t_1) = \frac{D-d}{c} + \frac{3n\,d}{c} - \frac{D-d}{c} - \frac{n\,d}{c} = \frac{2n\,d}{c},$$

therefore

$$\boxed{n = \frac{c}{2d}(t_2 - t_1) \equiv n_b.} \tag{6.3.8}$$

By subtracting Eq. 6.3.3 from Eq. 6.3.5, then we have

$$(t_2^{'} - t_1^{'}) = \frac{D-d}{c} + \frac{3n'\,d}{c} - \frac{D-d}{c} - \frac{n'\,d}{c} = \frac{2n'\,d}{c},$$

therefore

$$\boxed{n' = \frac{c}{2d}(t_2^{'} - t_1^{'}) \equiv n_{b'}\,.} \tag{6.3.9}$$

The difference in the refractive indices Δn is then given by

$$\Delta n = n - n'. \tag{6.3.10}$$

The values of n we obtained are summarized in Table.6.6.

	n		$n^{'}$		Average	
θ°	n_a	$n_{a'}$	n_b	$n_{b'}$	$\bar{n} \equiv n_o$	$\bar{n}^{'} \equiv n_e$
0	3.04	3.02	3.33	3.31	3.03	3.32
15	3.04	3.02	3.33	3.31	3.03	3.32
30	3.04	3.03	3.33	3.31	3.04	3.32
45	3.04	3.03	3.33	3.32	3.04	3.33
60	3.06	3.02	3.33	3.32	3.04	3.33
75	3.06	3.02	3.33	3.33	3.04	3.33
90	3.04	3.03	3.35	3.32	3.04	3.33
105	3.04	3.03	3.35	3.32	3.04	3.33
120	3.06	3.03	3.35	3.32	3.04	3.33
135	3.06	3.03	3.35	3.32	3.04	3.33
150	3.06	3.03	3.35	3.32	3.04	3.33
165	3.06	3.03	3.35	3.32	3.04	3.33
180	3.06	3.03	3.35	3.31	3.04	3.33

Table 6.6: Average refractive indices measured for the Sapphire sample.

In summary, the results obtained in the case of Sapphire are similar to those obtained for Silicon, except that in the former, we observe two peaks succeeding each other. Using the concept of multiple reflections which occur inside the material, we were able to obtain two distinct refractive indices. Two different methods were used to calculate the refractive index, and similar results were obtained in both cases. The fact that we obtained two different refractive indices, confirms that Sapphire is a birefringent material.

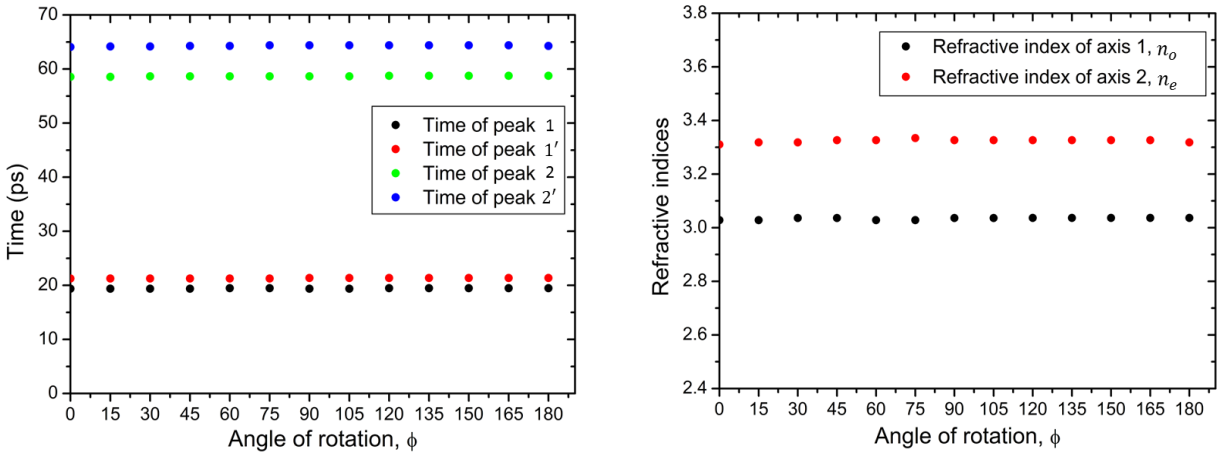

(a) (b)

Figure 6.23: (a) Time at which the peaks are observed as a function of the angle of rotation and (b) Refractive index as a function of the angle of rotation.

Figure 6.23(a) shows that the times at which the peaks are observed are constant with respect to the angle of rotation as expected. We have plotted the refractive indices calculated using Eq. 6.3.6 and Eq. 6.3.7 against the angle of rotation to demonstrate that the refractive indices associated with each peak is constant with respect to the angle of rotation as shown in Figure 6.23(b). In the figure, the values of the two refractive indices, n_e and n_o of the sample were found to be 3.326 and 3.036 respectively. The difference between the refractive indices (i.e., Δn) is approximately 0.29.

In Table 6.7 we summarized the comparison between the method used for computing the refractive indices of Silicon and Sapphire samples in the THz region (as its discussed in section 6.2 and section 6.3) and the literature values.

Material	Literature	Our method
Silicon	$n \simeq 3.42$ [20]	$n \simeq 3.49$
Sapphire	$n_o \simeq 3.05$, and $n_e \simeq 3.40$ [20]	$n_o \simeq 3.04$, and $n_e \simeq 3.33$

Table 6.7: Comparison between literature and the method used in obtaining the refractive indices .

6.4 Investigating polymers properties

In this section we will investigate the properties of various polymer samples. For the measurement of the refractive indices and absorption coefficients of the polymers, we first measured the electric field of the THz pulse, E_{ref}, before passing through the samples, as shown in Figure 6.24, after which we measure the pulse that has passed through the samples.

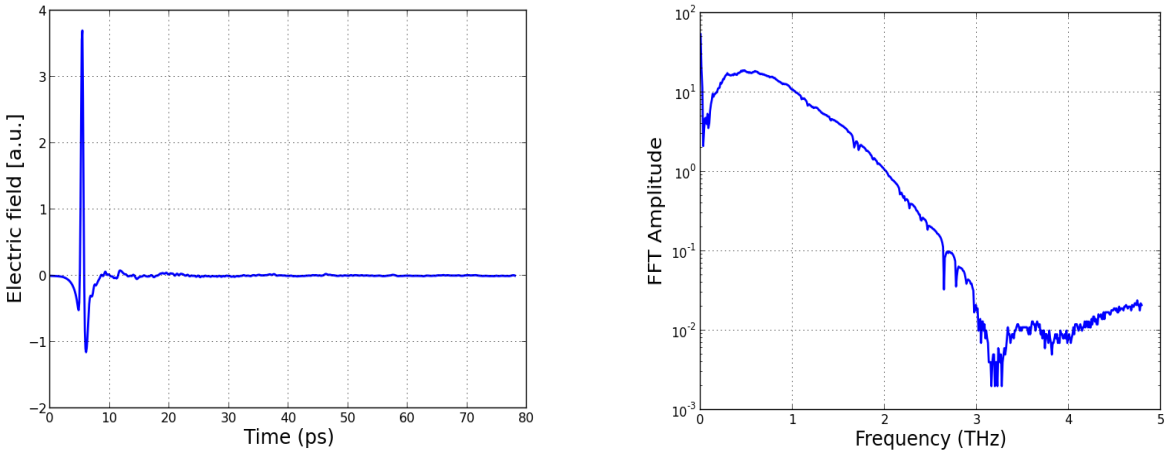

(a) (b)

Figure 6.24: (a) The electric field of the THz pulse versus time (without sample) and (b) the spectrum obtained by applying a fast Fourier transform to the electric field of the THz pulse.

Terahertz time domain spectroscopy (THz TDS) is a technique that can be used for measuring a material's optical parameters such as refractive index and absorption coefficient over a wide frequency range [30]. In the last decade several algorithmic techniques for material parameter extraction, used to determine the absorption coefficient and refractive index of solid samples with THz TDS have been developed. In our measurements for parameter extraction, we used software called Teramat (Menlo System GmbH) to determine the refractive index and absorption coefficient. To do this a THz pulse measured before passing through sample is compared to a THz pulse obtained after it has propagated through the sample [30].

In this section we will show some experimental results from various polymers using the Teramat software for the material parameter extraction. For each material parameter extraction, we performed both a measurement of the reference pulse and the pulse after it has passed through the sample. We also measured the thickness of the sample with a screw micrometer [30].

The first sample considered in this section was Teflon, which had a thickness of 0.23 mm. The same techniques that were used for measuring the electric field of the THz pulse passing through the Silicon and Sapphire samples in the previous sections are again implemented. The results of our experiment are depicted in Figure 6.25. To determine the Teflon optical properties, we implemented the Teramat software, and the results are shown in Figure 6.26.

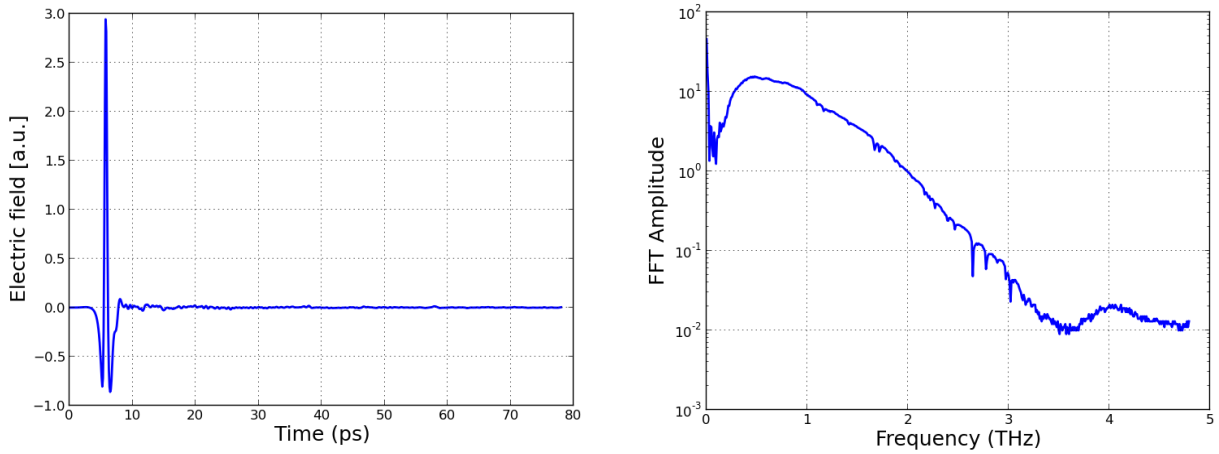

(a) (b)

Figure 6.25: (a) The electric field of the THz pulse that has passed through the Teflon sample versus time, and (b) the spectrum obtained by applying a fast Fourier transform to the electric field of the THz pulse.

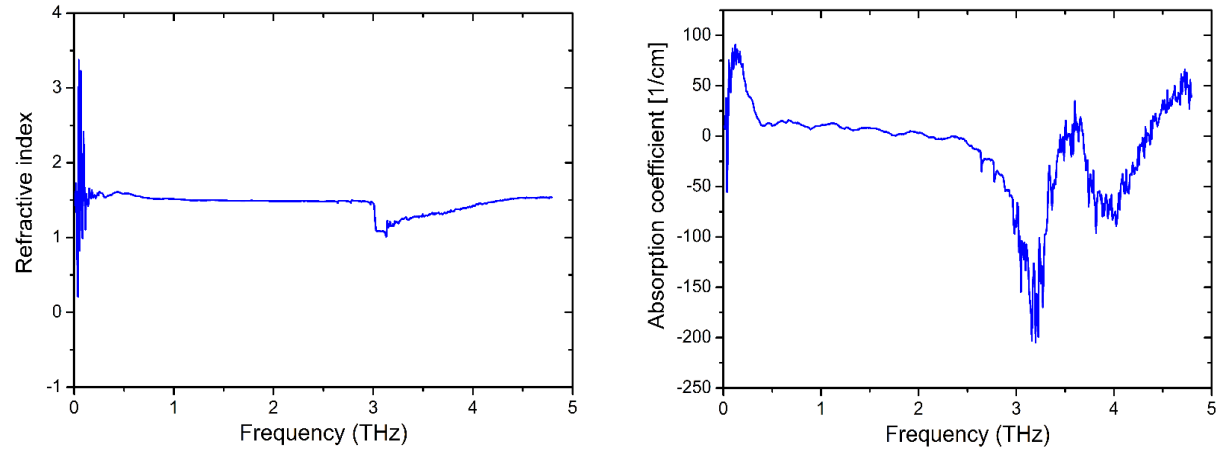

(a) (b)

Figure 6.26: (a) Refractive index of a 0.23 mm Teflon sample versus frequency, and (b) absorption coefficient of the same sample versus frequency.

For the samples considered in this section, we note that in the material parameter extraction curves at certain points in the frequency domain there are negative absorption values, and that means in this area there is just noise. The negative absorption has no physical meaning, so we will ignore the negative components of the extracted parameters. It should be noted that our system is not accurate below 0.2 THz. For all samples inspected in this section we found that their refractive indices lies between 1 and 2. To highlight our results we zoomed in between 1 and 2, for the extracted refractive index data.

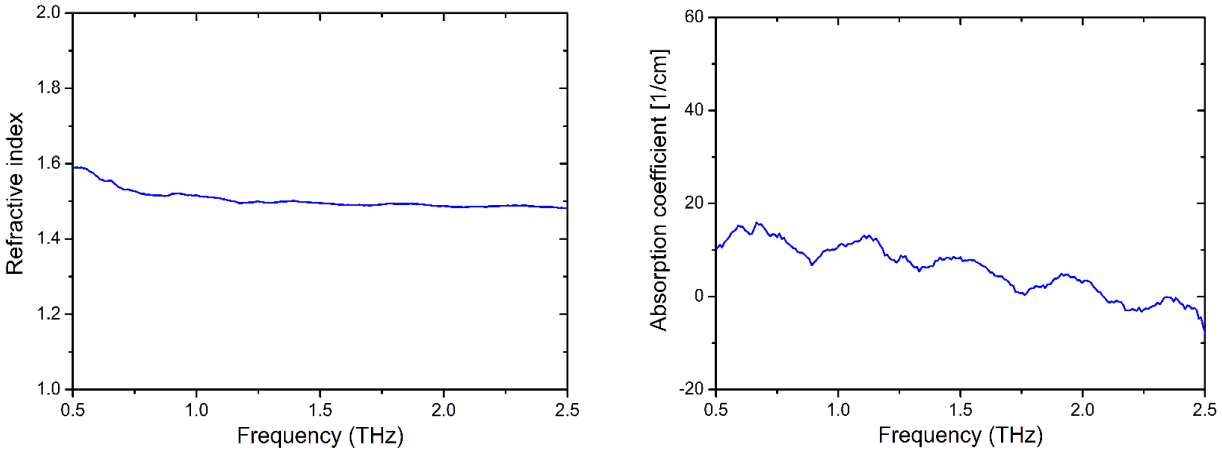

(a) (b)

Figure 6.27: (a) Zoomed in data of the refractive index of a 0.23 mm Teflon sample versus frequency obtained via the Teramat software, and (b) absorption coefficient of the same sample versus frequency obtained via the Teramat software.

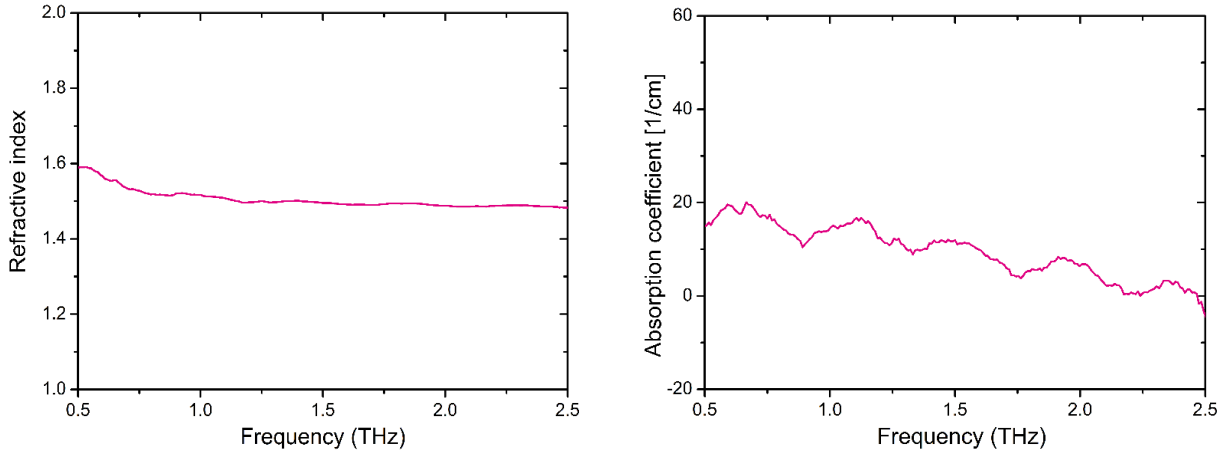

(a) (b)

Figure 6.28: (a) Refractive index of a 0.23 mm Teflon sample versus frequency obtained via Eq. 6.1.1, and (b) the absorption coefficient of same sample versus frequency obtained via Eq. 6.1.2.

Figure 6.27(a) shows the frequency dependent refractive index of a 0.23 mm Teflon sample which is calculated from the phase and amplitude information of the Fourier spectra of the pulse in the frequency range 0.5 and 2.5 THz obtained via the Teramat software. We note that the refractive index of the Teflon sample is approximately 1.5 and does not vary significantly with frequency. (b) The frequency dependent absorption coefficient of a 0.23 mm Teflon sample is also calculated from the phase and amplitude information of the Fourier spectra of the pulse in the same frequency range with the same method. Here we note that the absorption coefficient of the Teflon sample does vary with frequency. As can be seen at low frequencies the absorption is higher and starts to decrease with frequency. We also note that there are oscillations in the absorption curve. These are most likely artefacts due to Fabry Perot reflections.

Similar procedure used to obtain Figure 6.6 has also been used to obtain the results in Figure 6.28 [29].

Next we examined a 1.6 mm Polyethylene sample, for which we extracted the optical parameters. We used the same technique, that we used for the Teflon sample. The results of our experiment are depicted in Figures 6.29.

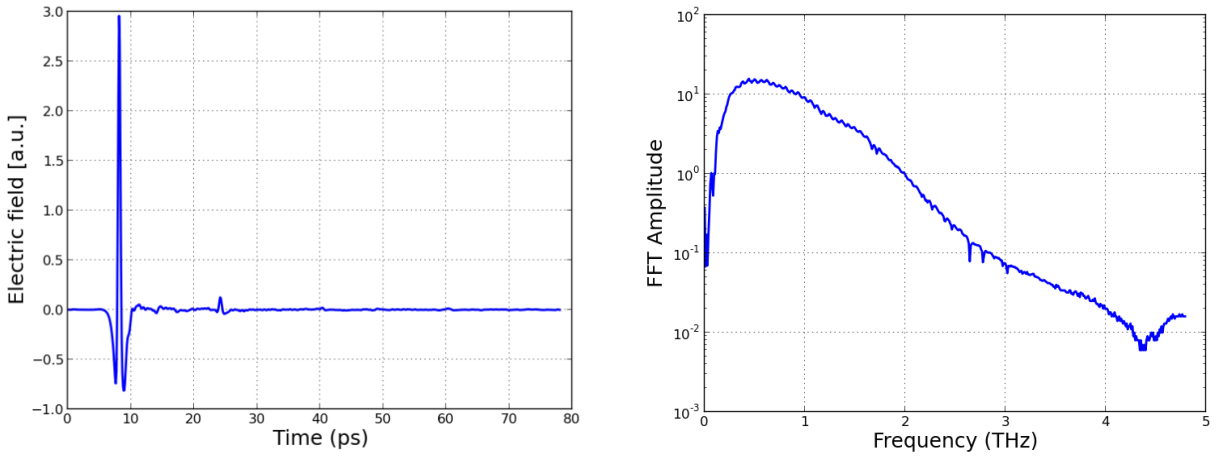

(a) (b)

Figure 6.29: (a) The electric field of the THz pulse that has passed through the Polyethylene sample versus time, and (b) the spectrum obtained by applying a fast Fourier transform to the electric field of the THz pulse.

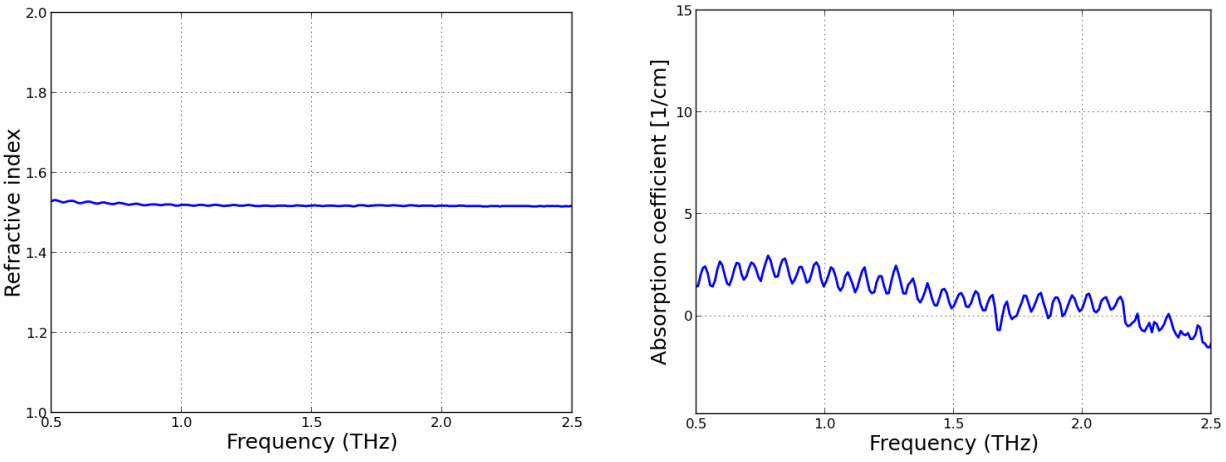

(a) (b)

Figure 6.30: (a) The refractive index of a 1.6 mm Polyethylene sample versus frequency, and (b) absorption coefficient of the same sample versus frequency.

Figure 6.30(a) shows that the frequency dependent refractive index of a 1.6 mm Polyethylene sample calculated from the phase and amplitude information of the Fourier spectra of the pulse in the frequency range 0.5 and 2.5 THz. We note that the refractive index of the Polyethylene sample is approximately 1.5 and does not vary significantly with frequency. (b) The frequency dependent absorption coefficient of the 1.6 mm Polyethylene sample is also calculated from the

phase and amplitude information of the Fourier spectra of the pulse in the same frequency range. Here we note that the absorption coefficient of the Polyethylene sample does slightly vary with frequency. We also note that there are oscillations in the absorption curve due to Fabry Perot reflections in the sample [29].

The third sample we examined was a Polypropylene which came in two variations. The first variation was clear (unstretched) and was measured to be 1.36 mm thick, and the second variation was opaque (stretched) and was measured to be 1.40 mm thick as shown in Figure 6.31. Again we used the same technique, that we used to perform the previous measurement, to extract its optical properties. Before considering our sample we first measured the electric field of the THz pulse (E_{ref}) before passing through the sample, as shown in Figure 6.32, after which we measured the pulse that passes through the sample. The results of our experiment are depicted in Figures 6.33 and 6.35.

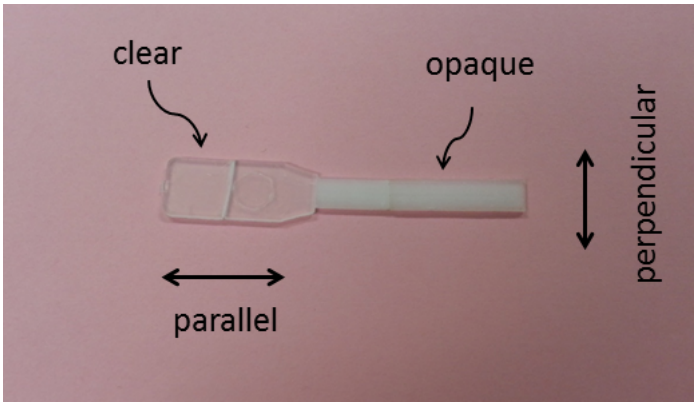

Figure 6.31: Clear and opaque Polypropylene sample with an indication of the orientation of the sample relative to the THz pulse polarization.

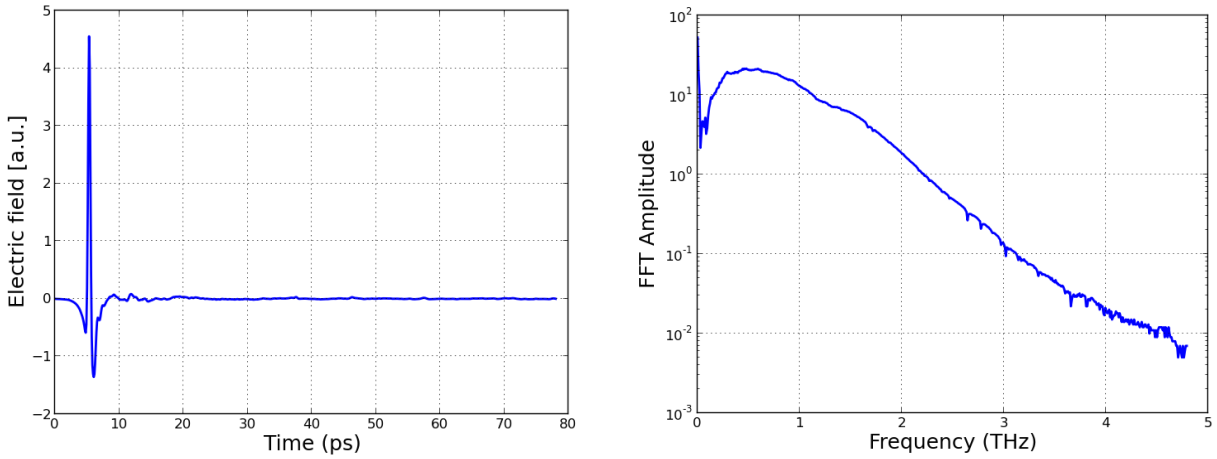

(a) (b)

Figure 6.32: (a) The electric field of the THz pulse versus time, (b) the spectrum obtained by applying a fast Fourier transform to the electric field of the THz pulse.

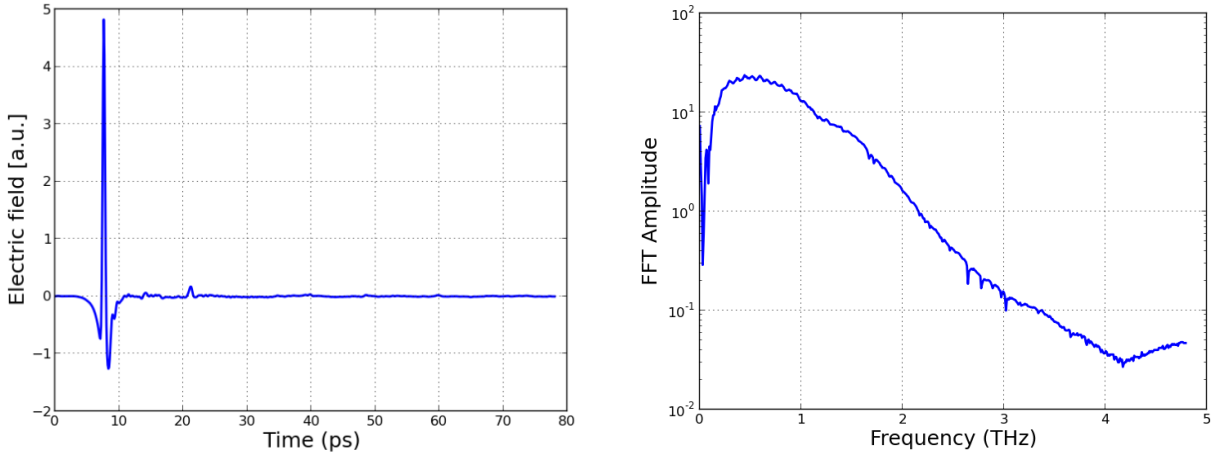

(a) (b)

Figure 6.33: (a) Transmitted electric field of the THz pulse through the clear Polypropylene sample versus time. The incident polarization was in the parallel direction. (b) The spectrum obtained by applying a fast Fourier transform to the electric field of the THz pulse.

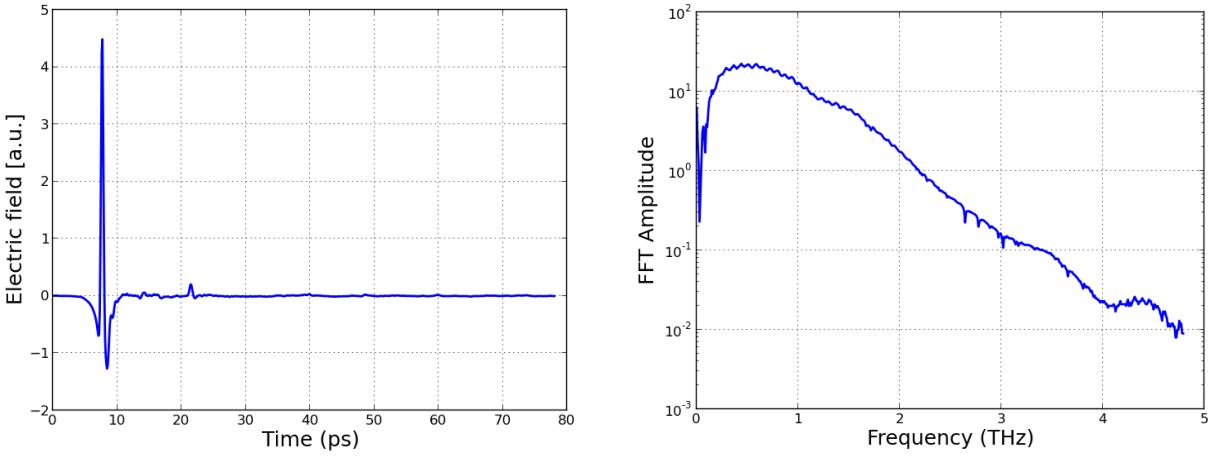

(a) (b)

Figure 6.34: (a) Transmitted electric field of the THz pulse through the clear Polypropylene sample versus time, this time polarized in the perpendicular direction. (b) The spectrum obtained by applying a fast Fourier transform to the electric field of the THz pulse.

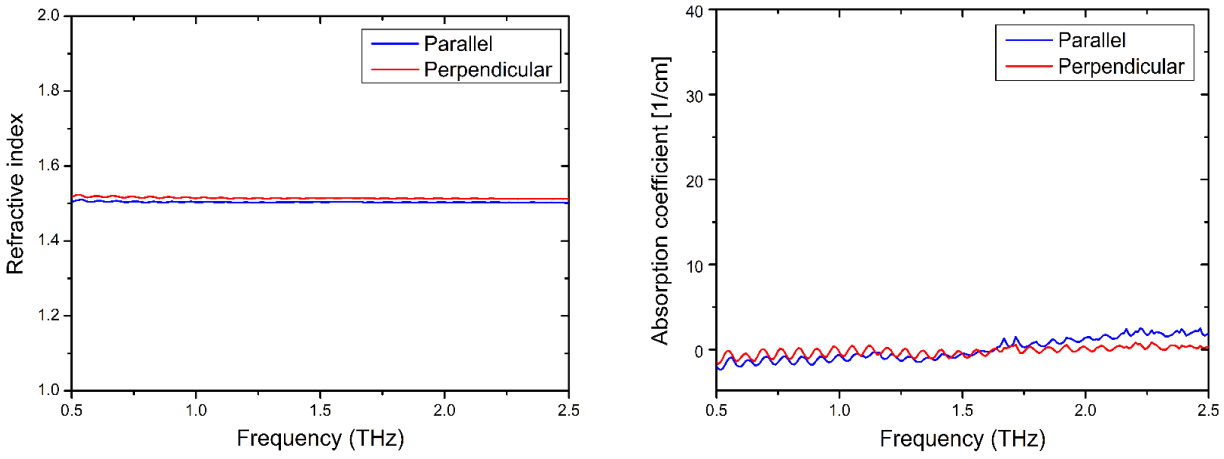

(a) (b)

Figure 6.35: (a) The combined refractive indices of a 1.36 mm clear Polypropylene sample oriented parallel and perpendicular to the THz pulse polarization, and (b) the combined absorption coefficients of the same Polypropylene sample oriented parallel and perpendicular to the THz pulse polarization.

Figure 6.35(a) shows the frequency dependent combined refractive indices of a 1.36 mm clear Polypropylene sample oriented parallel and perpendicular to the THz pulse polarization which is calculated from the phase and amplitude information of the Fourier spectra of the pulse in the frequency range 0.5 and 2.5 THz. We note that the refractive index of the clear Polypropylene sample oriented parallel and perpendicular to the THz pulse polarization is approximately 1.5 and does not vary significantly with frequency. (b) The frequency dependent combined absorption coefficients of a 1.36 mm clear Polypropylene sample oriented parallel and perpendicular to the THz pulse polarization is also calculated from the phase and amplitude information of the Fourier spectra of the pulse in the same frequency range. Here we note that the absorption coefficient of the clear Polypropylene sample oriented perpendicular to the THz pulse polarization is approximately zero, and does not vary significantly with frequency. The parallel coefficient is similar to the perpendicular one at first, but at approximately 1.5 THz there is a slight increase as the frequency increases. We also note that there are small oscillations in the absorption curve and this is due to Fabry Perot reflections [29].

These measurements were now repeated to determine whether the small differences observed are real or artefacts of the measurement.

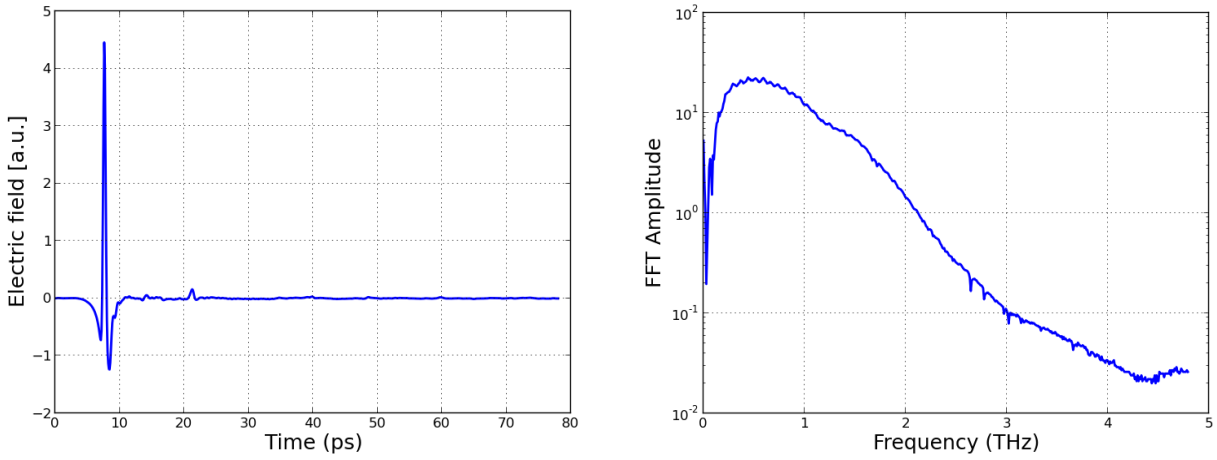

(a) (b)

Figure 6.36: Transmitted electric field of the THz pulse through the clear Polypropylene sample versus time (repeat measurement). The incident polarization was in the parallel direction. (b) The spectrum obtained by applying a fast Fourier transform to the electric field of the THz pulse.

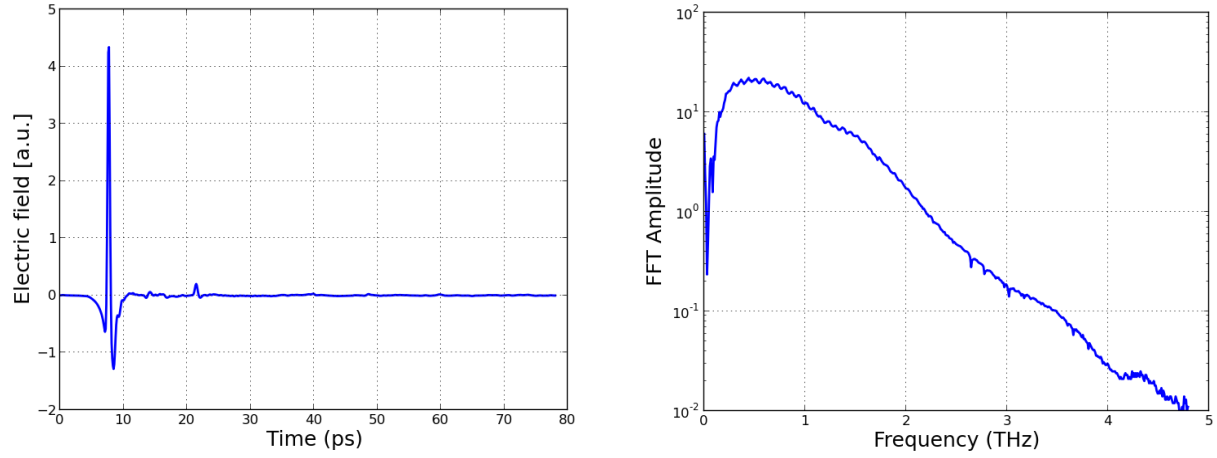

(a) (b)

Figure 6.37: Transmitted electric field of the THz pulse through the clear Polypropylene sample versus time (repeat measurement), this time polarized in the perpendicular direction. (b) The spectrum obtained by applying a fast Fourier transform to the electric field of the THz pulse.

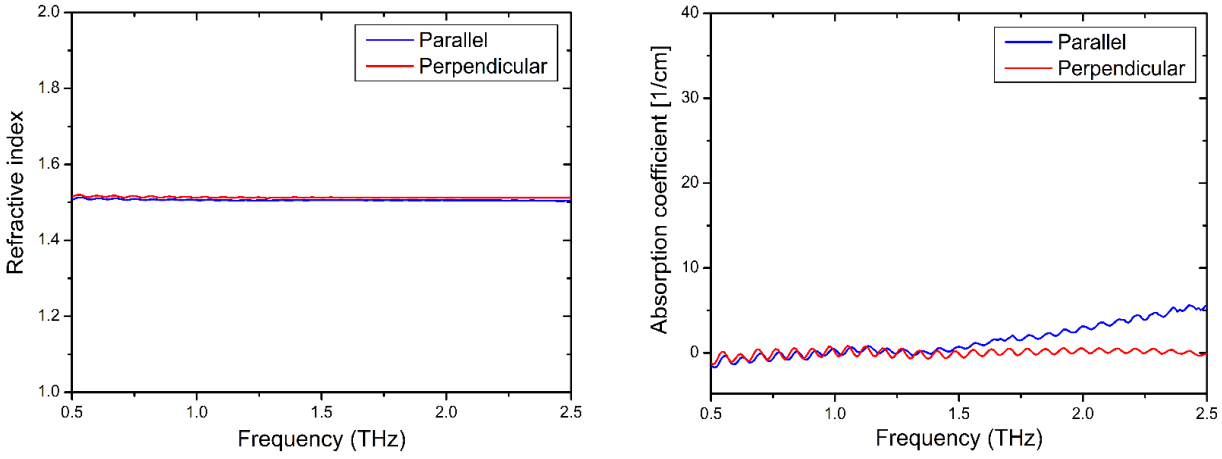

(a) (b)

Figure 6.38: (a) The combined refractive indices of a 1.36 mm clear Polypropylene sample oriented parallel and perpendicular to the THz pulse polarization (repeat measurement), and (b) the combined absorption coefficients of the same Polypropylene sample oriented parallel and perpendicular to the THz pulse polarization.

Figures 6.38(a) and 6.38(b) closely resembles Figures 6.35(a) and 6.35(b). This would confirm the slight differences observed between the parameters extracted for the parallel and perpendicular orientations are real and reproducible. These small difference in the refractive indices will be investigated further after we have performed similar measurements on the opaque Polypropylene sample. At frequencies above 1.5 THz the absorption coefficient of the parallel orientated sample seem to increase compared to the perpendicular sample. The reason for this is unclear and will not be gassed at.

The second part of the Polypropylene sample is slightly opaque, because it was stretched, and had a thickness of 1.40 mm. We again used the same technique as previously to perform the measurement and extract its optical properties. The results of our experiment are depicted in Figures 6.39, 6.40 and 6.41.

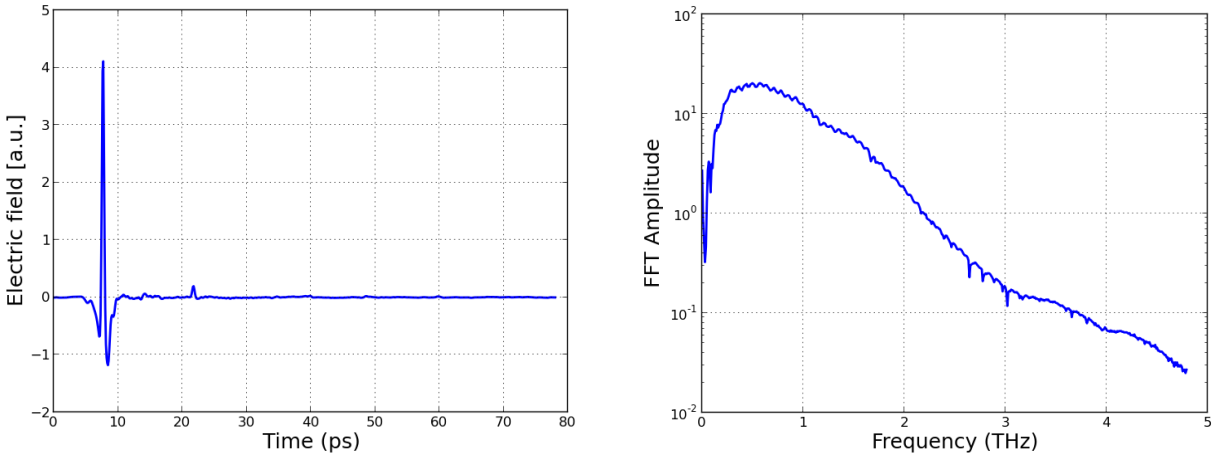

(a) (b)

Figure 6.39: (a) Transmitted electric field of the THz pulse through the opaque Polypropylene sample versus time. The incident polarization was in the parallel direction. (b) The spectrum obtained by applying a fast Fourier transform to the electric field of the THz pulse.

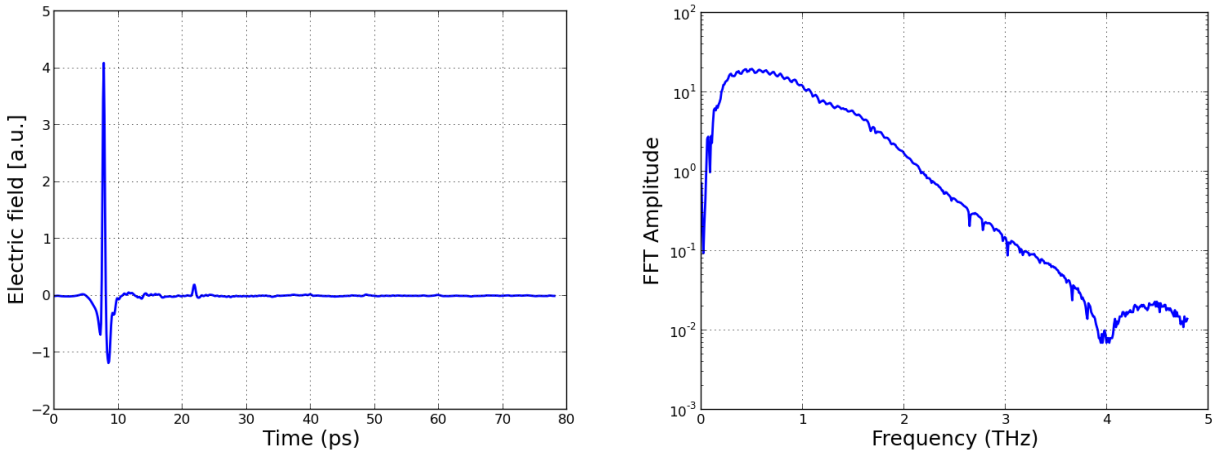

(a) (b)

Figure 6.40: (a) Transmitted electric field of the THz pulse through the opaque Polypropylene sample versus time, this time polarized in the perpendicular direction. (b) The spectrum obtained by applying a fast Fourier transform to the electric field of the THz pulse.

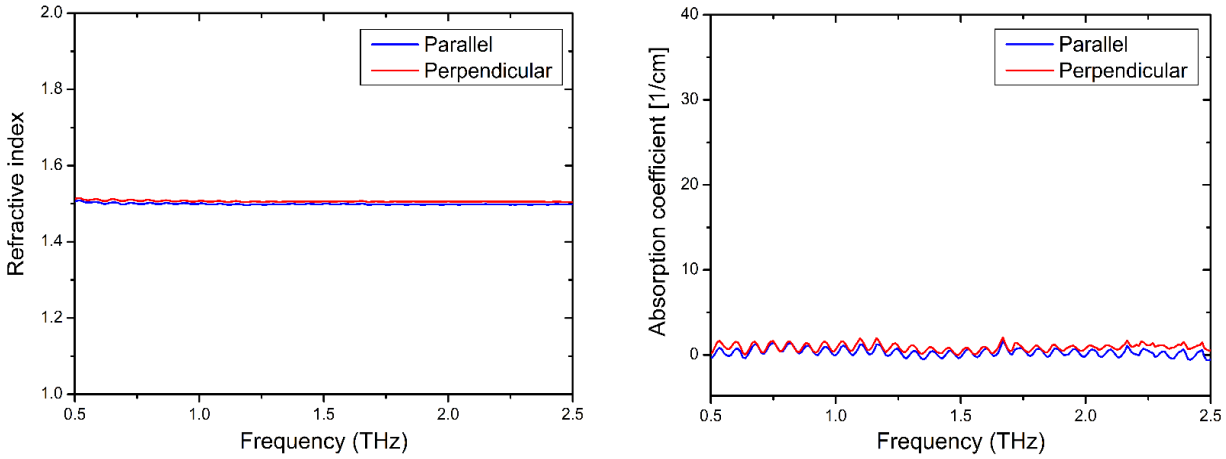

(a) (b)

Figure 6.41: (a) The combined refractive indices of a 1.40 mm opaque Polypropylene sample oriented parallel and perpendicular to the THz pulse polarization, and (b) the combined absorption coefficients of the same Polypropylene sample oriented parallel and perpendicular to the THz pulse polarization.

Figure 6.41(a) shows the frequency dependent refractive index of a 1.40 mm opaque Polypropylene sample oriented parallel and perpendicular to the THz pulse polarization in the frequency range 0.5 and 2.5 THz. We note that the refractive index of the opaque Polypropylene sample oriented parallel and perpendicular to the THz pulse polarization is approximately 1.5 and does not vary significantly with frequency, and (b) shows the frequency dependent absorption coefficients of the same Polypropylene sample oriented parallel and perpendicular with the THz pulse polarization in the same frequency range. Here we note that the absorption coefficients of the opaque Polypropylene sample oriented parallel and perpendicular to the THz pulse polarization is approximately zero, and does not vary significantly with frequency. We also note that there are oscillations in the absorption spectrum that are due to Fabry Perot reflections [29].

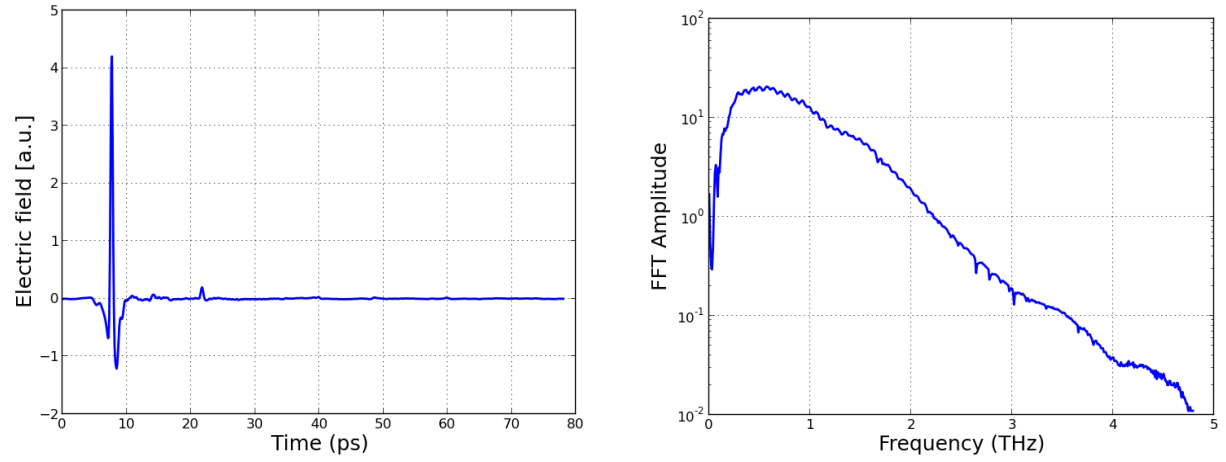

(a) (b)

Figure 6.42: Transmitted electric field of the THz pulse polarized parallel to the opaque Polypropylene sample versus time (repeat measurement), and (b) the spectrum obtained by applying a fast Fourier transform to the electric field of the THz pulse.

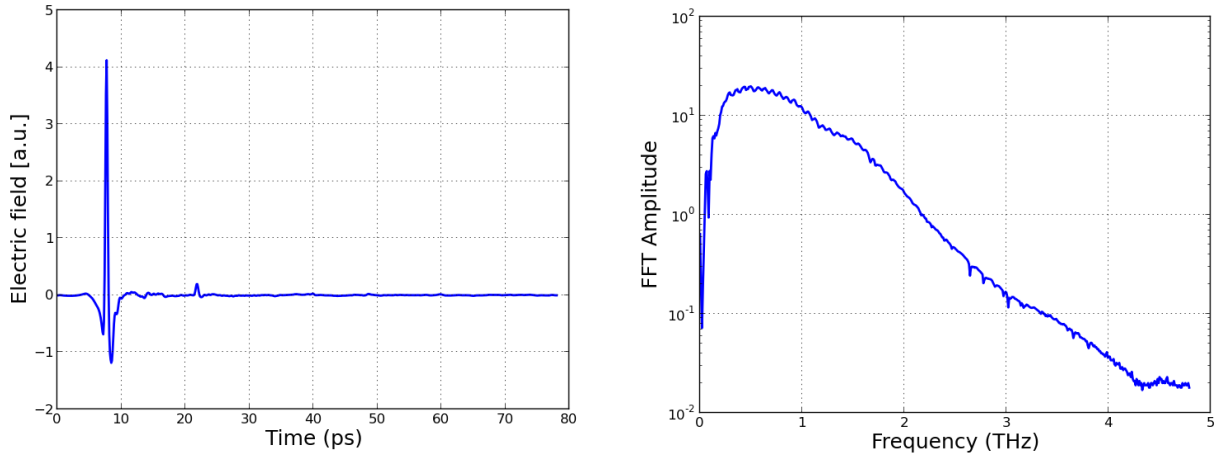

(a) (b)

Figure 6.43: Transmitted electric field of the THz pulse polarized perpendicular to the opaque Polypropylene sample versus time (repeat measurement), and (b) the spectrum obtained by applying fast Fourier transform to the electric field of the THz pulse.

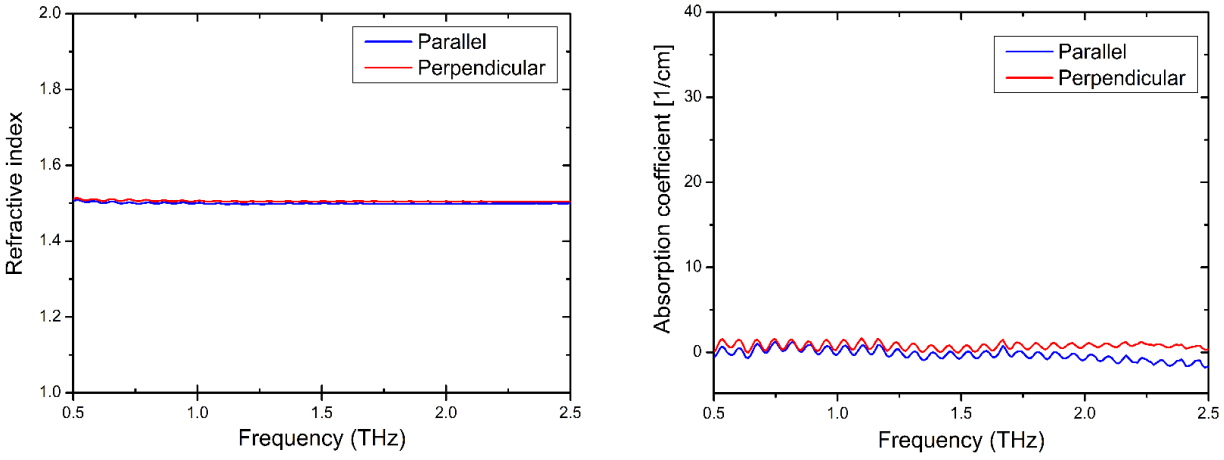

(a) (b)

Figure 6.44: (a) The combined refractive indices of a 1.40 mm opaque Polypropylene sample oriented parallel and perpendicular to the THz pulse polarization (repeat measurement), and (b) the combined absorption coefficients of the same Polypropylene sample oriented parallel and perpendicular to the THz pulse polarization.

Figures 6.44(a) and 6.44(b) closely resembles Figures 6.41(a) and 6.41(b). This again confirm the reproducibility of the results. These results, along with those obtained in Figures 6.38(a) and 6.38(b) and Figures 6.35(a) and 6.35(b), will now be looked at in more detail.

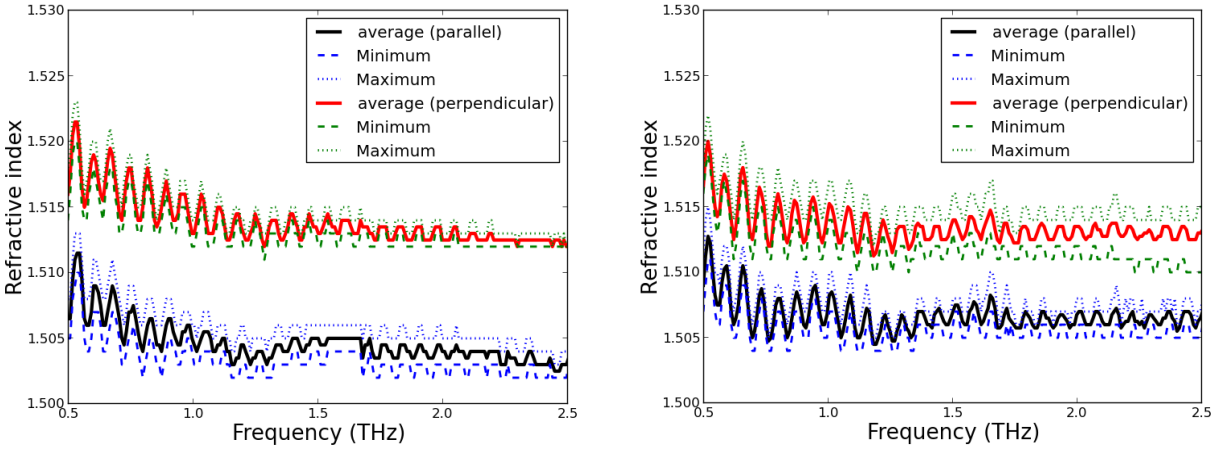

(a) (b)

Figure 6.45: (a) Average value calculated for the refractive index of 1.36 mm clear Polypropylene sample oriented parallel and perpendicular to the THz pulse polarization, and (b) average value calculated for the refractive index of 1.40 mm opaque Polypropylene oriented parallel and perpendicular to the THz pulse polarization.

In Figure 6.45, we calculated the errorbars between the refractive index of 1.36 mm and 1.40 mm clear and opaque Polypropylene sample oriented parallel and perpendicular to the THz pulse polarization. From Figures 6.45(a) and 6.45(b) we can see that the differences in refractive indices between the parallel and perpendicular orientations are small for both the clear and opaque Polypropylene samples. The differences are slightly larger for the clear sample.

This is contrary to what was expected since it was assumed that the sample would become more birefringent as it was stretched. The opposite occurred, indicating that the pre-existing order of the molecules was partially destroyed during the stretching process.

Now we investigate the oscillations in the material parameter extraction results. We took measurement with different temporal steps sizes (0.208 ps, 0.104 ps, 0.052 ps, 0.010 ps, and 0.005 ps) in order to see if the oscillations are due to sampling frequency. The results are shown in figure 6.46.

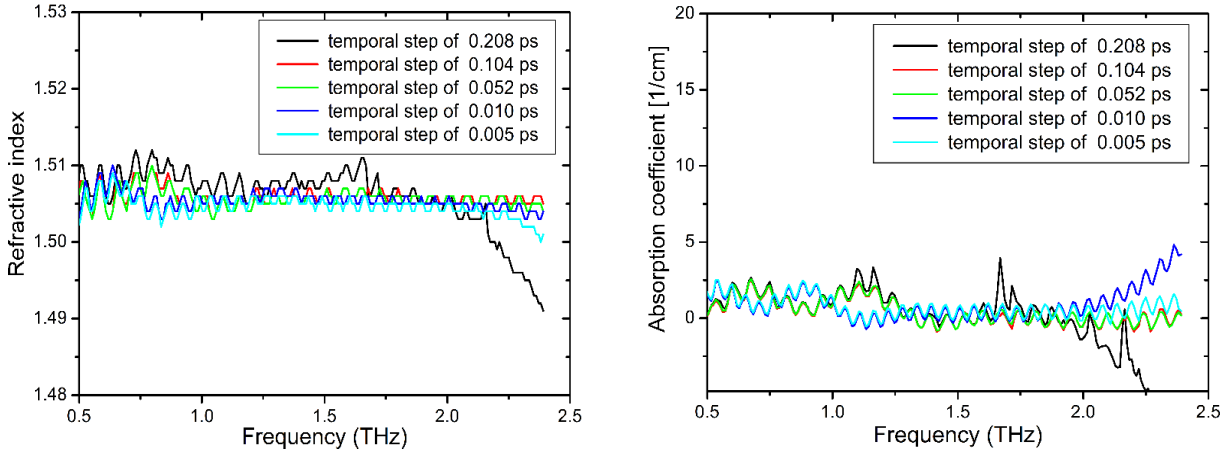

(a) (b)

Figure 6.46: (a) Refractive index of a 1.40 mm opaque Polypropylene sample measured at different temporal steps 0.208 ps, 0.104 ps, 0.052 ps, 0.010 ps, and 0.005 ps, and (b) the absorption coefficient of the same sample measured at the same intervals.

Figure 6.46 shows (a) the frequency dependent refractive index of a 1.40 mm opaque Polypropylene sample measured with different temporal steps of (0.208 ps, 0.104 ps, 0.052 ps, 0.010 ps, and 0.005 ps) [29]. We note that the oscillation in the refractive index is large at low frequencies and decreases at higher frequencies. This occurs for all temporal steps. We also note that at large temporal steps, for example (0.208 ps), the signal decreases at high frequencies. This is due to the fact that we can not resolve high frequencies with large temporal steps. Figure 6.46(b) shows the frequency dependent absorption coefficient of the 1.40 mm opaque Polypropylene sample measured at the same temporal steps. The results are similar to (a).

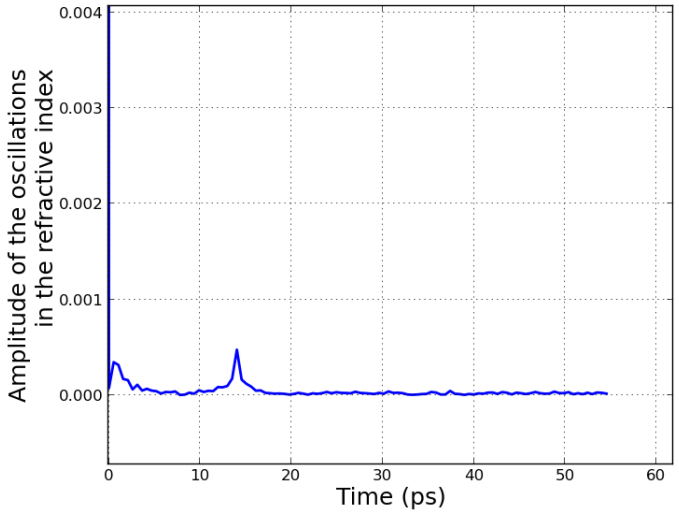

Figure 6.47: Amplitude of the oscillation in the refractive index of the 1.40 mm opaque Polypropylene sample versus time.

We applied a fast Fourier transform to transform the signal from Figure 6.46(a) from the frequency domain to the time domain. The result is shown in Figure 6.47. The purpose of transforming the signal from frequency domain to time domain is to check if the oscillation in our results is from the internal reflections, i.e. sample thickness. We observe a peak at 14.18 ps. Next we calculate the expected period of the pulses using the following equation

$$T = \frac{2\,n\,d}{c},$$

where n is the refractive index of the sample, d is the sample thickness, and c is the speed of light in vacuum.

The above parameters as obtained from the calculations, are $n = 1.505$, $d = 1.40$ mm, and $c = 3 \times 10^8$ m/s. This yields, $T = 14.046$ ps, which is approximately the same as the observed period of the oscillation. This shows that the oscillations in the results are related to the sample thickness which is consistent with the work of W. Withayachumnankul et al. in [48] and Pupeza et al. in [30].

6.5 Investigating thermoplastic polymer properties

In this section we wish to investigate the properties of thermoplastic polymer samples. For the measurement of the refractive indices and absorption coefficients of the thermoplastic polymers, we first measured the electric field of the THz pulse E_{ref} before passing through the samples, as shown in Figure 6.48, after which we measured it after passing through the samples.

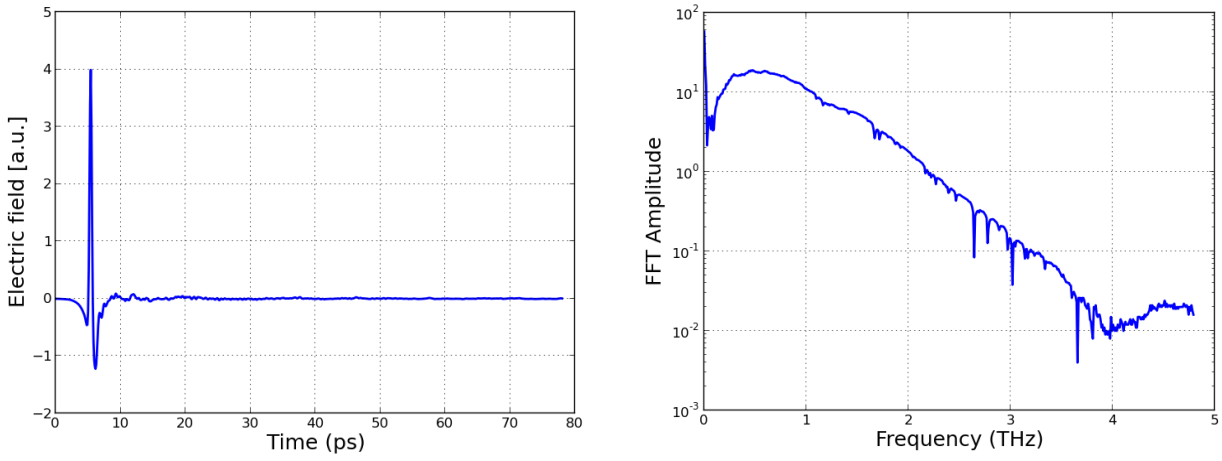

(a) (b)

Figure 6.48: (a) The electric field of the THz pulse versus time, and (b) the spectrum obtained by applying a fast Fourier transform to the electric field of the THz pulse, with an empty sample chamber.

The first sample considered in this section was Acrylonitrile Butadiene Styrene (ABS), with a thickness of 1.48 mm. The same techniques that were used previously are again implemented. The results of our experiment are depicted in Figure 6.49. To determine the optical properties of the ABS sample we implemented the Teramat software, and the results are shown in Figure 6.50.

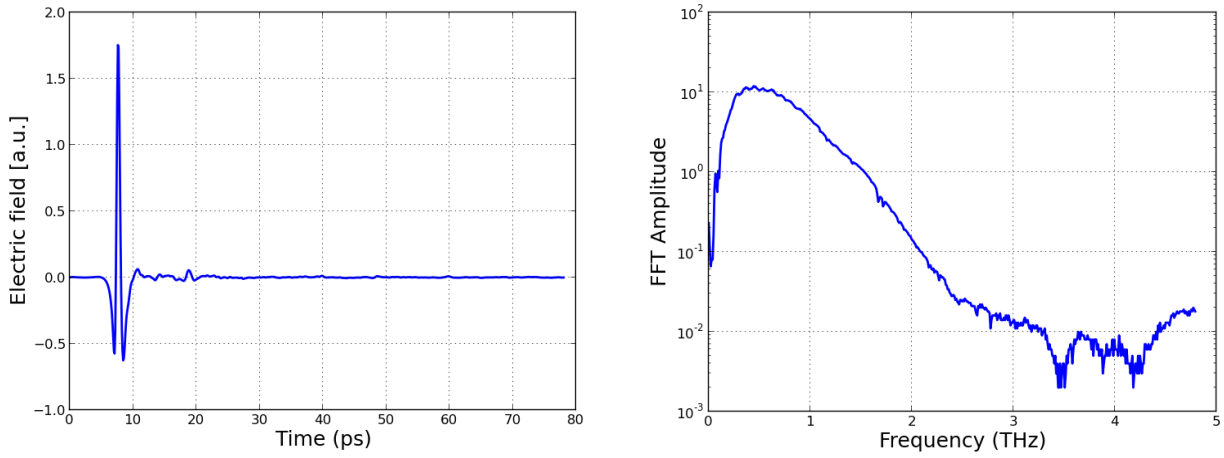

(a) (b)

Figure 6.49: (a) The electric field of the THz pulse after passing through Acrylonitrile Butadiene Styrene (ABS) sample versus time, and (b) the spectrum obtained by applying a fast Fourier transform to the electric field of the THz pulse.

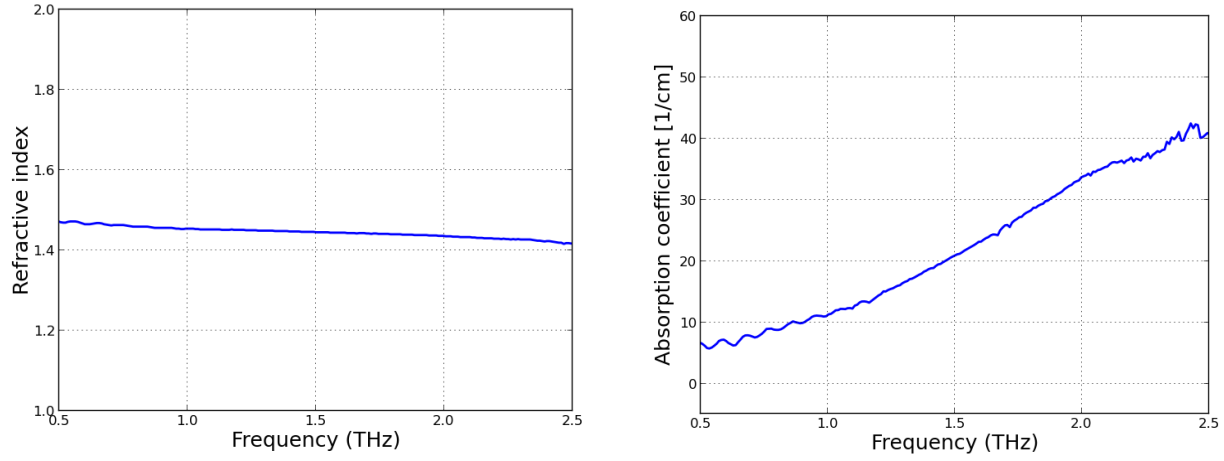

(a) (b)

Figure 6.50: (a) Refractive index of a 1.48 mm Acrylonitrile Butadiene Styrene (ABS) sample versus frequency, and (b) the absorption coefficient of the same (ABS) sample versus frequency.

Figure 6.50(a) shows the frequency dependent refractive index of a 1.48 mm Acrylonitrile Butadiene Styrene (ABS) sample in the frequency range 0.5 and 2.5 THz. We note that the refractive index of the ABS sample slightly declines between 0.5 and 2.0 THz, and (b) shows the frequency dependent absorption coefficient of the ABS sample in the same frequency range. Here we note that the absorption coefficient of the ABS sample does vary with frequency. As can be seen at low frequencies the absorption is low and starts to increase with frequency.

The second sample considered in this section was Polyphenylene Oxide (PPO), for which we had two samples of different thickness (0.72 mm and 2.53 mm). Again we used the same technique that we used for the first sample. In Figures 6.51 and 6.52 we depict the measurements for the 0.72 mm PPO sample.

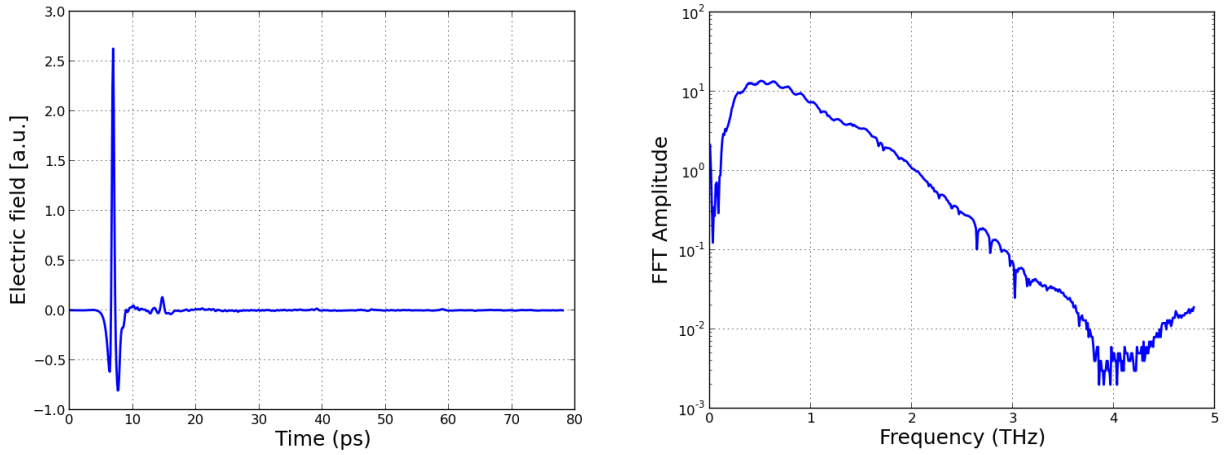

(a) (b)

Figure 6.51: (a) The electric field of the THz pulse after passing through the 0.72 mm Polyphenylene Oxide (PPO) sample versus time, and (b) the spectrum obtained by applying a fast Fourier transform to the electric field of the THz pulse.

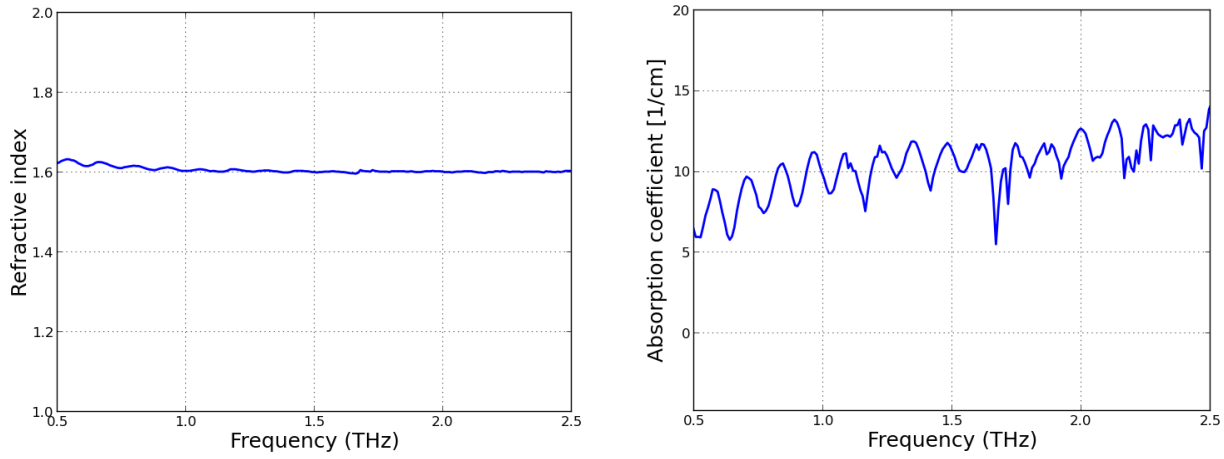

(a) (b)

Figure 6.52: (a) Refractive index of a 0.72 mm PPO sample versus frequency, and (b) the absorption coefficient of the same sample versus frequency.

Figure 6.52(a) shows the frequency dependent refractive index of a 0.72 mm Polyphenylene Oxide (PPO) sample in the frequency range 0.5 and 2.5 THz. We note that the refractive index of the PPO sample is approximately 1.6 and does not vary significantly with frequency, and (b) shows the frequency dependent absorption coefficient of the same sample. Here we note that the absorption coefficient of the PPO sample does vary with frequency. As can be seen at low frequencies the absorption is low and increases with frequency. We also note that there are oscillations in the absorption curve that are due to Fabry Perot reflections. At approximately 1.6 THz, there is a sharp decrease in the absorption spectrum of the sample [29].

In Figures 6.53 and 6.54 we depict the measurements of the 2.53 mm PPO sample.

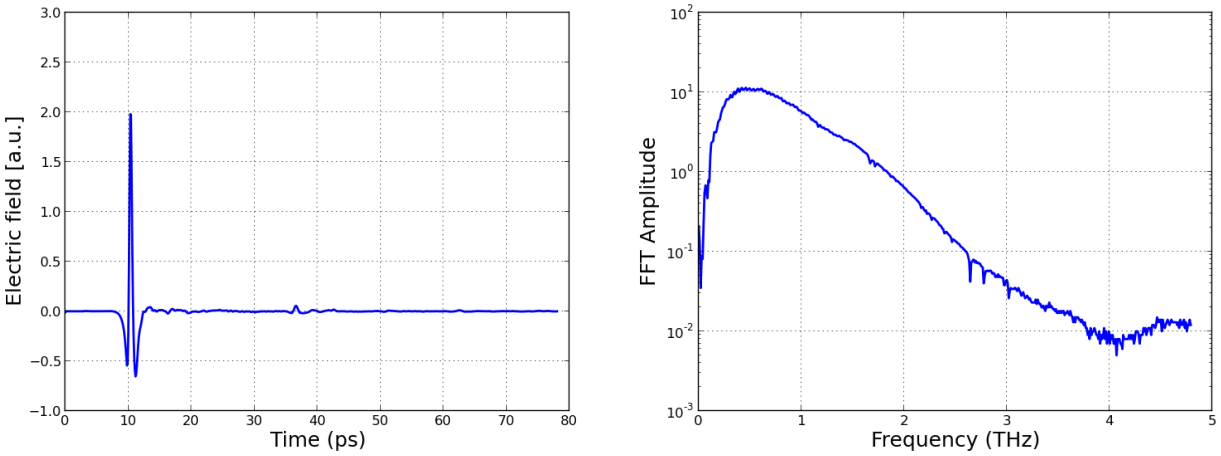

(a) (b)

Figure 6.53: (a) The electric field of the THz pulse after passing through the 2.53 mm Polyphenylene Oxide (PPO) sample versus time, and (b) the spectrum obtained by applying a fast Fourier transform to the electric field of the THz pulse.

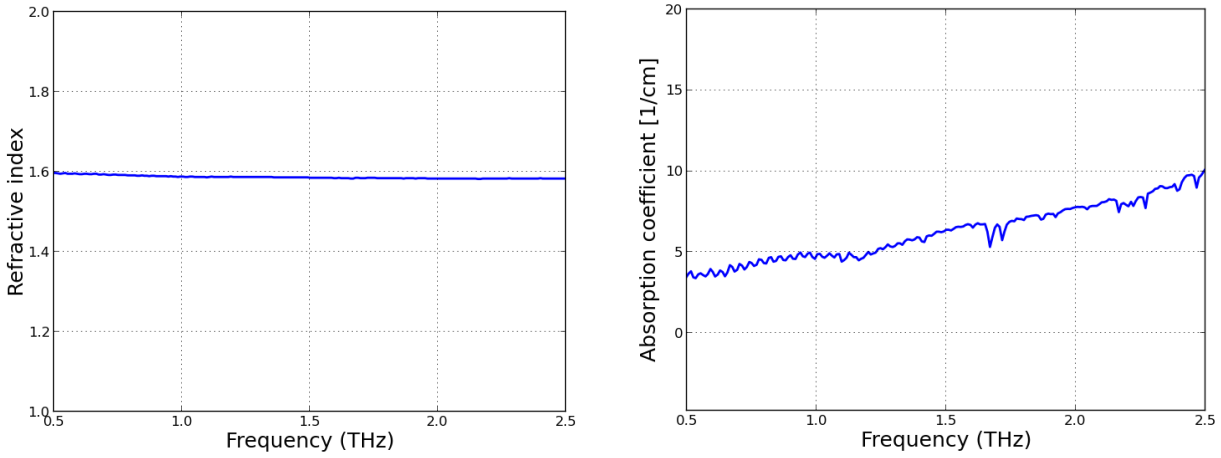

(a) (b)

Figure 6.54: (a) Refractive index of a 2.53 mm PPO sample versus frequency, and (b) the absorption coefficient the same sample.

Figure 6.54(a) shows the frequency dependent refractive index of a 2.53 mm Polyphenylene Oxide (PPO) sample in the frequency range 0.5 and 2.5 THz. We note that the refractive index of the PPO sample is approximately 1.6 and does not vary significantly with frequency, and (b) shows the absorption coefficient of the same sample. Here we note that the absorption coefficient of the PPO sample does vary with frequency. As can be seen at low frequencies the absorption is low and starts to increase with frequency. We again note the slight oscillations in the absorption curve that are due to Fabry Perot reflections. Again at 1.6 THz, there is a sharp decrease in the absorption spectrum of the sample [29].

The third sample considered in this section was Polyethylene doped with metal ions, of which we had two samples of thickness 0.8 mm and 2.58 mm. We again used the same technique as

we used for the previous samples. In Figures 6.55 and 6.56 we depict the measurements for the 0.8 mm sample.

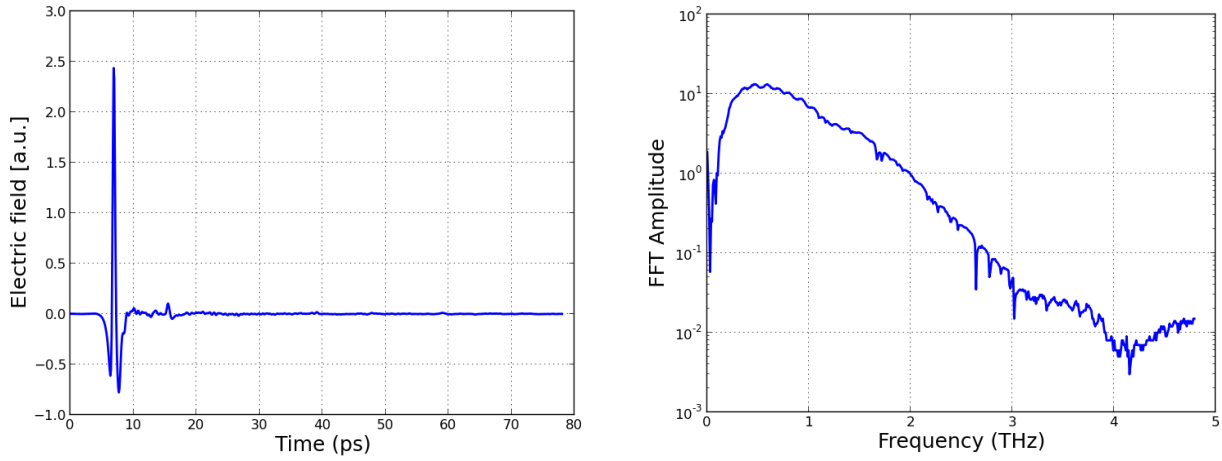

(a) (b)

Figure 6.55: (a) The electric field of the THz pulse after passing through 0.8 mm doped Polyethylene sample versus time, and (b) the spectrum obtained by applying a fast Fourier transform to the electric field of the THz pulse.

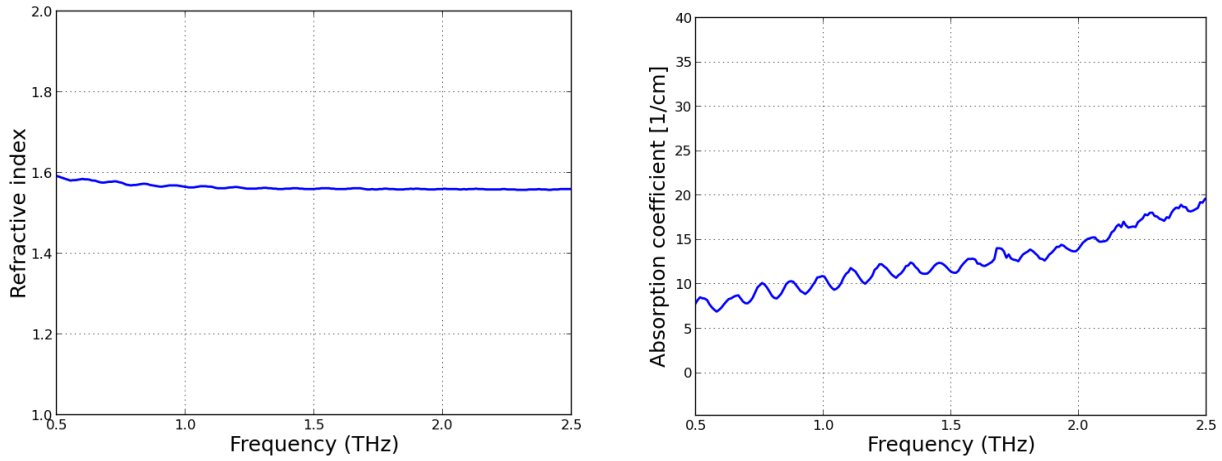

(a) (b)

Figure 6.56: (a) Refractive index of the 0.8 mm doped Polyethylene sample versus frequency, and (b) the absorption coefficient of the same sample versus frequency.

Figure 6.56(a) shows the frequency dependent refractive index of the 0.8 mm doped Polyethylene sample in the frequency range 0.5 and 2.5 THz. We note that the refractive index of the doped Polyethylene sample is approximately 1.58 and does not vary significantly with frequency, and (b) shows the frequency dependent absorption coefficient of the same sample. Here we note that the absorption coefficient of the doped Polyethylene sample does vary with frequency. As can be seen at low frequencies the absorption is low and increases with frequency. We also note the oscillations in the absorption curve that are due to Fabry Perot reflections.

In Figures 6.57 and 6.58 we depict the measurements of the 2.58 mm sample.

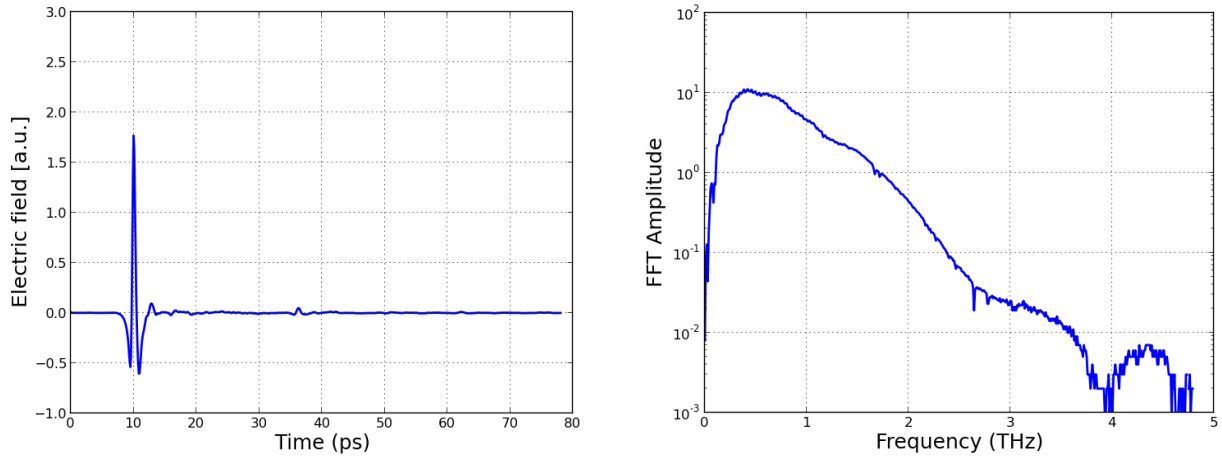

(a) (b)

Figure 6.57: (a) The electric field of the THz pulse after passing through the 2.58 mm doped Polyethylene sample versus time, and (b) the spectrum obtained by applying a fast Fourier transform to the electric field of the THz pulse.

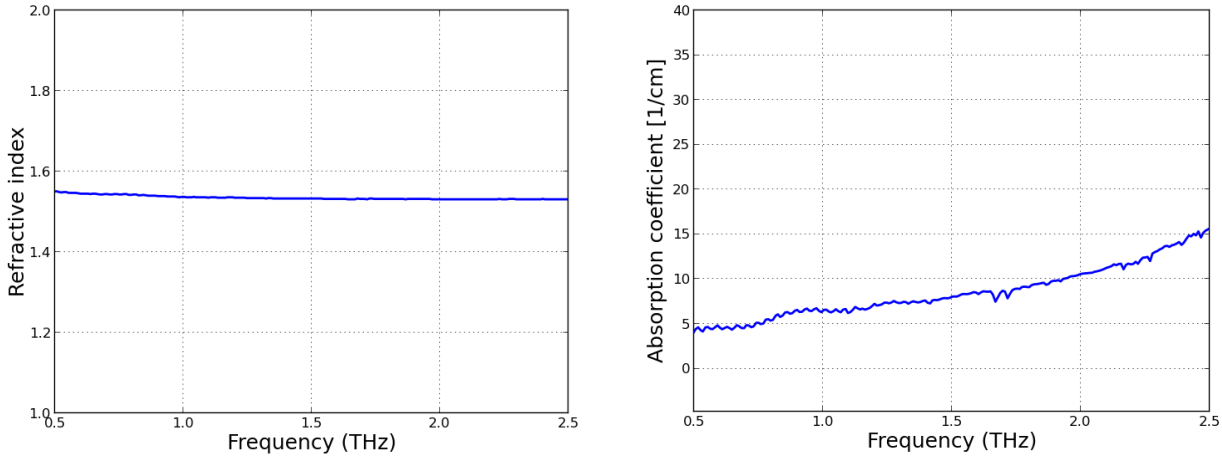

(a) (b)

Figure 6.58: (a) Refractive index of the 2.58 mm doped Polyethylene sample versus frequency, and (b) the absorption coefficient of the same sample versus frequency.

Figure 6.58(a) shows the frequency dependent refractive index of a 2.58 mm doped Polyethylene sample in the frequency range 0.5 and 2.5 THz. We note that the refractive index of the doped Polyethylene sample is approximately 1.55 and does not vary significantly with frequency, and (b) shows the frequency dependent absorption coefficient of the same sample. Here we note that the absorption coefficient of the doped Polyethylene sample does vary with frequency. As can be seen at low frequencies the absorption is lower and starts to increase with frequency. We also note the slight oscillations in the absorption curve that are due to Fabry Perot reflections. As can be seen at roughly 1.6 THz, there is a decrease in the absorption spectrum of the sample [29].

The fourth sample considered in this section was Polysulfone, for which we had two samples of thickness 0.73 mm and 2.54 mm. We again used the same technique that we used for the first sample. In Figures 6.59 and 6.60 we depict the measurements for the 0.73 mm sample.

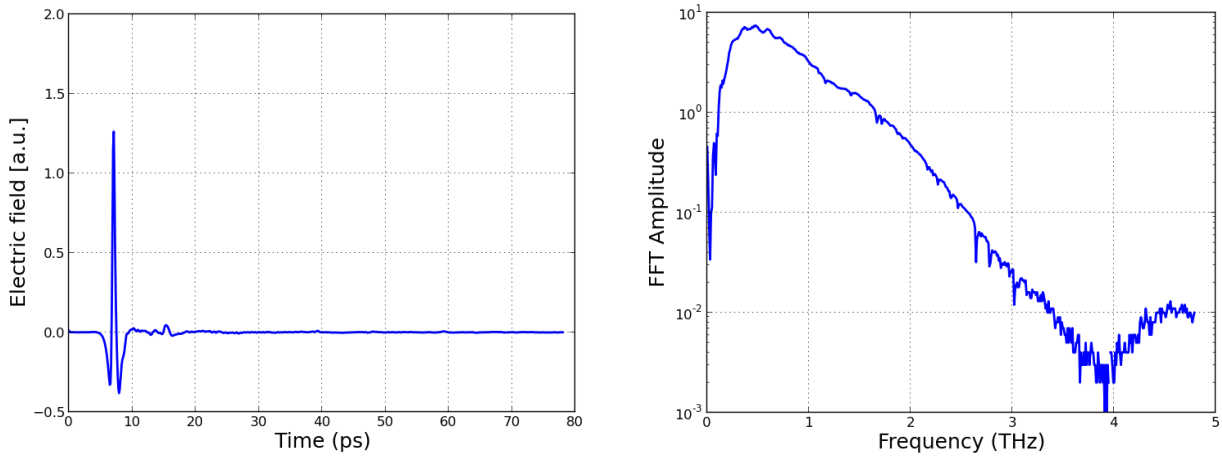

(a) (b)

Figure 6.59: (a) The electric field of the THz pulse after passing through the 0.73 mm Polysulfone sample versus time, and (b) the spectrum obtained by applying a fast Fourier transform to the electric field of the THz pulse.

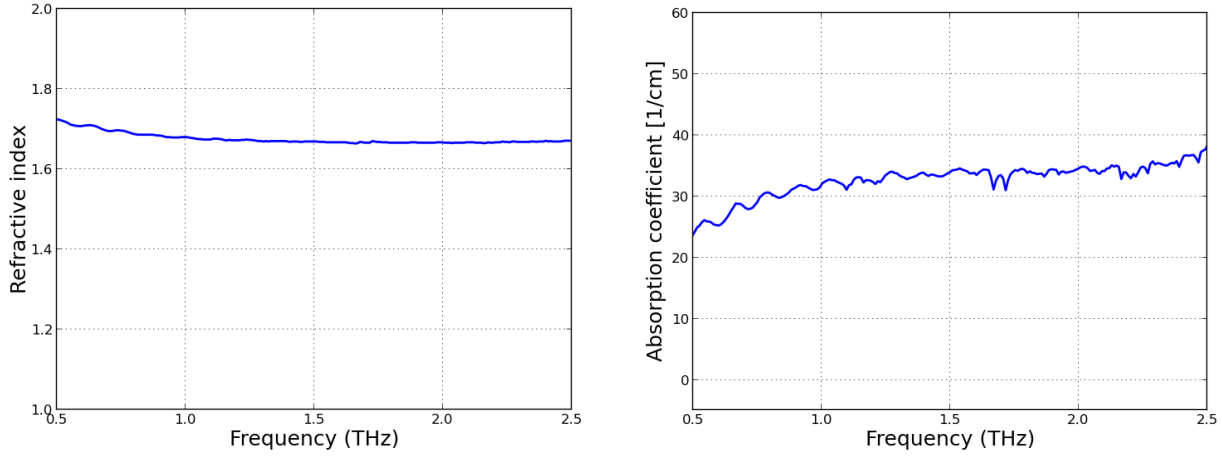

(a) (b)

Figure 6.60: (a) Refractive index of a 0.73 mm Polysulfone sample versus frequency, and (b) the absorption coefficient of the same sample.

Figure 6.60(a) shows the frequency dependent refractive index of a 0.73 mm Polysulfone sample in the frequency range 0.5 and 2.5 THz. We note that the refractive index of the Polysulfone sample shows a slight decline between 0.5 and 1.5 THz and then it becomes constant at about 1.65 THz, and (b) shows the frequency dependent absorption coefficient of the same sample. Here we note that the absorption coefficient of the Polysulfone sample does vary with frequency. As can be seen at low frequencies the absorption is lower and starts to increase with frequency. We also note that there are slight oscillations in the absorption curve that are due to Fabry Perot

reflections. As can be seen at roughly 1.6 THz, there is a decrease in the absorption spectrum of the sample [29].

In Figures 6.61 and 6.62 we depict the measurements of the 2.54 mm sample.

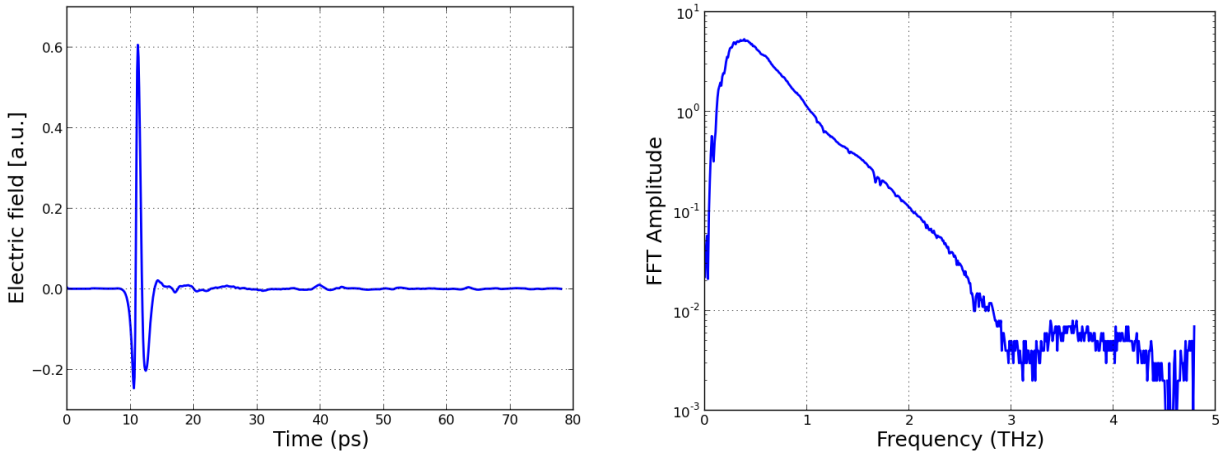

(a) (b)

Figure 6.61: (a) The electric field of the THz pulse after passing through the 2.54 mm Polysulfone sample versus time, and (b) the spectrum obtained by applying a fast Fourier transform to the electric field of the THz pulse.

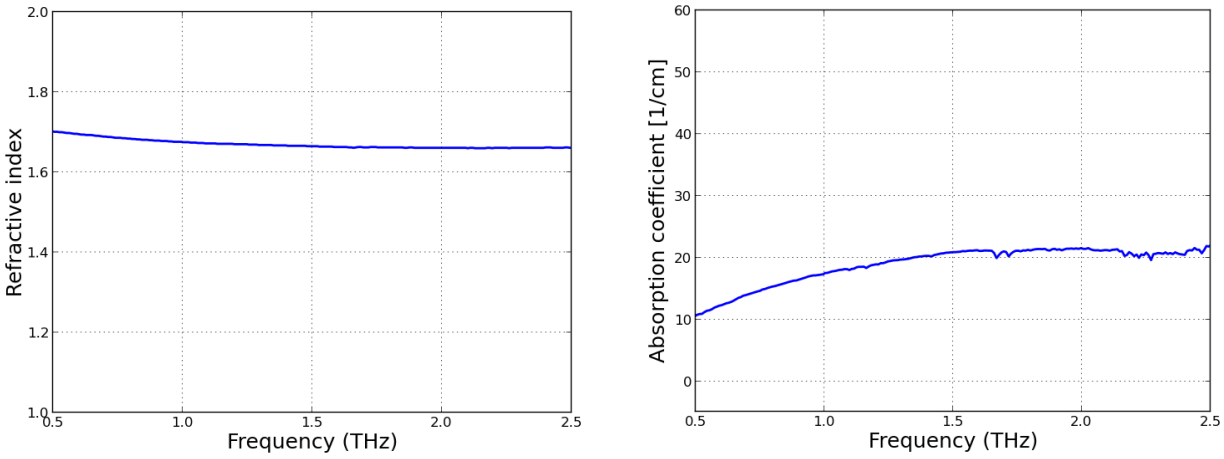

(a) (b)

Figure 6.62: (a) Refractive index of a 2.54 mm Polysulfone sample versus frequency, and (b) the absorption coefficient of the same sample versus frequency.

Figure 6.62(a) shows the frequency dependent refractive index of a 2.54 mm Polysulfone sample in the frequency range 0.5 and 2.5 THz. We note that the refractive index of the Polysulfone sample again shows a slight decline between 0.5 and 1.5 THz and then becomes constant at about 1.65 THz, and (b) shows the frequency dependent absorption coefficient of the same sample. Here we note that the absorption coefficient of the Polysulfone sample does vary with frequency. As can be seen at low frequencies the absorption is lower and starts to increase with

frequency. Again at a roughly 1.6 THz, there is a decrease in the absorption spectrum of the sample [29].

We were able to accurately extract the refractive indices and absorption coefficients for a number of different plastics. The dip in absorption spectrum observed in all the results at 1.6 THz is an artefact due to water absorption. When the measurement with the sample in place is performed, more water vapour has been removed than was the case for the reference measurement. This appears as a decrease in absorption.

In Table 6.8 we summarized the comparison between the method (Teramat software as discussed in section 6.4) used for computing the refractive indices of Silicon and Sapphire samples in the THz region and the literature values.

Material	Literature	Method (Teramat software)
Teflon	$n \simeq 1.46$ [4]	$n \simeq 1.49$
Polypropylene	$n \simeq 1.49$ [16]	$n \simeq 1.50$
Polyethylene	$n \simeq 1.52$ [20]	$n \simeq 1.53$
Polysulfone	$n \simeq 1.59$ [1]	$n \simeq 1.62$
ABS	$n \simeq 1.60$ [16]	$n \simeq 1.41$

Table 6.8: Comparison between literature and the method (Teramat software) used in obtaining the refractive indices .

Chapter 7

Conclusion

In this thesis, the characterization and determination of the refractive indices and absorption coefficients of dielectric materials in the terahertz region were investigated. THz radiation is electromagnetic (EM) radiation and we describe it using Maxwell's equations. Using the derived wave equation we can describe propagation of THz radiation in both vacuum and dielectric media.

We then studied the general background of the current oscillation in a series RLC circuit used in the THz spectroscopy system. We simulated the current in a series RLC circuit to show the behaviour of how it changes for various types of damping, namely critically damped, under damped and over damped. The emitted electric field of the THz waves is directly proportional to the time derivative of the current. We described the concept of the photoconductive antenna (PC) as used for the generation as well as detection of THz pulses. We showed that the THz electric field is proportional to the time derivative of the photocurrent induced by the incident femtosecond laser pulse on the PC antenna gap. We highlighted some photoconductive materials that are used for PC antennas. However, for the generation and detection of THz pulses with a PC antenna, low temperature grown gallium arsenide (LT-GaAs) is the standard material used, because it has advantages such as short carrier lifetime and high carrier mobility.

The four main aspects of this study are summarised in the following paragraphs

We described the experimental setup of the terahertz time domain spectroscopy (THz-TDS) system, and showed that THz pulses can be measured experimentally using a photoconductive antenna as emitter and detector.

We showed that the measurement of the THz pulses in time domain was affected by the absorption lines of water vapour. These absorption lines were successfully removed by using Nitrogen gas.

We used the measured THz pulses to determine the refractive indices and absorption coefficients of the samples we investigated. The average refractive index of the Silicon sample was $\bar{n} \simeq 3.49$. In Sapphire sample, the refractive indices were found to be $\bar{n}_o \simeq 3.04$ and $\bar{n}_e \simeq 3.33$. This result shows that Sapphire has two refractive indices, which confirms that it is a birifrengent material in THz region.

Furthermore, the experimental results also enabled the determination of the complex refractive index as function of frequency ($0.5-2.5$ THz) of the various samples such as Teflon, Polyethylene, Polypropylene, Acrylonitrile Butadiene System (ABS), Polyphenylene Oxide (PPO), Polyethylene doped with metal ions, and Polysulfone via the software called Teramat 1.0.

Bibliography

[1] Raluca Marinica Albu, Ecaterina Avram, Valentina Elena Musteata, Mihaela Homocianu, and Silvia Ioan. Opto-electrical properties of some quaternized polysulfones. *High Performance Polymers*, 23(1):85–96, 2011.

[2] Colin Baker, William R Tribe, Thomas Lo, Bryan E Cole, Simon Chandler, and Michael C Kemp. People screening using terahertz technology. In *Defense and Security*, pages 1–10. International Society for Optics and Photonics, 2005.

[3] Peter F Bernath. The spectroscopy of water vapour: experiment, theory and applications. *Physical Chemistry Chemical Physics*, 4(9):1501–1509, 2002.

[4] Paul D Cunningham, Nestor N Valdes, Felipe A Vallejo, L Michael Hayden, Brent Polishak, Xing-Hua Zhou, Jingdong Luo, Alex K-Y Jen, Jarrod C Williams, and Robert J Twieg. Broadband terahertz characterization of the refractive index and absorption of some important polymeric and organic electro-optic materials. *Journal of Applied Physics*, 109(4), 2011.

[5] Susan L Dexheimer. *Terahertz spectroscopy: principles and applications*. CRC press, 2007.

[6] M. Dressel and G. Grüner. *Electrodynamics of Solids: Optical Properties of Electrons in Matter*. Cambridge University Press, 2002.

[7] John F Federici, Brian Schulkin, Feng Huang, Dale Gary, Robert Barat, Filipe Oliveira, and David Zimdars. THz imaging and sensing for security applications explosives weapons and drugs. *Semiconductor Science and Technology*, 20(7):S266, 2005.

[8] Samuel D Gasster, Charles H Townes, David Goorvitch, and Francisco PJ Valero. Foreign-gas collision broadening of the far-infrared spectrum of water vapor. *JOSA B*, 5(3):593–601, 1988.

[9] Ilja Gerhardt. *Scattering and absorption of light by a single molecule under a subwavelength aperture*, volume 68. ETH Zürich, 2006.

[10] David J. Griffiths. *Introduction to Electrodynamics (3rd Edition)*. Addison Wesley, 1999.

[11] Fredric J Harris. On the use of windows for harmonic analysis with the discrete fourier transform. *Proceedings of the IEEE*, 66(1):51–83, 1978.

[12] E. Hecht. *Optics*. Pearson Education, 2012.

[13] Matthias Clemens Hoffmann. *Novel techniques in THz-time-domain-spectroscopy*. PhD thesis, Universitätsbibliothek Freiburg, 2006.

[14] Hiromichi Hoshina, Aya Hayashi, Norio Miyoshi, Fumiaki Miyamaru, and Chiko Otani. Terahertz pulsed imaging of frozen biological tissues. *Applied Physics Letters*, 94(12):123901, 2009.

[15] J.F. James. *A Student's Guide to Fourier Transforms: With Applications in Physics and Engineering*. Cambridge University Press, 2011.

[16] Yun-Sik Jin, Geun-Ju Kim, and Seok-Gy Jeon. Terahertz dielectric properties of polymers. 2006.

[17] AJ Kemp, JR Birch, and MN Afsar. The refractive index of water vapour: a comparison of measurement and theory. *Infrared Physics*, 18(5):827–833, 1978.

[18] T Kuhn, A Bauer, M Godon, S Bühler, and K Künzi. Water vapor continuum: absorption measurements at 350 GHz and model calculations. *Journal of Quantitative Spectroscopy and Radiative Transfer*, 74(5):545–562, 2002.

[19] Lev Davidovich Landau, JS Bell, MJ Kearsley, LP Pitaevskii, EM Lifshitz, and JB Sykes. *Electrodynamics of continuous media*, volume 8. Elsevier, 1984.

[20] Yun-Shik Lee. *Principles of Terahertz Science and Technology (Lecture notes in physics)*. Springer, 2008.

[21] R. A. Lewis. *Terahertz Physics*. Cambridge University Press, 2013.

[22] Hany S Loka, Seldon D Benjamin, and Peter WE Smith. Optical characterization of low-temperature-grown GaAs for ultrafast all-optical switching devices. *Quantum Electronics, IEEE Journal of*, 34(8):1426–1437, 1998.

[23] S. Madhu. *Linear Circuit Analysis*. Prentice Hall College Div, 1988.

[24] MenloSystems. *THz-antennas for 800 nm: The solution for free-space THz systems.* available online at http://www.menlosystems.com/home/products.html.

[25] JL Morán-López, ME Ortiz, LF Rodriguez, and V Romero-Rochin. Measuring the wavelength of a diode laser and the birefringence of mica: the experimental examination of the ipho 40 held in mexico. *European Journal of Physics*, 31(4):S1, 2010.

[26] Seizi Nishizawa, Kiyomi Sakai, Masanoi Hangyo, Takeshi Nagashima, Mitsuo Wada Takeda, Keisuke Tominaga, Asako Oka, Koichiro Tanaka, and Osamu Morikawa. Terahertz time-domain spectroscopy. In *Terahertz Optoelectronics*, pages 203–270. Springer, 2005.

[27] Vivienne H Payne, Eli J Mlawer, Karen E Cady-Pereira, and J Moncet. Water vapor continuum absorption in the microwave. *Geoscience and Remote Sensing, IEEE Transactions on*, 49(6):2194–2208, 2011.

[28] J Engholm Pedersen, S Rud Keiding, CB So, PE Lindelof, WW Rühle, XQ Zhou, et al. 5-THz bandwidth from a GaAs-on-silicon photoconductive receiver. *Journal of applied physics*, 74(11):7022–7024, 1993.

[29] R Piesiewicz, C Jansen, S Wietzke, D Mittleman, M Koch, and T Kürner. Properties of building and plastic materials in the THz range. *International Journal of Infrared and Millimeter Waves*, 28(5):363–371, 2007.

[30] Ioachim Pupeza, Rafal Wilk, and Martin Koch. Highly accurate optical material parameter determination with THz time-domain spectroscopy. *Optics express*, 15(7):4335–4350, 2007.

[31] Jan-Martin Rämer, Frank Ospald, Georg von Freymann, and René Beigang. Generation and detection of terahertz radiation up to 4.5 THz by low-temperature grown GaAs photoconductive antennas excited at 1560 nm. *Applied Physics Letters*, 103(2):021119, 2013.

[32] Jason D Readle. Terahertz time-domain spectroscopy. *University of Illinois at Urbana-Champaign*, 2007.

[33] Caroline Reid. *Spectroscopic methods for medical diagnosis at terahertz wavelengths.* PhD thesis, UCL (University College London), 2009.

[34] Daryoosh Saeedkia. Terahertz photoconductive antennas: Principles and applications. In *Antennas and Propagation (EUCAP), Proceedings of the 5th European Conference on*, pages 3326–3328. IEEE, 2011.

[35] K Sakai. *Terahertz optoelectronics*. Springer Berlin Heidelberg, 2005.

[36] Mark Salomon, Meizhen Xu, Edward M Eyring, and Sergio Petrucci. Molecular structure and dynamics of liclo4-polyethylene oxide-400 (dimethyl ether and diglycol systems) at 25. degree. c. *The Journal of Physical Chemistry*, 98(33), 1994.

[37] Takamasa Seta, Jana Mendrok, and Yasuko Kasai. Laboratory spectroscopic measurement of water vapor for the terahertz-wave propagation model. *URSI Chicago General Assembly*, 14, 2008.

[38] Kailash K. Sharma. *Optics: Principles and Applications*. Academic Press, 2006.

[39] Hagit Shatkay. The fourier transform-a primer. *Brown University*, 1995.

[40] William T. Silfvast. *Laser Fundamentals*. Cambridge University Press, 2004.

[41] Carlo Sirtori. Applied physics: Bridge for the terahertz gap. *Nature*, 417(6885):132–133, 2002.

[42] David M Slocum, Elizabeth J Slingerland, Robert H Giles, and Thomas M Goyette. Atmospheric absorption of terahertz radiation and water vapor continuum effects. *Journal of Quantitative Spectroscopy and Radiative Transfer*, 127:49–63, 2013.

[43] F. Graham Smith, Terry A. King, and Dan Wilkins. *Optics and Photonics: An Introduction*. Wiley, 2007.

[44] Masahiko Tani, Michael Herrmann, and Kiyomi Sakai. Generation and detection of terahertz pulsed radiation with photoconductive antennas and its application to imaging. *Measurement science and technology*, 13(11):1739, 2002.

[45] M Venkatesh, KS Rao, TS Abhilash, SP Tewari, and AK Chaudhary. Optical characterization of GaAs photoconductive antennas for efficient generation and detection of terahertz radiation. *Optical Materials*, 36(3):596–601, 2014.

[46] Zoltán Vörös and Rainer Johnsen. A simple demonstration of frustrated total internal reflection. *American Journal of Physics*, 76(8):746–749, 2008.

[47] Stephan Winnerl, Falk Peter, Sven Nitsche, André Dreyhaupt, Burkhard Zimmermann, Martin Wagner, Harald Schneider, Manfred Helm, and K Kohler. Generation and detection of THz radiation with scalable antennas based on GaAs substrates with different carrier lifetimes. *Selected Topics in Quantum Electronics, IEEE Journal of*, 14(2):449–457, 2008.

[48] Withawat Withayachumnankul, B Ferguson, T Rainsford, Samuel P Mickan, and Derek Abbott. Material parameter extraction for terahertz time-domain spectroscopy using fixed-point iteration. In *Microtechnologies for the New Millennium 2005*, pages 221–231. International Society for Optics and Photonics, 2005.

[49] Withawat Withayachumnankul, Bernd M Fischer, and Derek Abbott. Numerical removal of water vapour effects from terahertz time-domain spectroscopy measurements. *Proceedings of the Royal Society A: Mathematical, Physical and Engineering Science*, 464(2097):2435–2456, 2008.

[50] R.C. Wrede, M.R. Spiegel, and D.C. Arangno. *Schaums Outline of Advanced Calculus, Second Edition*. Schaum's outline series. McGraw Hill, 2002.

[51] Li-juan YANG, Bai-hua ZHANG, and Xu-zhen YE. Fast fourier transform and its applications. *Opto-electronic Engineering*, page S1, 2004.

[52] Yihong Yang, Mahboubeh Mandehgar, and D Grischkowsky. Broadband THz pulse transmission through the atmosphere. *Terahertz Science and Technology, IEEE Transactions on*, 1(1):264–273, 2011.

[53] Yihong Yang, Mahboubeh Mandehgar, and D Grischkowsky. Time domain measurement of the THz refractivity of water vapor. *Optics express*, 20(24):26208–26218, 2012.

[54] Xi-Cheng Zhang and Jingzhou Xu. *Introduction to THz Wave Photonics*. Springer, 2009.

[55] Xuemei Zheng, Colin V McLaughlin, P Cunningham, and L Michael Hayden. Organic broadband terahertz sources and sensors. *Journal of Nanoelectronics and Optoelectronics*, 2(1):58–76, 2007.

[56] B Zhu, Y Chen, K Deng, W Hu, and ZS Yao. Terahertz science and technology and applications. pages 1166–1170, 2009.